OK

ISAS - INTERNATIONAL SCHOOL FOR ADVANCED STUDIES

Statistical Methods in the Study of the Large–Scale Structure in the Universe

Thesis submitted for the degree of

"Magister Philosophiae"

Astrophysics Sector

Candidate:

Stefano Borgani

Supervisor:

Professor
George F. R. Ellis

Academic Year 1989/90

TRIESTE

SISSA - SCUOLA INTERNAZIONALE SUPERIORE DI STUDI AVANZATI
TRIESTE
Strada Costiera 11

No theory is always in agreement with all the facts concerning its field, but not always the fault is of the theory itself.

Paul K. Feyerabend

Acknowledgements

First of all, I would like to acknowledge all the people that collaborated with me in the preparation of the original material presented in this Thesis. They are: Professor Silvio A. Bonometto, who introduced me in the study of the Large Scale Structure in the Universe and suggested some of the computations that I present here; Dr. Massimo Persic, who initiate me to the dynamics of spiral galaxies and for several stimulating discussions; Dr. Paolo Salucci, for the fruitful collaboration, despite the long distance between Trieste and Durham. Many thanks are also due to my supervisor, Professor George F. R. Ellis, for his continuous encouragements and efforts to inprove the readability of this Thesis. I want also to acknowledge Dr. Manolis Plionis and Dr. Riccardo Valdarnini for several discussions and useful suggestions, that also open further development of some results I report here.

Finally, I whish to thank Dr. José Acosta and Dr. Mauro Orlandini for their patience in introducing me in the mysterious worlds of LaTeX and Mongo.

Contents

Introduction

This Thesis is devoted to give a description of the most significant statistical properties of the observed Large Scale Structure in the Universe and the methods to investigate them. In this framework we present our original contribution concerning *biased* models for the formation of cosmic structures and the investigation of the statistical properties (on galaxy scales) of the background matter distribution.

Observations of the Universe on scales comparable to the typical galaxy dimension, $\sim 10\,kpc$, reveal large inhomogeneities and the current view is that down to such scales non–gravitational forces are dynamically dominant. On the other hand, scales $R \gg 10\,kpc$ are considered relevant to the Large Scale Structure. The main difference between small (galaxy) and the large scale lies essentially in the dynamics giving rise to structure formation. In fact, the galaxy mass is determined by its capacity to cool down during the gravitational collapse, as the density increases. A quantitative analysis shows that, for masses $M \gtrsim 10^{12} M_{\odot}$, the heat, produced during the initial collapse, prevents a further compression [171]. Apart from the details of the heat production and dissipation, it is clear that, while the efficiency of the dissipation in a proto–object of dimension R is proportional to R^2 (*i.e.*, to the extension of its surface), the heat production is proportional to R^3 (*i.e.*, to the mass of the object). Then, it is easy to understand that a characteristic scale R^* must exist, such that above R^* the rate of heat production is greater than the dissipation rate, which prevents the gravitational collapse to proceed. The precise value of R^* depends on the geometry of the collapse process, on environmental effects, and on the dissipation characteristics of the collapsing material. Detailed analysis give R^* values that are very similar to the typical scale of normal galaxies.

The study of dissipative processes, that determine the internal structure and dynamics of galaxies, is then essential to understand the origin of galaxies. However, such analysis can be very difficult and the details of the *genesis* and evolution of structures, below the galaxy scales, are widely debated.

On the contrary, on scales much larger than the galaxy ones, it is possible to study the formation and evolution of cosmic structure only on the basis of gravitational interaction. Such evolution follows initially a linear pattern, while later,

when the fluctuation amplitude increases sufficiently, undergoes non–linear phases. For this reason, the large scale dynamics could not be so easy to understand. However, on such scales the problem is much better determined and ones hope is to solve adequately the dynamical picture.

It is also interesting to note that some phenomena on super–galactic scales exist that can not be explained on grounds of gravitational interactions. Indeed, the absorbtion and the emission in different spectral regions (*i.e.*, microwave, infrared, X, etc.) from groups and clusters of galaxies arise from dissipative phenomena that are very similar to those determining the galaxy internal structure. However, the dynamical relevance of such phenomena rapidly decreases as we consider larger and larger scales, and their influence on super–galactic scales is completely negligible.

On such scales the essential observation is that galaxies have a spatial distribution with highly non–random characteristics. They show a strong tendency to group together forming clusters, while cluster themselves cluster to give rise to "superclusters" on even larger scales. This kind of *hierarchical* distribution of objects is one of the most relevant characteristics that must be taken into account by any theory concerning galaxy formation. Indeed, it constraints cosmological models and the amplitude of the primordial fluctuation spectrum on different scales. (In this thesis we will not be concerned with the formation of primordial fluctuations; however only some sketch will be given on the evolution of fluctuations after the epoch of recombination.)

Quantitative measures of the large scale matter distribution can be extracted either from the analysis of the observed distributions of luminous objects like galaxies and clusters, or directly by investigating the effects of the gravitational field, generated by density fluctuations, on the galaxy peculiar motions. In the first case, the statistical analysis of the distribution of luminous objects is mainly realized through the determination of the *correlation functions*. For this reason, the use of functional methods, based on *path–integral* techniques, probably represents the most natural way to connect observational data and theory.

However, any comparison between the observed object distribution and theoretical predictions on the matter distribution should be made with some cautions. In fact, the former is essentially determined by physical phenomena occurring during the structure formation, that probably give rise to some segregation between luminosity and *background* matter distributions. For this reason, the deduction of the *effective* matter distribution from data concerning galaxies and galaxy clusters is quite uncertain. Such a difficulty leads to the introduction of models that should be able to predict the non–linear relation between the observed luminosity density and the matter density, as deduced from the virial analysis of large–scale motions. In

this context, the *biased* models for the formation of cosmic structures represents the natural solution. Indeed, according to such models, we define the observed object distribution as a suitable functional of the *primordial* density fluctuation field. In this way, it is possible to determine, at least in principle, the correlation properties of the background field (and consequently the statistics of the system) starting from that of the luminosity distribution.

Instead of using positions of luminous objects, an investigation of the large scale matter distribution in the Universe can be alternatively realized by observing the effects of the background gravitational field on galaxy peculiar motions. A direct estimate of the radial peculiar velocity of each galaxy can be obtained by subtracting the Hubble velocity, $H_o d$, at the distance d of the galaxy from the observed recessional velocity, once a redshift–independent estimate of d is available. This kind of distance measurement is usually based on intrinsic relations between intrinsic structural parameters of galaxies, such as the famous Tully–Fisher relation for spirals [196] (relating the intrinsic luminosity and the observed rotation velocities) and the Faber–Jackson relation for ellipticals [71] (relating the intrinsic luminosity and the internal velocity dispersion).

It has been recognized for a long time that, under the assumption that a given structure is completely virialized, the internal peculiar motions trace the matter distribution [72]. In this framework, the Peebles' Cosmic Virial Theorem [149,150,151] represented an important step towards the understanding of the existing connection between galaxy peculiar motions and clustering. An exciting development in this field has been the recent completion of large galaxy redshift surveys (*e.g.*, ref. [86]) and the availability of redshift–independent distance estimates (see ref. [39] for a recent review). As a consequence, a lot of theoretical work has been devoted to find methods of extracting the large–scale three-dimensional velocity and mass density fields from measurements of radial peculiar velocities [17,18]. Even though in this Thesis we will not be concerned with the study of large–scale peculiar motions, we will present a method for extracting detailed information on the background matter distribution on galaxy scales from observed rotation velocities in spiral galaxies.

We decided to divide this Thesis into a background part and one in which we present our original work. The first part includes a review of the observational material on the large–scale distribution of galaxies and galaxy systems (Chapter 1) and a technical description of the most important statistical methods which will be used in the rest of the thesis (Chapter 2). The second part contains our original contribution to the theoretical study of *biased* models (Chapter 3), their influence on the statistical properties of object distributions (Chapter 4), and the description of a new method for investigating the small–scale matter distribution by means of spiral galaxy rotation curves (Chapter 5). All the most detailed computations are reported

in the appendices.

In more detail, we present in Chapter 1 a qualitative description of the galaxy distribution and clumpiness, as revealed by recently compiled homogeneous samples. We also present the most important statistical properties of such a distribution. In this framework, we review the main results obtained in the last twenty years from the correlation analysis of galaxy and galaxy cluster samples. Furthermore, we describe previous investigations of the object luminosity distribution by means of the luminosity function (relevant to galaxies) and the multiplicity function (relevant to galaxy systems).

Chapter 2 is devoted to the description of the statistical algorithms that will be widely used in the following chapters. To this aim we furnish a detailed definition and presentation of the correlation functions. Then we give a brief review of some fundamental concepts of functional methods and describe how such methods find a very useful application in the analysis of the correlation properties of a statistical system. A complete determination of the statistics of the large–scale matter distribution in the Universe is possible only once the spectrum of the fluctuations and their probability distribution are known. For this reason we briefly describe the two most popular dark matter spectra, the cold dark matter (CDM) and the hot dark matter (HDM) ones, and show, as an example, how to work out correlation properties in the simple, but most important case of Gaussian fluctuation field. We end the chapter by introducing the concept of a *smoothed* density field, that is of fundamental relevance in the study of the statistics of finite–size object distributions.

In Chapter 3 we introduce the concept of *biased* models for the formation of cosmic structures. After a description of the main motivations for such models, both of theoretical and observational origin, we discuss some physical mechanisms occurring during the galaxy formation processes, that are likely to give rise to substantial differences between object and background matter distributions. In this framework, we assume that the distribution of a given class of objects is defined through the so–called *biased field*, which represents a suitable non–linear functional of the background fluctuation field. In the original formulation of the *biased* model of galaxy formation the observable structures are identified as those peaks of the density field that exceed a fixed threshold value. In this picture, the threshold function for selecting fluctuations coincide with a Heavyside θ-function (θ-threshold case). In general, the specific shape of the threshold function does depend on the physical phenomena leading to the object formation, so that a step function seems to be inadequate to describe the effective object distribution. In this chapter a general formalism is developed to deduce the statistical properties of the *biased field* in terms of that of the matter field, in the generic cases of non–θ threshold and non–Gaussian background fluctuations. Moreover, we show that in the so–called high–threshold approximation

all the peculiarity of the n-point correlation functions, that are related to a non–θ threshold, gradually vanish. Viceversa, the effect of the shape of the threshold function is still present in the expressions of the object number density.

Chapter 4 is entirely devoted to the study of the influence of non–θ thresholds on the statistics of galaxy clusters. In particular, we take tentatively into account some effects, like non–sphericity in the gravitational collapse process and merging between different scale fluctuations, by means of two suitable choices for the threshold function. As a first application, we consider the data on the multiplicity function for groups and clusters of galaxies. Such data have been already interpreted in the literature by means of the so–called Press & Schechter [167] approach, but only at a qualitative level. After reproducing these results, we discuss the possibility of interpreting observational data in the framework of our general biased models in a CDM background field. Taking a non–θ threshold, that accounts for non–sphericity in the gravitational collapse, enable us to get a good fit to all the data on the multiplicity function with the introduction of only one phenomenological parameter. After that, we analyse the effects both of non–spherical geometry and merging on the evolution of fluctuations by assuming two suitable shapes for the threshold function. We also compare the results of our models with observational data, taking both a CDM and a scale–free background spectra. In our analysis, the CDM spectrum has difficulties in reproducing the data, even for different choices of the threshold. A better agreement is obtained for a scale–free spectrum. In any case, the predictions of our models are sensitive to the shape of the threshold and corrections to the θ–bias case lead to systematic improvements of the fit. Indeed, we attain a satisfactory fit by assuming a scale–free spectrum and by allowing for merging effects.

In Chapter 5 we describe a new method to investigate the distribution of dark matter surrounding spiral galaxies. Such a method is essentially based on the fact that observed rotation velocities can be used as tracers of the background gravitational field, as well as for the large–scale peculiar velocities. We apply the Persic & Salucci [158] mass decomposition method of splitting spiral galaxy rotation curves into the contributions of dark (halo) and luminous (disk) matter. We find that the background 2-point correlation function is well modeled by a power law and extends its galaxy counterpart with the same slope down to scales of few kiloparsecs. This supports the conjecture that galaxies and background matter have closely related clustering properties. A similar analysis for the disk matter reveals different correlation properties and suggests that any such difference, between the clustering patterns of luminous and dark components, are to be ascribed to their different dissipation properties. The extension of the investigation of the 2-point function to higher–order correlations shows that functions up to the sixth order can be detected and fit the so–called hierarchical expression. Moreover, from a comparison between the cluster-

ing amplitudes of the background and galaxy functions two different cosmological scenarios emerge: an open Universe where light is a good tracer of mass, or a flat Universe where an excess in light is ~ 3 times larger than the corresponding excess in mass. We discriminate between these possibilities by formulating the Cosmic Virial Theorem, which involves the amplitude of the three-point function, on galaxy scales. Once such amplitude is independently deduced for the same sample of galaxies, a low–density, no–bias Universe is virtually ruled out.

Chapter 1

The observational data

1.1 A "by eye" description of galaxy clustering

Starting from the first investigation of the galaxy distribution in the sky, it has been recognized that galaxies in our neighborhood are distributed in a very inhomogeneous way. Indeed, they are found to form double systems, groups with up to 100 members, rich clusters with more than 1000 members and diameters of $\sim 5 - 10\, Mpc$, up to superclusters involving scales of $\sim 30 - 100\, Mpc$.

Figure 1.1a, b, that represents the distribution of galaxies on portions of the sky surveyed by Zwicky *et al.* [208], shows that galaxies are clearly clustered and reveals some well known structures. For example, the Coma cluster is the dense concentration at $\alpha = 13^h$ and $\delta = 28°$, while the Virgo cluster is centered at $\alpha = 12.5^h$ and $\delta = 12°.5$. A decrease in the galaxy density west of 9^h and east of 16^h is due to galaxy obscuration. In the southern hemisphere the most relevant structure is the Pisces–Perseus chain which runs across the sky in the declination interval 30°–40°. Again, the apparent absence of galaxies at 21^h and 3^h is due to galactic absorption.

More recently, the availability of a large amounts of galaxy redshifts made it possible to have a three–dimensional picture for some regions of the Universe. In this way, Kirshner *et al.* [115] discovered the Boötes void (see Figure 1.2), a region where the density of bright galaxies is $\lesssim 20\%$ of the mean, and that has a diameter of $\sim 6000\, km\, s^{-1}$ (let us observe that, due to the well known Hubble relation between recession velocities and distances of galaxies, linear dimensions can be equally expressed in units of $km\, s^{-1}$ or $h^{-1} Mpc$; here h is the Hubble constant in units of $100\, km\, s^{-1} Mpc^{-1}$ and, because of observational uncertainties, $0.5 \lesssim h \lesssim 1$).

More extended surveys revealed an even greater variety of structure in the 3-dimensional pictures of the Universe. In Figure 1.3, surfaces of constant densities from the first CfA catalog are shown [78]. The contours correspond to 4 times the

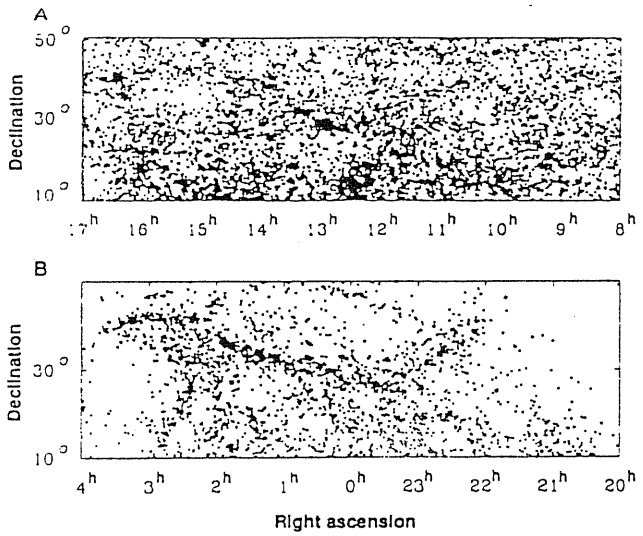

Figure 1.1: *Position of galaxies in the Zwicky catalogue, with $m \leq 15.5$ in the northern galactic cap (panel a) and in the southern galactic cap (panel b). The coordinates are cartesian.*

mean density. This picture indicates that 90% of all galaxies are in clusters or strings, while the volume occupied by these structures is 10% of the total sampled volume. Then, 90% of the Universe seems to be empty, in the sense that these regions do not contain appreciable quantities of luminous matter.

A specific attention was devoted by Giovannelli & Haynes [103] in a survey of the Perseus–Pisces filament. In their redshift survey over the declination interval 30° to 40°, they showed that many of the galaxies in the region lie in a narrow redshift range around $\sim 5000\, km\, s^{-1}$ (Figure 1.4*a*). Then, as well as in the angular projection, the Pisces–Perseus filaments turns out to be a thin structure in the redshift direction too.

Instead of investigating the details of the galaxy distribution in a specific region, the extension of the CfA survey [59,108] is an attempt to map the general galaxy distribution, rather than to explore a particular feature on the sky. The results of such an investigation are shown in Figures 1.4*b*, *c*, *d*. One of the most relevant feature is the presence of several large regions that appear to be almost devoid of galaxies, while galaxies seem to be distributed in elongated structures. De Lapparent *et al.* [59] suggested that "the apparent filament is a cut through boundaries of several bubble–like structures". The pronounced radial "finger" along the line of sight in *b* and *c* is the Coma cluster. If we could map the actual position of galaxies rather than their redshifts , this feature would be approximately spherically symmetric, with a radius $\sim 1\, h^{-1} Mpc$. The elongation in redshift space occurs because of peculiar velocities of galaxies inside the cluster, that affect the determination of the distance, if simply based on the Hubble relation. Although gravitationally bound systems produce local peculiar motions on scales of few megaparsecs, the removal of

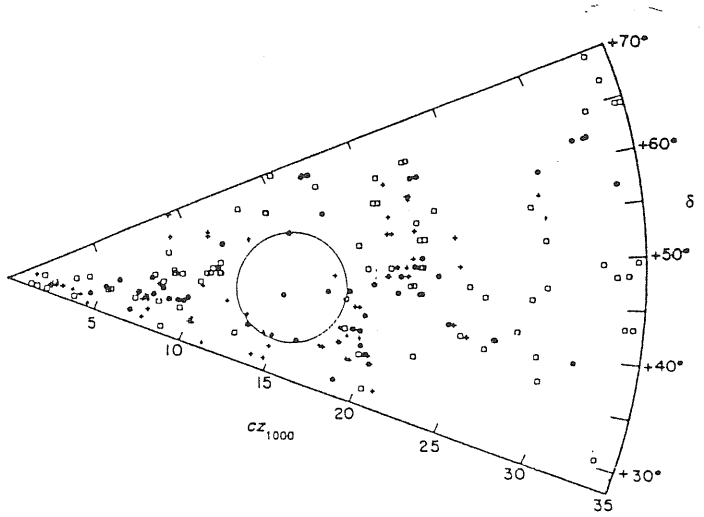

Figure 1.2: *Cone diagram for the Boötes survey. The circle shows the location of the void; the galaxies within the circle are outside the right ascension range of the void (after [115]).*

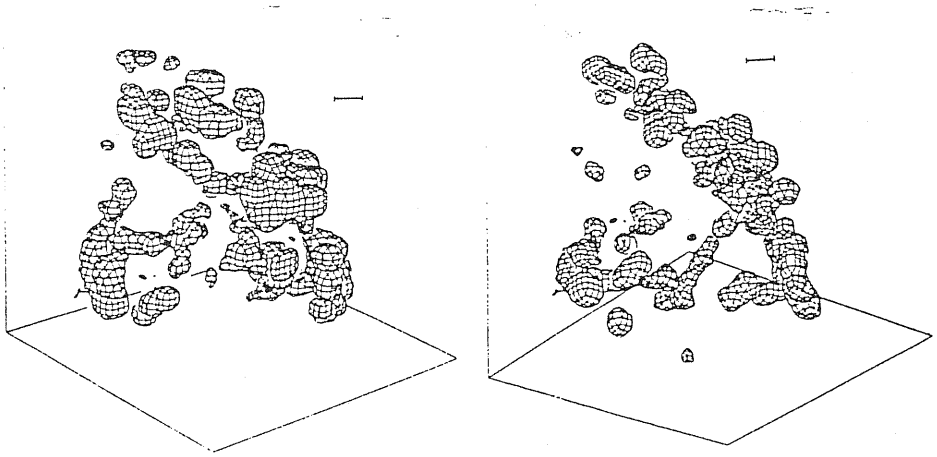

Figure 1.3: *Surfaces of constant density from the CfA catalogue. The northern hemisphere map contains 1130 galaxies (after [78]).*

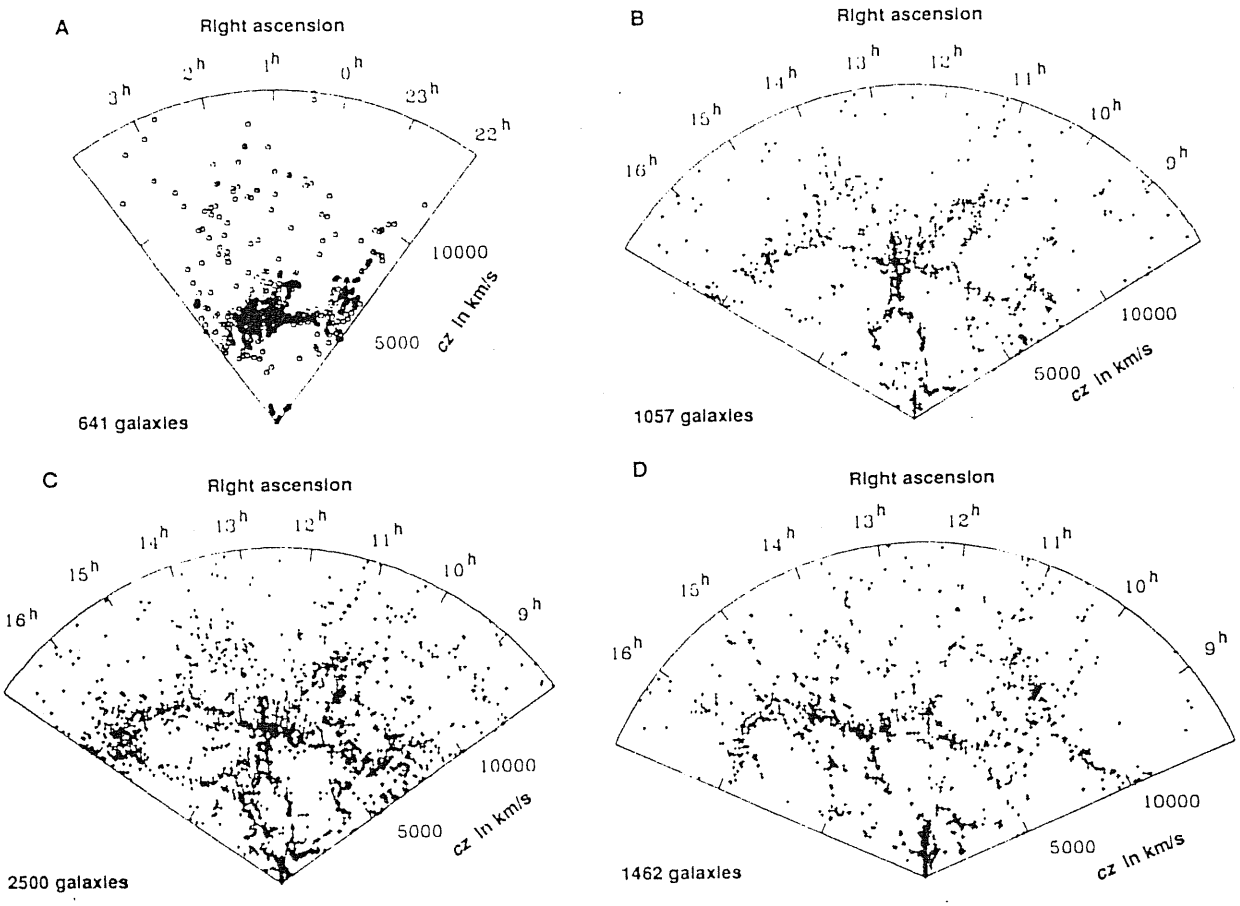

Figure 1.4: *(A) Cone diagram for galaxies in the region of the Perseus–Pisces chain. (B) Cone diagram for a complete sample of galaxies with* $m \leq 15.5$ *in the declination range* $26°.5 \leq \delta \leq 32°.5$. *(C) Cone diagram for a complete sample covering the declination range* $26°.5 \leq \delta \leq 44°.5$. *Note the "Great Wall" that runs across the survey. (D) Cone diagram for a nearly complete sample covering the declination range* $8°.5 \leq \delta \leq 14°.5$ *(after [86]).*

such effects is not expected to change the global picture very much on scales of tens of megaparsecs. The slice of Figure 1.4*b* demonstrates than filamentary structures in this region are cuts through two–dimensional sheets, not one dimensional filaments. Indeed in contrast to Figure 1.4*a*, that samples the apparent filaments of Figure 1.1*a*, there are no detected filaments on the sky in the region covered by Figure 1.4*b*. Thus, it being difficult to expect that the intersection of a slice with a 3–dimensional network of filaments give rise in turn to a network of filaments, a sheet–like distribution of galaxies around the voids can account for the data.

Despite the great amount of observations devoted to enlarging the sampled volume by means of three-dimensional surveys, there is up to now no evidence for an upper limit to the scale of structure discernible in the redshift analysis. One such very large scale feature is the so–called *Great Wall* revealed by the slices of the

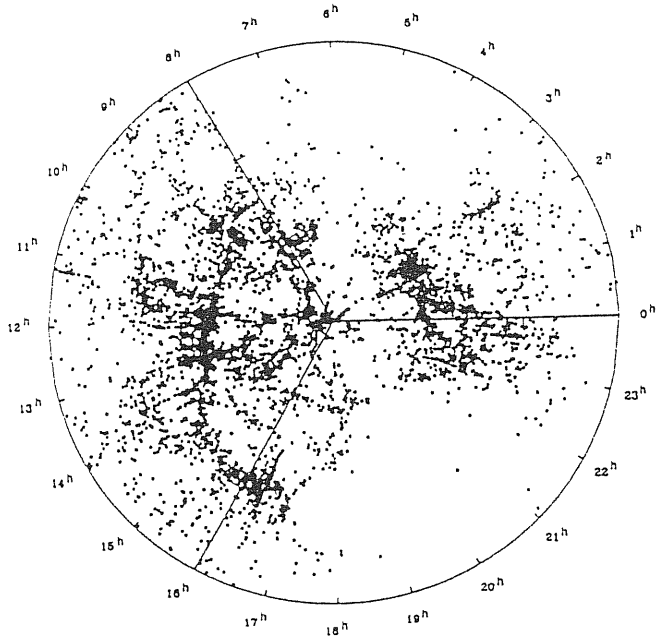

Figure 1.5: *A 360° view that shows a relation between the "Great Wall" and the Perseus–Pisces chain. The slice covers the declination region* $20° \leq \delta < 40°$ *and contains all the 6112 galaxies with detected redshift* $cz \leq 15,000\, km\, s^{-1}$. *The regions that appear to be almost devoid of galaxies are obscured by the galactic plane (after [86]).*

extended CfA sample [86]. The apparent extension of the *Great Wall* in both right ascension and declination is only limited by the extension of the survey. The detected spatial extent in these two dimensions is $\sim 60\, h^{-1} Mpc \times 170\, h^{-1} Mpc$. The typical thickness, approximately along the redshift direction, is $\lesssim 5\, h^{-1} Mpc$. The density contrast between the wall and the mean of the survey is $\Delta\rho/\rho \simeq 5$. The 360° view of Figure 1.5 indicates the geometrical relation between the Pisces–Perseus chain and the Great Wall.

A further remarkable result, that seems to confirm the sheet–like structure of galaxy distribution, has been obtained by Broadhurst *et al.* [38]. They combined data coming from four distinct surveys at the north and south Galactic poles to produce a well sampled distribution of galaxies by redshift on a linear scale extending to $2{,}000\, h^{-1} Mpc$. By analysing their pencil–beam survey, they found a remarkably regular one–dimensional distribution with most galaxies lying in discrete peaks separated by $\sim 128\, h^{-1} Mpc$ (Figure 1.6). The finding of one–dimensional structure of such periodicity might be understood in terms of a cellular distribution of galaxies. The cross section of a pencil–beam with such three–dimensional structure could generate structure with form strongly dependent on the direction of the beam itself.

As a concluding remark, let us observe that all the above qualitative descriptions of the observed pattern in the galaxy distribution give a quite good idea of the

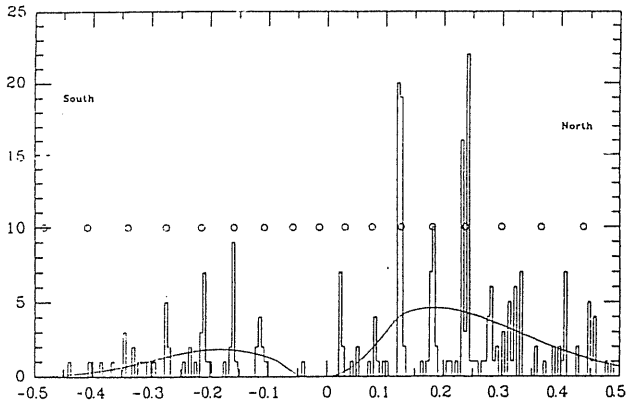

Figure 1.6: *Redshift distribution for the four surveys at the galactic poles. Circles indicate a best–fit constant comoving separation of* $128\,h^{-1}Mpc$ *(after [38]).*

way in which galaxies are arranged to form large–scale structures. However, such features can hardly constraint by themselves any theoretical model on the origin and evolution of cosmic large–scale structure. Rather, in order to test theoretical predictions against observational features, a detailed statistical description of the galaxy distribution is required. In the following sections of this chapter, we will describe and review the main results that has been obtained from quantitative analysis of galaxy samples.

1.2 Data on the clustering of galaxies

This section is devoted to the description of the galaxy clustering pattern as deducible from the statistical analysis of homogeneous samples. In particular, after a brief description of the most important galaxy samples, we summarize the main results obtained in the last twenty years on the correlation properties of the galaxy distribution.

1.2.1 The data samples

The statistical investigation of the distribution of galaxies has been initially realized by means of bidimensional *homogeneous samples*, in which angular positions of the objects on the sky are reported. An angular sample contains all the objects of a given class (*e.g.*, galaxies or clusters of galaxies), whose apparent luminosity exceeds a fixed value. For historical reasons, apparent luminosities are expressed in logarithmic units, by means of the *apparent magnitude*

$$m \;=\; \mathrm{M} + 5\,log\,r + 25\,. \qquad (1.1)$$

Here r represents the distance of the object from the observer, while M is the *absolute* magnitude (*i.e.*, the apparent magnitude of the same object, if placed at the fixed distance $r = 10\,pc$).

Another important quantity that characterizes a galaxy sample is the *depth* of the survey. In fact, galaxies selected by apparent magnitude are found to have fairly definite absolute magnitudes, M^*, with a standard deviation about this value of about one magnitude. Thus, according to eq. (1.1), M^* and m define a characteristic distance

$$D \;=\; 10^{0.2(m-\mathrm{M}^*)-5}\,Mpc\,, \tag{1.2}$$

that defines the depth of the sample.

Among the most important (apparent) magnitude-complete angular samples of galaxies, there are:

i) **the Zwicky sample** [208], that contains the angular positions of 3753 galaxies, having apparent magnitudes $m \leq 15.5$ and coordinates with *declination* $\delta \geq 0$ and *galactic latitude* $b \geq +40°$ (see Figure 1.1);

ii) **the Lick sample** [183], that includes galaxies with apparent magnitudes $m \leq 18$, each belonging to an elementary cell of $10' \times 10'$. In turn, these cells are grouped in sets of 36×36 to form maps, that have an extension of $6° \times 6°$. The centers of each maps are separated one from each other by 5° in declination, from $\delta = -20°$ up to $\delta = +90°$. In addition, the separation in right ascension is such that each map is overlapped to adjacent one at most for 1°;

iii) **the Uppsala Catalog** [140], that contains all the galaxies with magnitude $m \leq 14.5$, in the region of sky characterized by $\delta \geq 0°$ and $b \geq +40°$;

iv) **the Jagellonian field** [176], that includes more than 10,000 galaxies comprised in a small angular region of $6° \times 6°$. This sample turns out to be almost 8 times deeper than the Zwicky sample in such a way that, even though the angular extension of the latter is $\sim$ 10 times larger, the *spatial* dimension of the two sampled regions are almost the same;

v) **the ESO/Uppsala Catalogue** [120], which is considered complete for those galaxies of the southern hemisphere having declination $\delta < -17°.5$ and major diameters greater than 1′;

vi) **the APM Galaxy Survey** [129] that has been realized by using an automatic plate scanner. With such a procedure, there have been detected about 2 millions of galaxies, covering the area of the sky $\delta < -20°$ and $b \lesssim 40°$. This galaxy sample is 95% complete in the magnitude range $17 < m < 20.5$ and corrections for plate overlapping and galactic obscuration have been included.

Other than the above angular samples, there exist also some *spatial samples*, that, in addition to the angular coordinates, give for each object the redshift too. As for the two–dimensional samples, also the three–dimensional ones are limited in apparent magnitude. However, because the distance of each object follows with good accuracy from its redshift, the three-dimensional samples allow to to work out homogeneous subsamples, that are limited by a fixed absolute magnitude.

The spatial samples usually considered are the following:

i) **the CfA1 (Center for Astrophysics) survey** [106], that includes all the 2400 galaxies having magnitudes $m \leq 14.5$ and angular positions characterized by ($\delta > 0^{\circ}$, $b > +40^{\circ}$) and by ($\delta \geq -2^{\circ}.5$, $b < -30^{\circ}$);

ii) **the Southern Sky Redshift Survey (SSRS)** [139], that includes 1657 galaxies, selected from the ESO Catalogue [120], in an area of $1.75\,sr$ with declination south of $-17^{\circ}.5$ and galactic latitude below -30°. The sample diameter is limited with all galaxies having $log\, D(0) > 0.1$, where $D(0)$ is a "face-on" diameter, in arcminutes, that is related to the galaxy morphological type and to the angular dimension;

iii) **the CfA2 survey** that is now slowly emerging. It extends the original CfA redshift survey to include galaxies brighter than $m = 15.5$. When completed, this survey will include all galaxies between 8^h and 17^h in the north galactic cap, and between 20^h and 4^h in the south cap. A first slice, that contains 1057 objects in the declination range $26^{\circ}.5 \leq \delta \leq 32^{\circ}.5$ (Figure 1.4*b*), was completed in 1986 [59], while the data has been recently published [108]. Other two slices have been completed [86] and contain 1443 galaxies with $32^{\circ}.5 \leq \delta \leq 44^{\circ}.5$ (Figure 1.4*c*), but the data are still unpublished. A fourth strip, that includes 1462 galaxies with $8^{\circ}.5 \leq \delta \leq 14^{\circ}.5$, is nearly completed (Figure 1.4*d*).

1.2.2 The two-point correlation function

The investigation of the galaxy clustering by means of angular samples is mainly based on the determination of the angular 2-point *correlation function* $w(\vartheta_{12})$. Its definition is related to the joint probability

$$\delta^{(2)}P \;=\; n^2\,\delta\Omega_1\,\delta\Omega_2\,[1 + w(\vartheta_{12})] \tag{1.3}$$

of finding two objects in the solid angles $\delta\Omega_1$ and $\delta\Omega_2$, respectively, at angular separation ϑ_{12}. The value of the correlation function mirrors the non-randomicity of the distribution (see §2.1, below). In particular, the object positions are said to be *correlated* if $w(\vartheta_{12}) > 0$, *anticorrelated* if $w(\vartheta_{12}) < 0$. In general, for greater and

greater values of $|w(\vartheta_{12})|$, the distribution of galaxies turns out to be less and less random.

A huge amount of work has been done in order to detect the correlation properties of the galaxy distribution, starting from the pioneering paper of Totsuji & Kihara [193], and, most importantly, through the analysis of Peebles and coworkers.

Making use of the Zwicky and Lick samples, Peebles & Hauser [157] yielded an estimation of the angular 2-point correlation function.

Peebles [148] analysed all the $6° \times 6°$ area of the Jagellonian field, comparing the results also with those obtained from the Zwicky sample. In this analysis, the expectation values of the number of galaxies contained inside cells of size $3'.75 \times 3'.75$ were considered. In this way, he obtained 98×98 cells with an average of one galaxy per cell. No corrections for vignettature and galactic absorbtion effects have been introduced, the region described by the sample being small and at high galactic latitude.

Afterwards, Groth & Peebles [97] used the Lick catalogue for a further determination of $w(\vartheta)$. They considered 476 maps having the galactic latitude of the central points $|b_c| \geq 40°$ and introduced suitable corrections to the sample. In order to eliminate overlapping between adjacent maps, they took only the regions of angular dimension $5° \times 5°$ around the center of each map; correction factors were also introduced to make the sample formed by all the maps truly homogeneous, as well as to take into account galactic and atmospheric absorption.

All these analyses converge to indicate that the angular 2-point function is well represented by the power law

$$w_g(\vartheta) \;=\; A_g\, \vartheta^{1-\gamma} \tag{1.4}$$

with $\gamma = 1.77 \pm 0.04$ and amplitude A_g dependent on the depth of the sample, with a break from the power–law behaviour in the case of large angular separations (see Figure 1.7).

From the analysis of the APM sample, which is particularly suitable for investigating correlations at large separations, Maddox *et al.* [129] found an angular 2–point correlation function having the same slope as eq. (1.4), in the range of validity of the power–law. The break they found from the power law occurs roughly at the same physical separation as found by Groth & Peebles [97], but with a decline much more gently from a power law on larger scales. Consequently, they argued that Groth & Peebles may have removed some intrinsic clustering in correcting for large–scale gradients in the Lick sample.

In order to extract information on the *spatial* properties of the galaxy distribution from eq. (1.4), we need a method for deprojecting angular data, so to obtain

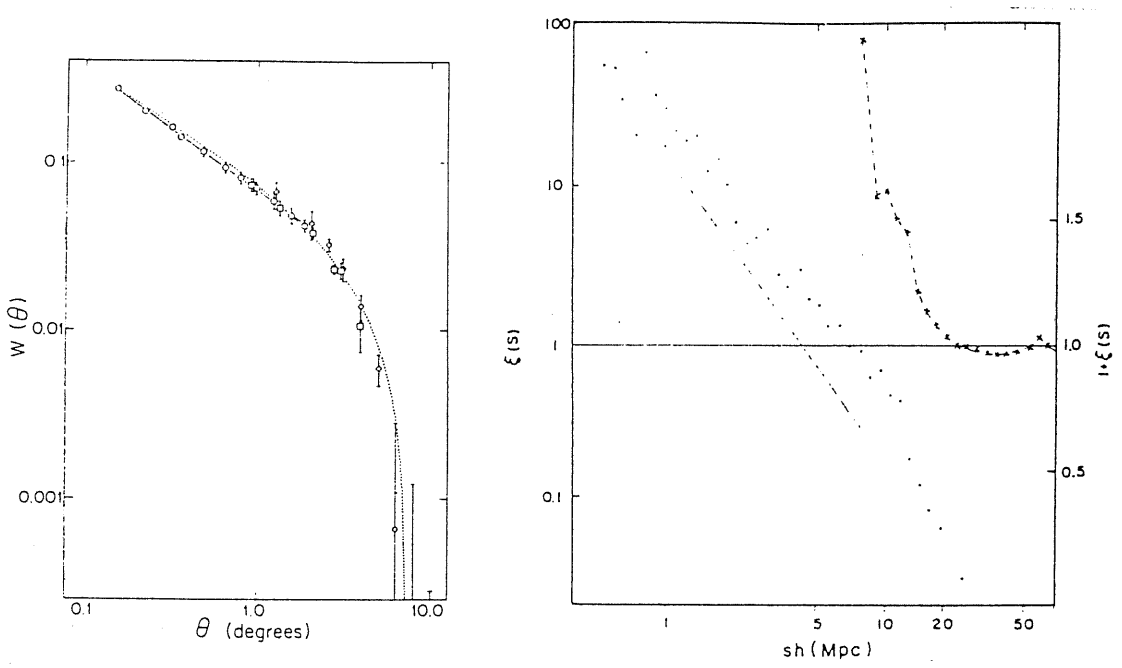

Figure 1.7: *Left panel: estimate of the galaxy 2-point* angular *correlation function from the Lick sample; the solid line represents the best–fit power–law (1.4), with* $\gamma = 1.734$ *and* $A_g = 0.0684$ *(after [97]). Right panel: estimate of the galaxy 2-point* spatial *correlation function from the CfA1 redshift survey; crosses on the right represent the quantity* $\xi(r) + 1$*, while the dashed line is a power–law with exponent* $\gamma = 1.8$ *(after [52]).*

the *spatial* 2-point correlation function. Such a function is defined, in analogy with eq. (1.3), by means of the joint probability

$$\delta^{(2)}P \;=\; n^2\,\delta V_1\,\delta V_2\,[1+\xi(r_{12})] \tag{1.5}$$

of finding an object in the small volume δV_1 and another one in δV_2, at separation r_{12}. In this case too, the spatial 2-point function $\xi(r_{12})$ is a measure of the non-randomicity of the spatial galaxy distribution.

A suitable deprojection method, that allows us to derive the expression of $\xi(r)$ from that of the angular function, is provided by the *Limber equation* [122]. Such an equation, that holds under the hypothesis of absence of any correlation between position and luminosity of objects, permits us to express the angular function $w(\vartheta)$ in terms of the spatial function $\xi(r)$. The inversion of the Limber equation, in which we are interested, is also possible in several cases [73]. Indeed, in the case of the power-law model (1.4) for $w(\vartheta)$, the spatial 2-point function turns out to be

$$\xi_g(r) \;=\; \left(\frac{r_{o,g}}{r}\right)^{\gamma}, \tag{1.6}$$

with the same value of γ and with the value of the *clustering length* $r_{o,g}$ depending on the amplitude of $w(\vartheta)$. All the investigations of the spatial correlations by means

of angular data indicate $r_{o,g} \simeq 5\,h^{-1}Mpc$, with some scatter around this value, in the range of separations $0.1\,Mpc < rh < 10\,Mpc$ [157,148,97], but with a break in the power law for larger separations. Some evidences have also been found [94,119] that support the validity of the power-law model (1.6) down to $r \sim 3\,h^{-1}kpc$.

Such results on the spatial 2-point correlation function follow naturally from the analysis of three-dimensional samples. By using the CfA1 sample, Davis & Huchra [51] deduced the galaxy spatial number density, while Davis & Peebles [52] obtained the expression (1.6), for the 2-point function, with $r_{o,g} = 5.4 \pm 0.3\,h^{-1}Mpc$, in fairly good agreement with angular results and for the same range of separations (see Figure 1.7).

An analysis of the CfA sample for the region centered on the Virgo cluster leads Einasto *et al.* [67] to find a shoulder in the 2-point function at $r = 4 - 5\,h^{-1}Mpc$. Such a discrepancy with respect to the Davis & Peebles' result indicates that, in some cases, the system under study may have specific properties – such as transition from clusters to strings in rich clusters – which disappear when a larger sample is considered. In a further analysis of the CfA Catalogue and dividing the full sample into subsamples of different volumes, Einasto *et al.* [68] found that the value of the galaxy clustering length turns out to vary with the volume of the subsample itself. In particular, the conventional value $r_{o,g} = 5\,h^{-1}Mpc$ is obtained for a sampling volume containing not more than one supercluster, while the estimated correlation length for a fair sample of the Universe is $r_{o,g} = 10\,h^{-1}Mpc$. The authors argued that such an effect could be related to differences in relative volumes occupied by large voids; samples chosen from larger volumes have usually larger relative volumes of voids.

A statistical investigation of the CfA2 sample led to quite large uncertainties in the determination of galaxy number density and 2-point correlation function. De Lapparent *et al.* [60] found an indetermination of $\sim$ 25% in the galaxy number density. In this analysis the galaxy 2-point function was found to have a slope $\gamma \simeq 1.6$ and a correlation length $r_{o,g} \simeq 7.5\,h^{-1}Mpc$, in the $\sim 3 - 14\,h^{-1}Mpc$ range. Because of the large uncertainty in the mean density, the ranges in the slope and amplitude are respectively $\sim 1.3 - 1.9$ and $\sim 5 - 12\,h^{-1}Mpc$. On scales larger than $20\,h^{-1}Mpc$, the correlation function is indeterminate.

Several attempts had been also devoted to the investigation of the clustering properties of galaxies having different morphology. The importance of such an investigation lies in the fact that different clustering for different morphological type galaxies can be due to a difference in the physical processes that gave rise to their formation, other than to environment effects. Indeed, it has been recognized from long time that small groups tend to contain more elliptical galaxies than do looser groups [75]. On the contrary, the central regions of rich compact clusters appear to

be dominated by elliptical and lenticular galaxies and contain few normal spirals; irregular, less dense clusters, which have a composition similar to that of the field, contain many spirals [141].

By analysing the Uppsala Catalog, Davis & Geller [50] determined the angular 2-point correlation function for the distribution of galaxies of various morphological types. They found that elliptical galaxy clustering is characterized by a power law with a slope ($\gamma_{\rm E} \simeq 2.1$) steeper than that for spiral clustering ($\gamma_{\rm S} \simeq 1.69$), while the lenticular slope has an intermediate value ($\gamma_{\rm L} \simeq 1.71$). Dressler [65] studied the galaxy populations in 55 rich clusters. He found that a well–defined relationship exists between local galaxy density and galaxy type, which confirms an increasing elliptical and S0 population and a corresponding decrease in spirals with increasing density inside the cluster. Still by using the Uppsala Catalog, Giovannelli *et al.* [89] revealed evidence for continuous morphological segregation in a wide range of galaxian densities in the Pisces–Perseus supercluster. Furthermore, evidences of significant differences in the slope of the angular 2-point function for different morphological types are found, in agreement with previous results. From the analysis of the three-dimensional CfA survey, Börner & Mo [36] obtained a correlation length for elliptical and lenticulars that they estimated to be ~ 1.7 times that of spiral and irregulars.

1.2.3 Higher order correlations

The determination of the 2-point correlation function does not give in general a complete description of a given statistical system. Indeed, further informations can be obtained when one goes to higher–order correlations. At the third order, the joint probability

$$\delta^{(3)}P \;=\; n^3\,\delta\Omega_1\,\delta\Omega_2\,\delta\Omega_3\,[1 + w(\vartheta_{12}) + w(\vartheta_{13}) + w(\vartheta_{23}) + z(\vartheta_{12},\vartheta_{13},\vartheta_{23})]\,. \qquad (1.7)$$

represents a generalization of eq. (1.3) and defines the angular 3-point correlation function $z(\vartheta_{12},\vartheta_{13},\vartheta_{23})$. In the case of the large–scale galaxy distribution, the analysis of the 3-point function in the Zwicky, Lick and Jagellonian samples has been discussed by in a series of papers by Peebles and coworkers [156,97,148]. They concluded that data on the 3-point function can be well fitted by assuming the so-called *hierarchical model*

$$z(\vartheta_{12},\vartheta_{13},\vartheta_{23}) \;=\; Q\,[w(\vartheta_{12})w(\vartheta_{23}) + w(\vartheta_{12})w(\vartheta_{13}) + w(\vartheta_{13})w(\vartheta_{23})] \qquad (1.8)$$

with $Q = 1.29 \pm 0.21$.

However, Bonometto *et al.* [26] repeated the analysis of the Zwicky sample, interpreting the presence of a limiting magnitude as the effect of an *optical bias.*

Consequently, it has been shown that a better fit to the angular data on the 3-point function can be obtained by assuming

$$z(\vartheta_{12},\vartheta_{13},\vartheta_{23}) = Q_1\,[w(\vartheta_{12})w(\vartheta_{23}) + w(\vartheta_{12})w(\vartheta_{13}) + w(\vartheta_{13})w(\vartheta_{23})] + \\ +Q_2\,w(\vartheta_{12})w(\vartheta_{23})w(\vartheta_{13}) \qquad (1.9)$$

with $Q_1 \simeq Q_2 \simeq 1$. Such results have a problematic interpretation, because it seems to imply that the expression for $z(\vartheta_{12},\vartheta_{13},\vartheta_{23})$ depends on the definition itself of magnitude–limited sample.

In a similar fashion, it is also possible to consider correlation functions for n (> 3) points. An estimation of such high-order function is however quite difficult, because of the increasing noise in the sample with the increase of the correlation order. Fry & Peebles [82] made an estimation of the 4-point correlation in the Lick Catalog. Sharp *et al.* [184] analysed the higher-order correlation properties of the Zwicky sample, by means of the so–called *moment method* [1]. They found a signal for the 4-point function, while an attempt to estimate the 5-point function gave results that were completely lost in the noise. More recently, an analysis of the Lick sample by means of the moment method revealed signals of correlation up to the eighth order [191].

1.2.4 Fractal analysis of the galaxy distribution

Some criticism in the use of the correlation function $\xi(r)$ for the analysis galaxy samples has been made by Pietronero [162]. He claimed that a definition for a dimensionless ξ includes normalization with respect the mean density n (see eq. (1.6)). Thus, if the real distribution is such that the average density depends on the size of the sampled volume, the same set of object appears to have different correlation lengths, depending on the volume considered. In fact, if we postulate a (self–similar) *fractal* structure where the number density of objects within r is

$$N(r) = B\,r^{\mathrm{D}} \qquad (1.10)$$

(B is a constant and D, also a constant, is the *fractal dimension* of the system), the average density inside a sphere of radius R_{S},

$$n = \frac{N(R_{\mathrm{S}})}{V(R_{\mathrm{S}})} = \left(\frac{3}{4\pi}\right) B\,R_{\mathrm{S}}^{3-\mathrm{D}}\,, \qquad (1.11)$$

turns out to be a function of the sample size R_{S}. Accordingly, the 2-point function is given by

$$\xi(r) = \frac{D}{3}\left(\frac{r}{R_S}\right)^{-(3-D)} - 1\,. \qquad (1.12)$$

[1] See §5.4 and Appendix C for a detailed description of such a method.

Then, while the exponent of the power law, $\gamma = 3 - D$, is an intrinsic property of the distribution, the normalization of ξ depends explicitly on R_s. Alternatively to $\xi(r)$ we can consider the quantity

$$\Gamma(r) = n\,[\xi(r) + 1] \tag{1.13}$$

that is independent of R_s. Making use of such a quantity, Pietronero analysed the CfA Catalog, dividing the whole sample into two volume-limited subsamples. He found that galaxy distribution can be described by a simple fractal which extends up to the sample size, without any evidence for a homogeneous distribution.

However, alternative interpretations of the observed scaling of ξ with the size of the sample volume have been also proposed. Indeed, clustering properties of galaxies may not be independent of luminosity. Such segregation of luminosity is a natural consequence of galaxy formation processes and is in agreement with the detected differences in the clustering of different morphological types [28,35].

In order to investigate the fractal structure of the galaxy distribution, Martinez & Jones [131] divided the CfA sample in 10 volume-limited subsamples. They found that, despite the scale invariance on length scales less than $\sim 5\,h^{-1}Mpc$, the Universe is not a single fractal, but a more complicate structure, a *multifractal*. On larger scales the Universe breaks away from this scale-free behaviour and tends to homogeneity and isotropy.

1.3 Data on the clustering of galaxy clusters

In analogy with the previous section, we describe now the clustering properties of galaxy systems like groups and clusters. Again, after a description of the most important samples, we review the results of correlation analysis applied to the distribution of galaxy systems. Some attention will be also devoted to the existing relations between clustering properties of different structures, namely galaxies, groups and clusters.

1.3.1 The data samples

Galaxies does not represent the only claass of cosmic structures that can be used to investigate the large scale statistics of the Universe. Indeed, galaxies themselves tend to group together to form structures on larger scales, such as groups or clusters. In turn, such structures can be considered as single objects and, then, the statistics of their distribution can be analysed in full analogy with the case of galaxies. In order to use galaxy clusters and groups as tracers of the large–scale structure in

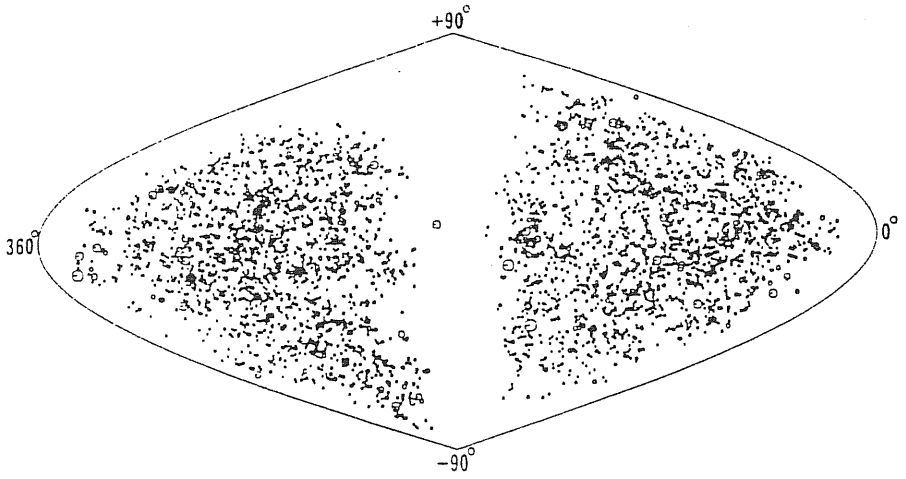

Figure 1.8: *All–sky distribution in supergalactic coordinates of the 4073 Abell clusters contained in the Abell and ACO samples. The symbol size has been scaled by distance class: the $D = 0$ clusters are represented by large open circles, while $D = 7$ clusters corresponds to small dots (after [3]).*

the Universe, complete samples that describe their distribution over a wide volume are required. In general, different samples use quite different selection criteria for identifying clusters to be included in the catalog, so that different it can be also the respective distributions. The most important *angular* samples of clusters are described as follows.

i) **The Abell Catalog** [1] includes a total of 2712 clusters that are the richest, densest clusters found on the Palomar Survey plates (see Figure 1.8). Of these rich clusters, 1682 constitute Abell's complete statistical sample and are distributed over 4.26 steradians. The Abell selection criteria can be summarized as follows: (a) a cluster must contain at least 50 members in the magnitude range m_3 to $m_3 + 2$, where m_3 is the magnitude of the third brightest galaxy; (b) all these members should be contained within a circle of radius $1.5\,h^{-1}Mpc$ around the center of the cluster; (c) the cluster redshift z should be in the range $0.02 \lesssim z \lesssim 0.20$; and ($d$) the cluster should lie north of declination $-27°$. The 1682 clusters in the sample are divided in 6 distance classes (D); 104 clusters belong to the first 4 distance classes (nearest clusters), while the remaining belong to the subsample $D = 5 + 6$. For each cluster, it is also given a richness class, $R = 1$ through 5, that is related to the number of members belonging to each cluster.

ii) **The Zwicky Catalog** [208] contains 9700 clusters of galaxies visible to the limit of the Palomar plates ($m \simeq 20$). The criteria for including clusters in the

sample are less restrictive than Abell's; (a) The cluster must contain at least 50 galaxies in the magnitude range m_1 to m_1+3, where m_1 is the magnitude of the brightest galaxy; (b) these galaxies must lie within the isopleth, where the projected density of galaxies is about twice that of the neighboring field; (c) no limits on the redshift are specified, but structures such as the Virgo cluster (which cover very large areas) are not included; and (d) the clusters must lie north of declination $-3°$ and within well specified areas. Cluster richness is defined as the number of galaxies, corrected for the mean field count, that are located within the isopleth of twice the field density. In general, Zwicky clusters differ in size from Abell's, the former being mostly larger, lower density systems. These differences arise mainly from the different criteria used in the identification process.

iii) **The Schectman Catalog** [181] identifies 646 clusters of galaxies, based on the Lick counts in 10' bins and using an automated procedure. The clusters are located at galactic latitudes $|b| \geq 40°$ and declinations $\delta > -22°.5$. The selection was based on local density maxima of the galaxy distribution above a given threshold value. A selected threshold of five galaxies per count bin was used; this threshold is considerably higher than the tail of the background distribution of galaxy counts, which has a median of 1.3 galaxies per bin. Such a threshold of five galaxies succeeds in detecting 70% of Abell's $D \leq 4$ clusters and 10% of the $D = 5$ clusters. Moreover, the Schectman procedure selects clusters that are considerably poorer than the Abell $R \geq 1$ clusters.

iv) **The ACO Catalog** [3] represents an extension to the southern hemisphere of the Abell sample. It contains 1635 clusters of richness class $R \geq 0$ and includes clusters in the $-27° < \delta < -17°$ overlap region with the Abell clusters. Together with the Abell Catalogue, it constitute an all–sky sample of 4073 rich Abell clusters (see Figure 1.8), nominally complete to a redshift $z = 2$ for clusters with populations of 30 or more galaxies in the magnitude range m_3 to $m_3 + 2.0$.

As in the case of the galaxy samples, the detection of redshifts for clusters included in angular catalogs permits the compilation of 3–dimensional surveis. We describe in the following the most relevant spatial samples of clusters and groups.

i) **The Hoessel, Gunn & Thuan (HGT) sample** [105] includes the redshifts of all Abell clusters with distance class $D \leq 4$ and richness class $R \geq 1$, that are located at galactic latitude $|b| \geq 30°$. A total of 104 clusters belong to this sample.

ii) **The Bahcall & Soneira (BS) sample of superclusters** [10], that is complete to a redshift of $z \leq 0.08$ and defines superclusters as density enhancement of the cluster distribution deduced from the HGT sample. The selection process was repeated for different overdensity values f, from $f = 10$ to $f = 400$. In particular, a total of 16 superclusters are cataloged for $f = 20$, 12 superclusters for $f = 40$ and 11 superclusters for $f = 100$.

iii) **The Struble & Rood (SR) Catalog** [186], that contains all the 588 Abell clusters (including richness class $R = 0$) with measured redshifts.

iv) **Geller & Huchra (GH) deep redshift survey** [85], that consists of the 145 Abell clusters with $R \geq 0$, $D \leq 6$ and with redshift $z \lesssim 0.2$, in the area $10^h < \alpha < 15^h$, $58° < \delta < 78°$.

v) **The Ramella, Geller & Huchra (RGH) sample** [169] that identifies groups of galaxies in the first two complete strips of the CfA redshift survey [108].The group catalog is produced by applying an algorithm with searches for "friends of friends" in redshift space [107]. Galaxies in a groups are separated by limiting values of the line–of–sight velocity and of the projected separation. The catalog contains 128 groups with at least three members and 56 with at least five members.

vi) **The Southern Hemisphere Group (SEG) sample** [48], contains 87 groups with 3 or more members and with a surrounding density contrast greater than 20, identified from the SSRS galaxy catalog. The groups are located southwards of declination $-17°.5$, below galactic latitude $-30°$ and have mean radial velocities less than $800\, km\, s^{-1}$.

1.3.2 Correlation functions for galaxy systems

Many attempts has been devoted in the last years in order to trace the large–scale structure of the Universe on the basis of the observed statistical properties for the cluster distribution [7]. Indications that the cluster distribution on the sky is not random was already found several years ago by Abell [1,2]. Further evidences of super–clustering in the Abell survey was also detected by Bogart & Wagoner [21], Hauser & Peebles [102], and Rood [173] by means of nearest–neighbor distributions and/or angular correlation functions.

Bahcall & Soneira [23] and, independently, Klypin & Kopylov [118] determined the rich ($R \geq 1$) Abell cluster 2-point correlation function from the HGT 3-dimensional sample. They found strong correlations in both the $D \leq 4$ redshift

sample and in the larger and deeper $D = 5 + 6$ sample. Moreover, the spatial correlation function was found to fit a power–law relation of the form

$$\xi_c(r) = \left(\frac{r_{o,c}}{r}\right)^{\gamma}, \tag{1.14}$$

with $r_{o,c} \simeq 25\,h^{-1}Mpc$ and $\gamma \simeq 1.8$, for the distance range $5 \lesssim r \lesssim 150\,h^{-1}Mpc$. Thus, the rich–cluster autocorrelation function exhibits the same slope as the galaxy function, but with a greater value of the correlation length. (Such difference between the clustering lengths of these two kind of cosmic structure is a very crucial point that will be discussed in detail in Chapter 3.) They also noted that ξ_c is elongated in the line–of–sight direction and thus deduced large peculiar velocities ($\sim 2000\,km\,s^{-1}$) between clusters. A similar conclusion was also reached by Postman *et al.* [165] and by Batuski *et al.* [13] in the analysis of the Zwicky sample and of the ACO southern catalog, respectively.

However, Sutherland [189] showed that random peculiar motions cannot explain the line of sight correlations at separations $\gtrsim 50\,h^{-1}Mpc$. On the contrary, he claimed that such anisotropies in the redshift space correlation function are to be ascribed to spurious line–of–sight clustering. Such kind of clustering suggests that the richness of an Abell cluster could be apparently enhanced by background galaxies, so to produce significant line–of–sight correlations in a richness–limited sample. By analysing the SR spatial sample of Abell clusters and after correcting for the anisotropies in the redshift space correlations, Sutherland found that the power–law (1.14) for the rich–cluster 2-point function is still satisfied, but with a reduced correlation length, $r_{o,c} \simeq 14\,h^{-1}Mpc$. A numerical simulation of such contamination [56] allowed the construction of a "decontaminated" sample of $D \leq 4$, $R \geq 1$ clusters, with the result that the correlation are reduced of a factor ~ 2 (in agreement with the conclusions of Sutherland). A similar conclusion was also reached by Sutherland & Efstathiou [188]. In their analysis of the deep GH survey, they found further evidences of line–of–sight contamination and a resulting value of the clustering length $r_{o,c} \simeq 13\,h^{-1}Mpc$. In addition, effects of projection contamination on the *angular* cluster correlation function has also been found by Olivier *et al.* [143] in the analysis of the Abell and ACO catalogs. After removing these effects by means of a suitable model for the galaxy distribution around clusters, the correlation strength for small angular separation is reduced by a factor 2-3, in agreement with the results obtained from the spatial samples.

Differently from rich clusters, the analysis of samples of galaxy groups reveal that such structures are less clustered than galaxies. Indeed, from the investigation of the SEG sample, Maia & da Costa [130] showed that groups are characterized by a 2-point function of the type (1.14), with the same slope $\gamma \simeq 1.8$ in the range of separations 2-10$h^{-1}Mpc$, but with amplitude 2.5 times smaller than that of galaxies.

In a similar analysis of the correlation function for groups defined in the RGH sample, Ramella *et al.* [170] found $\gamma \simeq -1$ and $r_{o,c} \simeq 6\,h^{-1}Mpc$, over the range 3-10$h^{-1}Mpc$, but with very large uncertainties.

A further extension in the study of the large–scale structure of galaxy distribution is possible by investigating the spatial correlations between superclusters of galaxies (*i.e.*, groups of rich clusters). Bahcall & Burgett [8] analysed the BS sample of superclusters. They found a correlation on scales $\sim 100\,h^{-1}Mpc$, that is significant at about 95%-99% confidence level. The correlation appears to be stronger than that of galaxy and galaxy clusters (see Figure 1.9).

All these determinations of the 2-point correlation function for galaxy systems seem to suggest a dependence of the clustering strength on the richness, that is quite similar to the discrepancies found in the investigation of the clustering for galaxies with different morphology. In particular an increase in the clustering is observed for richer systems. A detailed description of the dependence of the correlation amplitude on the richness of galaxy groups and clusters will be given in the following.

As in the case of the galaxy distribution analysis, some attempts have also been devoted to the investigation of higher order correlations for galaxy clusters.

Toth *et al.* [192] analysed the northern Abell, the southern ACO and the Shechtman angular samples or rich clusters. They found that the angular 3-point correlation function is still consistent with the hierarchical expression (1.8), as in the galaxy case, with $Q = 1.0 \pm 0.1$ for Abell clusters and a systematically lower value $Q = 0.64 \pm 0.04$ for the Shechtman groups.

An investigation of the spatial 3-point function has been recently performed by Jing and Valdarnini [111], that considered a sample of 227 Abell clusters with known distances. They found that a hierarchical expression with $Q \simeq 0.7$ give a reasonable fit to the data, without, however, ruling completely out the Kirkwood model (1.9).

1.3.3 Galaxy–cluster cross correlations

Similarly to what we have seen up to now for the correlation properties of galaxies and galaxy clusters separately, it is also possible to investigate the cross–correlations between the positions of one galaxy and one cluster. Such an investigation is very useful in order to study the galaxy distribution inside cluster halos. In order to introduce the angular *cross–correlation* function $w_{cg}(\vartheta)$, let us consider the joint probability

$$\delta^{(2)}P \;=\; n_c n_g \delta\Omega_1 \delta\Omega_2 [1 + w_{cg}(\vartheta_{12})] \tag{1.15}$$

of having a cluster in the solid angle element $\delta\Omega_1$ and a galaxy in $\delta\Omega_2$.

The joint statistical investigation of the distribution of galaxies and clusters was performed by Seldner & Peebles [182]. In this analysis, the distribution of galaxy is that of the Lick Catalog, while the Abell Catalog is used for the cluster positions, characterized by $|b| > 40°$ and $\delta > -22°.5$. In this way about one fourth of the sky was covered, by including 1339 clusters. An appreciable precision for the fit to the data was found by using for the cross–correlation function the expression

$$w_{cg}(\vartheta) = A\vartheta^{-\rho} + B\vartheta^{-\sigma} , \tag{1.16}$$

with $\rho \simeq 1.4$ and $\sigma \simeq 0.2$. In the above relation, the first term, that is dominant for small separations, is essentially due to the galaxy density around each cluster, while the second term, that dominates for larger angular separations, takes into account the contribution of the clustering between clusters.

A further investigation of the cross–correlation properties for the distributions of galaxy and clusters was realized by Lilje & Efstathiou [121], that used the same catalogs as before both for galaxies and for clusters. They used redshifts for Abell clusters to compute a cross–correlation function $w_{cg}(\sigma)$, where $\sigma \equiv v\vartheta/H_o$ is the projected separation between a cluster with recession speed v and a galaxy at angular distance ϑ from the cluster center. They evaluated the amplitude of the spatial cross–correlation function $\xi_{cg}(r)$ by means of more recent determinations of the galaxy luminosity function. Their results show that on scales $r < 20\,h^{-1}Mpc$ the shape of the spatial cross–correlation function is well described by

$$\xi_{cg}(r) \simeq \left(\frac{8.8\,h^{-1}Mpc}{r}\right)^{2.2} . \tag{1.17}$$

Differences with respect to the Seldner & Peebles' results are probably due to the different assumption for the galaxy luminosity function.

The concept of cross–correlations can also be generalized for investigating the relative statistical properties of any two different distributions of cosmological interest. Indeed, in Chapter 5 we will discuss in detail a new method to study cross–correlations between the distribution of galaxies and the distribution of the background matter. In particular, such a kind of analysis will be very useful in order to test whether galaxies are good tracers of the matter distribution and, if not, what is the relation that links such two distributions.

1.3.4 Relationship between the clustering of different cosmic structures

In their analysis of the spatial correlation function for Abell clusters, Bahcall & Soneira [23] discussed the decrease of the correlation amplitude with cluster richness.

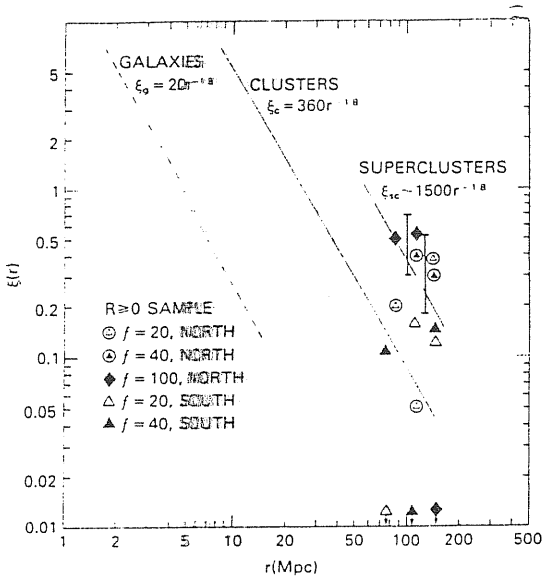

Figure 1.9: *Spatial correlation of superclusters. Different symbols indicate samples of different overdensity. The dashed line indicates the supercluster correlation function if it follows the power–law* $r^{-1.8}$. *The solid line represents the* $R \geq 1$ *cluster correlation function of Bahcall & Soneira, while the short–dashed line is the galaxy correlation function of Peebles and coworkers (after [8]).*

They classified individual galaxies as $N = 1$ systems (where N is the Abell's criterion for richness classification) and suggested that galaxies have a correlation function amplitude that falls on the richness relation for clusters. From a physical perspective, it would however be misleading to treat individual galaxies in the same way as galaxy systems, the processes governing galaxy formation probably being different from those relevant for groups and clusters.

Indeed, Szalay & Schramm [190] pointed out that galaxy clustering may be intrinsically different from cluster clustering. They discuss a possible *universal* correlation function characterized by a slope $\gamma = 1.8$ and by a dimensionless amplitude

$$\beta(L) = \xi(L) = \left(\frac{r_o}{L}\right)^{\gamma}. \tag{1.18}$$

Here $L = n^{-1/3}$ (n is the mean spatial density of objects) represents the average value of the separation. They derive $\beta \simeq 0.35$ for Shechtman clusters and for Abell $R \geq 1$ and $R \geq 2$ clusters, while $\beta \simeq 1.1$ for galaxies. Such a result suggests that galaxies are relatively more strongly correlated than clusters (see Figure 1.10*b*).

Bahcall & Burgett [8] extended such analysis to include also the correlation function of superclusters. They argued that the increasing of the clustering amplitude with the richness of the system is valid for supercluster clustering too (see Figure 1.9). Moreover, by using the adimensional correlation amplitude (1.18), they found that superclusters have $\beta \simeq 0.3$, in agreement with the value for clusters (see Figure

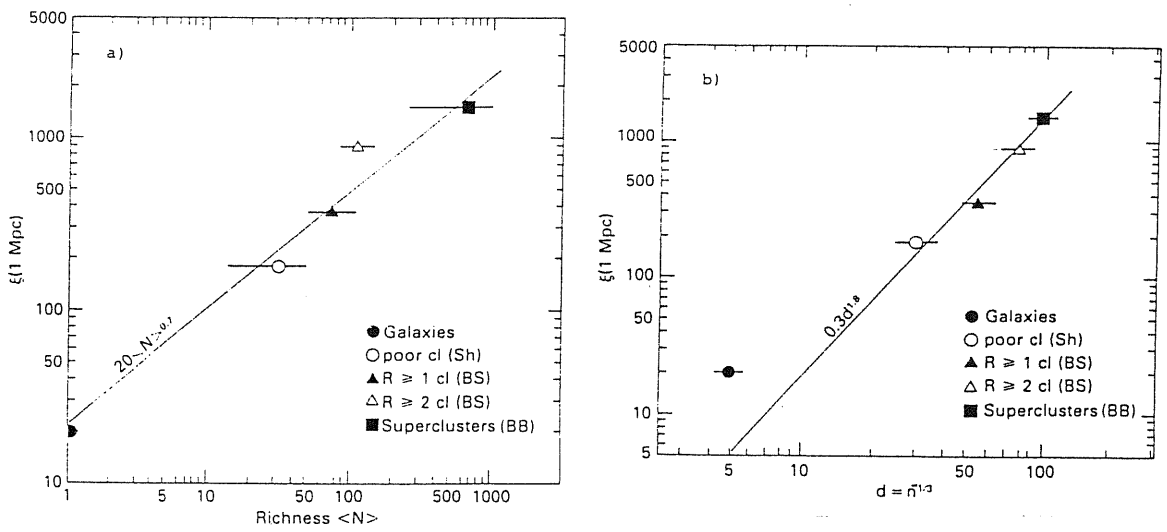

Figure 1.10: (*a*) *The dependence of the correlation function on the richness of the system. A range of the mean richness is shown for each cluster point. The solid line indicate an approximate dependence on richness.* (*b*) *The dependence of the correlation function on the mean separation of object. The solid line represents a* $d^{1.8}$ *dependence (after [8]).*

1.10*a*).

Such properties of scaling of the correlation function with richness and mean spatial density highlight a deep connection between physical processes relevant for the formation of different cosmic structure, from groups to superclusters. In our view, these regularities in the correlation amplitude for the distributions of distinct class of objects represent a significant observational constraint; any theory for the formation of the large-scale structure in the Universe should be able to predict such peculiar features relating clustering properties of vastly different galaxy systems.

1.4 The luminosity distribution of cosmic structures

From the analysis of homogeneous samples of galaxies and galaxy systems it is possible to obtaine not only as their angular or spatial distributions, but also their luminosity distribution. This section is devoted to the description of observational data concerning the luminosity distributions for galaxies and galaxy systems. We will also discuss how the luminosity distribution can be related to the so–called *mass function*, that describes the aboundance of cosmic structure in a given mass range.

1.4.1 The galaxy luminosity function

An essential statistical tool for the investigation of the luminosity distributions of cosmic structures is the *luminosity function.* This is defined as the comoving number density of galaxies with luminosity between L and $L+\delta L$ (see, *e.g.*, §49 of ref. [151]). Accordingly, we introduce the luminosity function by means of the probability

$$\delta P \;=\; \Phi(L)\,\delta L\,\delta V \tag{1.19}$$

of finding an object with luminosity between L and $L+\delta L$ in the volume element δV. Following the definition of luminosity function $\Phi(L)$, the number density of galaxies can be expressed as

$$n_g \;=\; \int_0^\infty \Phi(L)\,dL\,. \tag{1.20}$$

In order to extract the galaxy luminosity function from observational data, it is useful to introduce the *luminosity distribution* $n_S(L)$. This is defined so that $n_S(L)\,\Delta L$ gives the number of galaxies contained in the sample S, in the luminosity interval of width ΔL centered on L [180]. Let $V_S(L)$ the volume sampled at luminosity L by the sample S. Then, the luminosity function $\Phi_S(L)$ of a galaxy sample can be expressed as

$$\Phi_S(L)\,\Delta(L) \;=\; \frac{n_S(L)\,\Delta L}{V_S(L)}\,. \tag{1.21}$$

Assuming large–scale homogeneity for the Universe, in the limit of large, randomly chosen sample volumes, all luminosity functions approach a universal limit defined by

$$\Phi(L) \;=\; \lim_{V_S(L)\to\infty} \Phi_S(L)\,. \tag{1.22}$$

We shall henceforth refer to this limit as the luminosity function for galaxies. In practice, one can only determine the luminosity function for finite samples. Sample luminosity functions will show deviations from the universal luminosity function that decrease as sample volumes increase. The size of these deviations depends on the nature of the processes that give rise to the distribution of galaxies in space and luminosity. For a randomly chosen sample volume, the luminosity function yields an expected luminosity distribution

$$n_e(L) \;=\; \Phi(L)\,V_S(L)\,. \tag{1.23}$$

Luminosity functions (and distributions) may be obtained for each subclass of galaxies which can be identified with criteria other than luminosity.

A first attempt to find an analytical expression of the galaxy luminosity function was due to Schechter [180]. He used the galaxy sample by de Vaucoleurs & de Vaucoleurs [62]. This sample includes galaxies with magnitude $m \leq 11.75$ and

$b \geq 30°$, without including all the galaxies having angular distance $\leq 6°$ from the center of the *Virgo cluster* (in fact, the high velocity dispersion in this region is such that redshifts are not good distance indicators). In such analysis, he determined both the general luminosity function and the luminosity function only for galaxies contained inside clusters and found that the latter differs from the former only by a multiplicative factor. A good fit to the data was obtained with a luminosity function of the type

$$n_e(L)\,dL \;=\; \Phi^*\,V^*\Big(\frac{L}{L^*}\Big)^{\alpha}\,e^{-L/L^*}\,d\Big(\frac{L}{L^*}\Big)\,, \tag{1.24}$$

with $\alpha = -5/4$ and L^* corresponding to an absolute magnitude $\mathrm{M}^* = -21.4$ (taking for the Hubble parameter $h = 1/2$), and with $\Phi^*\,V^* = 216 \pm 6$ for the general luminosity function, while $\Phi^*\,V^* = 910 \pm 120$ for the cluster galaxies.

After Schechter's investigation of the galaxy luminosity function, many attempts have been devoted to obtaine an analytic expression for the general luminosity function. All such investigations converge to indicate the validity of a Schechter–like expression (1.24), with some differences in the deduced values of the parameters (see ref. [74] for a review).

Recently, de Lapparent *et al.* [61] calculated the luminosity function for two complete slices of the extension of the CfA redshift survey. They found that the shape of the luminosity function can still be approximated by a Schechter function with $\mathrm{M}^* = -19.2 \pm 0.1$ and $\alpha = -1.1 \pm 0.2$. Because of the large–scale inhomogeneities in the sample (comparable with the size of the sampled volume) they used an inhomogeneity–independent technique. Nevertheless, such large–scale inhomogeneities introduce large fluctuations in the derived amplitude of the luminosity function; $\Phi^* = 0.020 \pm 0.005\,h^3 Mpc^{-3}$. A comparison with the luminosity function deduced from the first CfA survey [106] shows consistency at the $\sim 2\sigma$ level (see Figure 1.11).

The luminosity function of galaxies inside clusters has been analysed by Lugger [128], who considered nine Abell clusters. He found that in three clusters there appears to be a deficit of bright galaxies in the inner regions with respect to the outer regions. In the composite luminosity function of all nine clusters there is evidence for an excess of bright galaxies in the high–density regions relative to the low–density regions. Moreover, the faint end of the luminosity function is flatter in the high–density regions than in the low–density regions.

1.4.2 The multiplicity function of galaxy systems

The concept of luminosity function of galaxies can be generalized to include galaxy systems. For this aim, Gott & Turner introduced the *group multiplicity function*

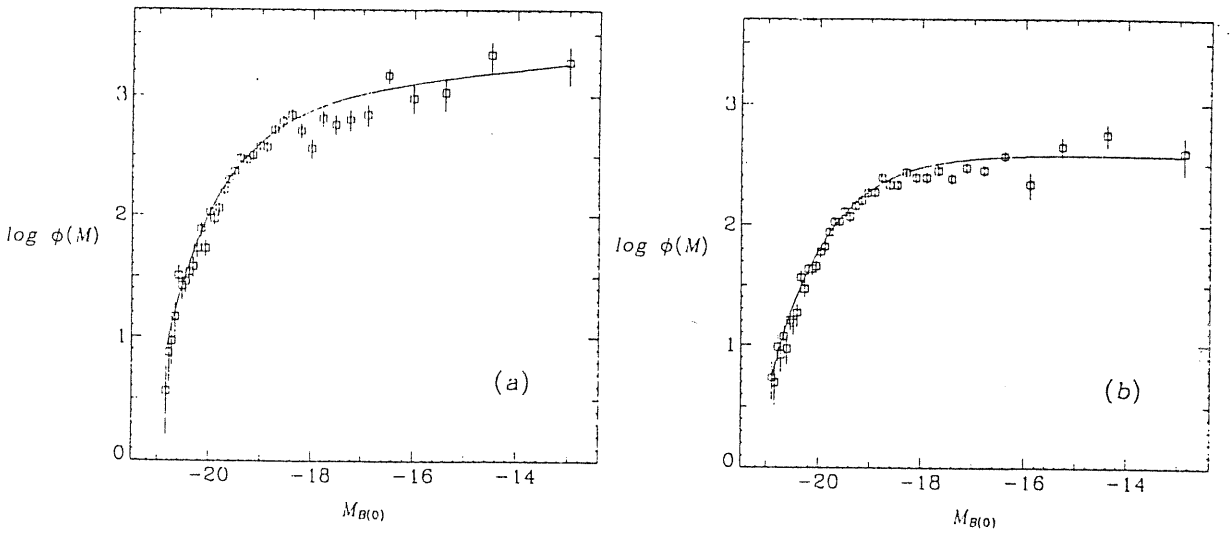

Figure 1.11: *Luminosity function* $\Phi(M)$ *for (a) the extended CfA sample, and (b) the* 14.5 *sample. Vertical lines are the* $\pm 1\sigma$ *error bars, and the smoothed curves are the fitted Schechter functions. The values of* M^* *and* α *for the fitted functions are (a)* -19.18 *and* -1.12*; (b)* -19.30 *and* -0.98*. Amplitudes are arbitrary (after [61]).*

[93]. In order to define such a function, let us consider a region of the Universe, that can be considered a fair sample, and determine the mean luminosity density. An estimation by Gott & Turner [92] gives $\rho_L = 3.76 \times 10^8 L_\odot h^2 Mpc^{-3}$, while some different values have been found by other authors (for example, Kirshner *et al.* [116] found $\rho_L = 2.4 \times 10^8 L_\odot h^2 Mpc^{-3}$). For a fixed density enhancement factor X, let us consider the largest possible sphere such that the mean luminosity density inside such sphere satisfies

$$\rho_{L,sphere} > X \rho_L . \tag{1.25}$$

The objects inside that sphere constitute the first group of galaxies, with total luminosity L_1. Next, let us consider the second largest sphere satisfying eq. (1.25) and not overlapping with the first sphere. Continue the process until every galaxy is assigned to a group. Some groups may consist of only one galaxy. We define the multiplicity function $\Phi_g(L)$ as the luminosity function of groups in such a group catalogue.

A first determination of the multiplicity function from a data sample has been performed by Gott & Turner [93]. They built their group catalog [194] by considering all the galaxies of the Zwicky catalog with apparent magnitude $m \leq 14$ and angular position characterized by $|b| > 40°$ and $\delta > 0$. The resulting angular density of such this distribution is $\bar{\sigma} = 180\, gal\, deg^{-2}$. The group catalog is then determined by selecting the structures with an angular galaxy density

$$\sigma_g = 7.95\, \bar{\sigma} . \tag{1.26}$$

The factor of 7.95 seems to be high enough to identify real physical association in

most cases. In this way, Gott & Turner were able to detect 283 groups, including 199 single galaxies.

A further investigation of the multiplicity function has been carried out by Bahcall [6], that found a universal multiplicity function holding at the same time for rich Abell clusters and Turner & Gott groups [194]. However, in doing such analysis there are several difficulties due to the ambiguity in the definition of single galaxy and to the uncertainties in the determination of the galaxy number density for very small ($< 10^{10} L_{\odot}$) groups. The Turner & Gott sample contains 350 single or 'field' galaxies. It is however possible that such galaxies belong to groups that are under the detection threshold. In any case, even though many single galaxies are luminous members of a group, these must represent the most part of the luminosity of the group itself. Consequently, such galaxies are not expected to cause appreciable modifications of the multiplicity function for groups and Abell clusters. In this analysis, Bahcall firstly determined the expression for $\Phi(L)$ that represents the best fit to the data on rich Abell clusters,

$$\Phi(L) = 5.2 \times 10^{-7} \left(\frac{L}{L_o}\right)^{-2} e^{-L/L_o} \, Mpc^{-3} \, (10^{12} L_{\odot})^{-1} , \tag{1.27}$$

with $L_o = 0.8 \times 10^{13} L_{\odot}$. Then this fit has been extended to include the groups of the Turner & Gott sample, finding

$$\Phi(L) = 1.6 \times 10^{-7} \left(\frac{L}{L_o}\right)^{-2} e^{-L/L_o} \, Mpc^{-3} \, (10^{12} L_{\odot})^{-1} , \tag{1.28}$$

with $L_o = 1.6 \times 10^{13} L_{\odot}$. A further generalization to include groups formed by only one galaxy leads to

$$\Phi(L) = \frac{1.6 \times 10^{-7}}{(1 + 1.6 \times 10^{10}/L)^{-0.75}} \left(\frac{L}{L_o}\right)^{-2} e^{-L/L_o} \, Mpc^{-3} \, (10^{12} L_{\odot})^{-1} , \tag{1.29}$$

with the same value for L_o as in eq. (1.28). The additional term in the denominator of eq. (1.29) has been introduced to take into account the lowering of the multiplicity function in correspondence of $L < 10^{10} L_{\odot}$ and makes such expression quite different from the usual Schechter function.

As a final comment, let us observe that the shape of the multiplicity function, as deducible from data samples, is very sensitive to the different techniques and definitions that are used for identifying galaxy systems on different scales. This show the necessity of realizing homogeneous samples in which groups of galaxies are defined in an objective and scale–independent way.

1.4.3 The mass function for cosmic structures

In analogy with the luminosity and multiplicity functions that describe the distribution in luminosity for galaxies and galaxy systems, we can also describe their distribution in mass by means of the *mass function* $n(M)$. In analogy with $\Phi(L)$, this function is determined by the number of objects that have mass between M and $M + dM$.

The very importance of such a function lies in the fact that any theoretical model for the formation of cosmic structures gives predictions directly on the mass spectrum of the objects. In turn, the luminosity distribution can be deduced once the mass–to–light ratio, M/L, for each object is known. If we assume a flat Universe with $\Omega_o = 1$, [2] the value $\rho_{\rm M} = 3 \times 10^{11} M_\odot h^2 Mpc^{-3}$ for the mean mass density gives a mass–to–light ratio of the order

$$\frac{M}{L} = 1500\,. \tag{1.30}$$

Evaluations of the M/L ratio are usually performed by measuring the discrepancy between luminous mass and dynamical mass, that is deduced from the virial analysis of galaxy motions [90,52,14]. The results of such an analysis suggest that $M/L \simeq 100$-$200\,h^{-1}$ on galaxy scales, while $M/L \simeq 200$-$500\,h^{-1}$ on the scales of rich clusters [20]. Agreement with the value in eq. (1.30) can however be achieved by taking into account a large amount of mass that can be present in galaxy voids and is not detected by dynamical analysis.

The first and, maybe, most popular approach to a theoretical determination of the mass function for cosmic structure was provided by Press & Schechter [167]. In their famous paper, the authors studied the growth of the clustering, starting from a primeval Gaussian distribution for the density fluctuations, that was assumed to have a power spectrum with constant *spectral index* n (the precise meaning and the significance of such assumptions well be better explained in following chapters). Under such assumptions, they found a mass function of the type

$$\begin{aligned} n(M) &= \frac{1}{\sqrt{2\pi}} \frac{\rho_{\rm M}}{M_o} \left(1 + \frac{n}{3}\right) \left(\frac{M}{M_o}\right)^{-\left(\frac{3}{2} - \frac{n}{6}\right)} \times \\ &\times \; exp\left[-\frac{1}{2}\left(\frac{M}{M_o}\right)^{1+\frac{n}{3}}\right] \frac{dM}{M_o} \end{aligned} \tag{1.31}$$

(here M_o represents a suitable mass–scale that we will define in the following). A remarkable feature of the expression (1.31) is that it is given by a power–law shape times an exponential cut–off and looks quite similar to the Schechter function (1.24).

[2] Here the *density parameter* $\Omega_o = \rho_o/\rho_c$ represents the ratio between the present mean matter density ρ and the closure density $\rho_c = 1.9 \times 10^{-29} \Omega\, h^2\, g\, cm^{-3}$.

Such an agreement between the Press & Schechter results on the mass function and observational indications on the luminosity function is however valid only at a qualitative level. In fact, a comparison between the above expressions for the luminosity function of galaxies and galaxy systems, as deduced from data samples, and the Press–Schechter model (1.31) shows that for a constant M/L ratio, no value of the spectral index n give the correct values for α. In Chapter 4 we will give an expression for the mass function that is proved to be valid for any galaxy systems and that is deducible on the basis of a more general theoretical ground.

Chapter 2

Statistical methods

2.1 Density field and correlation functions

Let us consider a reference frame in the Universe for which the homogeneity and isotropy hypothesis holds. In this case, the line element turns out to be

$$ds^2 = c^2\,dt^2 - a^2(t)\Big[\frac{dr^2}{1-r^2/R^2} + r^2\,d\Omega^2\Big] \tag{2.1}$$

(see, *e.g.*, refs. [202,104]). In eq. (2.1), the quantity

$$d\Omega^2 = sin^2\varphi\,d\vartheta^2 + d\varphi^2 \tag{2.2}$$

represents the solid angle element, while R^{-2} is a constant. With a suitable redefinition of the units of r, we can need to consider for R^{-2} only the values $0, \pm 1$. Moreover, in eq. (2.1) we introduced the *scale factor* $a(t)$, that describes the behaviour of the expansion of the Universe. Integration of the Friedmann equations

$$\begin{aligned}\left(\frac{\dot{a}}{a}\right)^2 &= \frac{8}{3}\pi G\rho - \frac{k}{a^2} \\ -\frac{\ddot{a}}{a} &= \frac{4}{3}\pi G(\rho + 3p)\,.\end{aligned} \tag{2.3}$$

gives the expression for $a(t)$, once the equation of state, that relates the pressure p and the energy density ρ, is specified. From a heuristic point of view, the Friedmann equations (2.3) can be seen as the relativistic equivalent of the energy conservation principle and of the second law of dynamics in classical mechanics.

In the frame of a Friedmanian universe, let us consider a set of point–like objects. We indicate by x_i the position vector of the i–th object, as deducible from its spatial coordinates (r, ϑ, φ) at the time t. In order to describe the large–scale

structure of the Universe, the objects to be considered are cosmic structures like galaxies or galaxy systems (groups, clusters, superclusters).

In view of the following considerations, such objects are taken as identical to each other and, in particular, as having the same mass. Thus, it is convenient to express their spatial density by means of a point–like distribution

$$\rho(x) = \sum_i \delta^{(3)}(x - x_i) \tag{2.4}$$

[not to be confused with the energy density introduced in eqs. (2.3)], and having dimensions $[L^{-3}]$. Consequently,

$$< \rho(x) > = \Pi^{(1)} = n \tag{2.5}$$

represents the mean value of the distribution, *i.e.* the object number density [in eq. (2.5) $< \cdot >$ indicates a spatial average], and

$$\delta P = \Pi^{(1)} \delta V \tag{2.6}$$

expresses the probability of finding an object in the volume element δV [151]. Such a volume can be considered infinitesimal in the same way that we consider the objects as point–like. This is completely analogous to what is usually done in the study of a macroscopic fluid, where, despite the existence of a microscopic structure, only infinitesimal volumes or points are considered. In our case, the microscopic structure is chosen to include galaxies or galaxy clusters as points. Consequently, such assumption permits us to treat in eq. (2.6) the probability of finding more than one object in δV as an infinitesimal of higher order.

In analogy with section 1.2, let us introduce the joint probability

$$\delta^{(2)} P = \Pi^{(2)}(x_1, x_2)\, \delta V_1\, \delta V_2 \tag{2.7}$$

that each of the two volumes δV_1 and δV_2 (centered at x_1 and x_2 respectively) contains an object. Taking

$$\Pi^{(2)}(x_1, x_2) = n^2[1 + \xi^{(2)}(x_1, x_2)]\,, \tag{2.8}$$

the adimensional quantity $\xi^{(2)}(x_1, x_2)$ represents the 2*–point correlation function.* Under the hypothesis of a homogeneous and isotropic Universe, this depends only on the separation $r = |x_1 - x_2|$. The physical meaning of $\xi^{(2)}$ lies in the fact that it indicates how much the distribution differs from a completely random (Poissonian) process. In fact, for a Poissonian distribution the probability of having an object in δV_1 does not affect the probability of having another object in δV_2, so that eq. (2.8) becomes

$$\Pi^{(2)}(x_1, x_2) = [\Pi^{(1)}]^2 = n^2\,. \tag{2.9}$$

Thus, a completely random distribution is reflected in a vanishing two–point correlation function, for any value of the separation r. On the other hand, if the positions of 2 objects are correlated (*i.e.*, the presence of one of them influences positively the presence of the other), it follows that $\xi^{(2)} > 0$, while $-1 \leq \xi^{(2)} < 0$ if the two positions are anticorrelated.

In a similar way, from eqs. (2.6) and (2.7) we get the expression

$$\delta^{(2)}P(1|2) \;=\; \frac{\delta^{(2)}P(1,2)}{\delta^{(1)}P(1)} \;=\; \frac{\Pi^{(2)}(1,2)}{\Pi^{(1)}(1)}\,\delta V_2 \tag{2.10}$$

for the conditioned probability of finding an object in δV_1, given the presence of another object in δV_2.

More generally, we can define the N–point correlation function through the joint probability

$$\delta^{(N)}P \;=\; \Pi^{(N)}(x_1,...,x_N)\,\delta V_1...\delta V_N \tag{2.11}$$

that each of the volume elements $\delta V_1,...,\delta V_N$ contains an object.

For $N = 3$, this is

$$\delta^{(3)}P \;=\; \Pi^{(3)}(x_1,x_2,x_3)\,\delta V_1\,\delta V_2\,\delta V_3\,. \tag{2.12}$$

In order to study the structure of the 3–point correlation function, let us suppose that the object in x_3 is sufficiently far away from x_1 and x_2 so that the probability of finding an object in δV_3 does not depend on the presence of the other two objects in δV_1 and δV_2. If this is the case, eq. (2.1) modifies into

$$\delta^{(3)}P \;=\; [\Pi^{(2)}(x_1,x_2)\,\delta V_1\,\delta V_2]\times[\Pi^{(1)}\,\delta V_3]\,. \tag{2.13}$$

Hence, requiring symmetry for the exchange of x_3 with x_1 and with x_2, according to eqs. (2.8) and (2.11) the 3–point probability can be expressed in the form

$$\begin{aligned}&\Pi^{(3)}(x_1,x_2,x_3) \;=\\ &=\; n^3[1+\xi^{(2)}(x_1,x_2)+\xi^{(2)}(x_2,x_3)+\xi^{(2)}(x_3,x_1)+\zeta(x_1,x_2,x_3)]\end{aligned} \tag{2.14}$$

In eq. (2.14), $\zeta(x_1,x_2,x_3)$ represents the adimensional term connecting the 3 points all together. Consequently, it must have the property

$$\zeta(x_i,x_j,x_l\to\infty) \;=\; 0 \qquad i\neq j\neq l \quad ; \quad i,j,l=1,2,3\,. \tag{2.15}$$

A graphic representation of eq. (2.14) is

$$\Pi^{(3)}(x_1,x_2,x_3) \;=\; n^3\Big[1+\;\cdot\!\!-\!\!\cdot\;+\;\cdot\!\!/\!\!\cdot\;+\;\cdot\!\!\diagdown\!\!\cdot\;+\;\triangle\;\Big], \tag{2.16}$$

where each leg represents a $\xi^{(2)}$ term, while the triangle corresponds to ζ.

Notice that all the above considerations are completely general and hold for any statistical system. For example, in the case of a dilute gas, the typical situation is that $1 \gg \xi^{(2)} \gg \zeta$. Viceversa, for the distribution of galaxies we have seen in Chapter 1 that the dominant term at small distances in eq. (2.14) is $\zeta \gg \xi^{(2)} \gg 1$.

On the basis of the same considerations that led us to eq. (2.14), we can write the 4–point joint probability in the form

$$\begin{aligned} \Pi^{(4)}(x_1,x_2,x_3,x_4) &= n^4\{1+[\xi^{(2)}(x_1,x_2)+...+6\ terms]+ \\ &+ [\zeta(x_1,x_2,x_3)+...+4\ terms]+\xi^{(4)}(x_1,x_2,x_3,x_4)\} \end{aligned} \quad (2.17)$$

Here the fourth–order correlation function

$$\begin{aligned} &\xi^{(4)}(x_1,x_2,x_3,x_4) = \\ &= \xi^{(2)}(x_1,x_2)\xi^{(2)}(x_3,x_4)+\xi^{(2)}(x_2,x_3)\xi^{(2)}(x_1,x_4)+\xi^{(2)}(x_1,x_3)\xi^{(2)}(x_2,x_4)+ \\ &+\eta(x_1,x_2,x_3,x_4) \end{aligned} \quad (2.18)$$

represents the term connecting the 4 points. In more detail, it contains 3 terms connecting separately two pairs, and the η term connecting all the four point together. Graphically, eq. (2.18) takes the form

$\xi^{(4)}(x_1,x_2,x_3,x_4)$ = 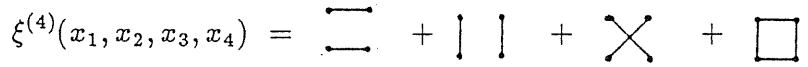 . (2.19)

In general, for the N–point correlations we have that

$$\Pi^{(N)}(x_1,...,x_N) = n^z[1+(n<Npoint)+\xi^{(N)}_{dis}(x_1,...,x_N)] \quad (2.20)$$

where the *disconnected* N–point correlation function is

$$\xi^{(N)}_{dis}(x_1,...,x_N) = (N-point\ disconnected\ terms)+\xi^{(N)}_{con}(x_1,...,x_N)\,. \quad (2.21)$$

In such expression $\xi^{(N)}_{con}(x_1,...,x_N)$ represents the *connected* N–point correlation function that links all the N point simultaneously. For $N=3$ eq. (2.14) becomes $\xi^{(3)}_{dis}(x_1,x_2,x_3)=\xi^{(3)}_{con}(x_1,x_2,x_3)=\zeta(x_1,x_2,x_3)$, and, for $N=4$, $\xi^{(4)}_{con}(x_1,x_2,x_3,x_4)=\eta(x_1,x_2,x_3,x_4)$.

The importance of the correlation functions lies in the fact that their expressions, deducible from observational data, determine completely the statistics of the system under investigation. Viceversa, the explicit expression for $\xi^{(N)}_{con}$ can only be written once the distribution function of the system is known.

An example of N–point disconnected correlation function is given by the *so–called* Kirkwood superposition [114]

$$\xi^{(N)}_{con}(x_1,...,x_N) = [1+\xi^{(2)}(x_1,x_2)]\times...\binom{N}{2}\ terms\,, \quad (2.22)$$

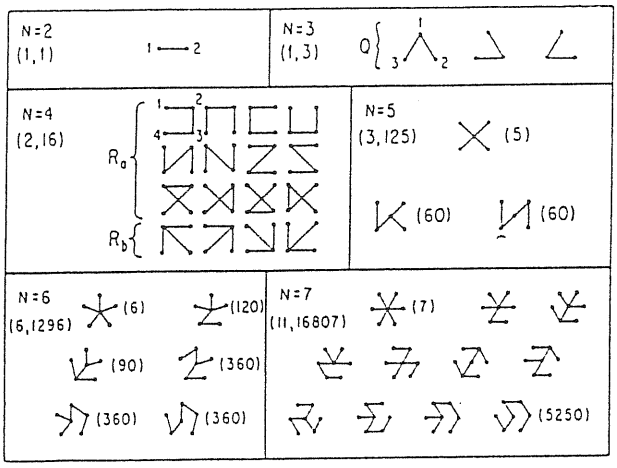

Figure 2.1: *Tree graphs contributing to the hierarchical expression (2.23) for $N = 2$ to 7. The pair of numbers below each N indicates the number of free trees and the number of labeled trees (see Table 2.1); a number in parentheses next to a graph indicates the number of distinct labelings (after [81]).*

that was originally introduced in the study of rarefied gases.

Another popular expression in cosmological context is the hierarchical pattern [81]

$$\xi^{(N)}_{con}(x_1,...,x_N) = \sum_{N-trees}^{t_N} \sum_{a} Q_{N,a} \sum_{labelings} \prod_{edges}^{(N-1)} \xi^{(2)}_{AB} \qquad (2.23)$$

in which the N–point connected function is expressed in terms of products of $(N-1)$ 2–point functions. In eq. (2.23), distinct "trees" designated by a have in general different coefficients Q_a, but configurations that differ only in interchange of labels 1,...,N all have the same amplitude coefficients, and AB is a single index which identifies links (see Figure 2.1). The number of trees t_N with N vertices is a result of combinatorial analysis [172], while the total number of labeled trees is $T_N = N^{N-2}$. Thus, eq. (2.23) has t_N amplitude coefficients ($a = 1,...,t_N$) and T_N total terms. Table 2.1 lists values of t_N and T_N up to $N = 10$. This shows that the 3–point function has one amplitude Q and three total terms; the 4–point function has two amplitudes, R_a and R_b, and 16 total terms. [The hierarchical pattern (2.23) will be widely used in Chapter 5 for the investigation of the correlation properties of the background matter]. Such a hierarchical pattern is quite interesting, because it is also predicted by several dynamical models of gravitational clustering such as the BBGKY equations in the statistical relaxation regime [53,151,79,80,100], or perturbative analysis for non–linear evolution of the fluctuations [81].

Table 2.1
Counting tree graphs

N	(trees) t_N	(labeled trees) $T_N = N^{N-2}$
1	1	1
2	1	1
3	1	3
4	2	16
5	3	125
6	6	1296
7	11	16807
8	23	262144
9	47	4782969
10	106	100000000

As a concluding remark, it is to be stressed that for increasing correlation orders it becomes more and more difficult to detect signals for $\xi^{(N)}(x_1, ..., x_N)$ from a homogeneous galaxy sample, so that it is often hard to distinguish between different statistical models.

2.2 Elements of functional methods

In this section we will introduce some fundamental concepts of functional methods that are widely employed in statistical mechanics. In particular we will emphasize their application to the study of the distribution of galaxies and clusters of galaxies. For this aim, in the following we give a series of definitions and relations having immediate applicability, instead of describing an extremely rigorous formalism.

2.2.1 The concept of functional

Let us consider the space $\mathcal{F}$ of the real functions $q(x)$ belonging to $L^2(D)$ (*i.e.*, having a Lebesgue–integrable square modulus over the domain D) [206]. For what follows, it is useful to introduce in $\mathcal{F}$ the concepts of *norm* and of *scalar product.*

Thus, let

$$q^2 = \int_D dx\, |q(x)|^2$$

be the square of the *norm* of $q(x)$, while, given $q_1(x), q_2(x) \in \mathcal{F}$, let

$$q_1 \cdot q_2 \equiv \int_D dx\, q_1(x)\, q_2(x)$$

be the *scalar product* of 2 functions. Moreover, let $\{\phi_n(x)\}$ be a complete orthonormal basis for $\mathcal{F}$, such that

$$\int_D dx\, \phi_n(x)\, \phi_m(x) = \delta_{nm} \qquad (orthonormality)\,, \tag{2.24}$$

$$\sum_n \phi_n(x)\, \phi_n(y) = \delta(x-y) \qquad (completeness)\,. \tag{2.25}$$

Then, $q(x)$ can be expanded according to

$$q(x) = \sum_n q_n\, \phi_n(x)\,, \tag{2.26}$$

where the coefficients of the expansion are

$$q_n(x) = \int_D dx\, \phi_n(x)\, q(x)\,. \tag{2.27}$$

We define *functional* $F[q(x)]$ as a mapping from $\mathcal{F}$ to the space of the real or complex numbers. Particularly simple examples are the linear functional

$$F[q(x)] = \int_{D_1} dx\, f(x)\, q(x) \tag{2.28}$$

and the bilinear functional

$$F[q(x)] = \int_{D_1} dx \int_{D_2} dy\, q(x)\, K(x,y)\, q(y)\,, \tag{2.29}$$

being $D_1, D_2 \subseteq D$. Many properties of the functionals can be deduced from those of ordinary functions of several variables. In particular it is possible to introduce the concept of functional starting from a description in which we refer to a finite number of independent variables, that form a discrete set.

If it is possible to introduce in $\mathcal{F}$ a discrete basis, from eq. (2.26) we get

$$F[q] = F\Big[\sum_n q_n\, \phi_n(x)\Big] = \hat{F}(q_1, ..., q_n, ...). \tag{2.30}$$

Then, the choice of an orthonormal basis $\{\phi_n\}$ determines uniquely the expansion coefficients q_n and, consequently, the representation of $F[q(x)]$.

For the linear and the bilinear functionals (2.28) and (2.29), we obtain

$$\hat{F}(q_1, ..., q_n, ...) = \sum_n q_n f_n \tag{2.31}$$

and

$$\hat{F}(q_1, ..., q_n, ...) = \sum_n \sum_m k_{nm} q_n q_m \,, \tag{2.32}$$

respectively, where the coefficients of the expansions are

$$f_n = \int_{D_1} dx\, \phi_n(x)\, f(x) \tag{2.33}$$

$$k_{nm} = \int_{D_1} dx \int_{D_2} dy\, \phi_n(x)\, K(x,y)\, \phi_m(y) \,. \tag{2.34}$$

Alternatively, we can divide the domain of definition of $q(x)$ into small cubes having volume τ. If we choose a point x_i inside each such cube, the function $q(x)$ will be approximately specified by the values $q(x_i) = q_i$ that it takes at these points. In the limit $\tau \to 0$, such a representation for $q(x)$ becomes exact, and

$$F[q] = \lim_{\tau \to 0} \hat{F}(..., q_i, ...) \,. \tag{2.35}$$

2.2.2 The functional derivative

In order to introduce the concept of *functional derivative* for $F[q(x)]$, let us consider a small function $\delta q(x) \in \mathcal{F}$, so that $q(x) + \delta q(x)$ differs from $q(x)$ only in a neighbourhood of $x = y$. Moreover, let

$$\delta\omega = \int dx\, \delta q(x) \tag{2.36}$$

be the volume element in $\mathcal{F}$ contained between $q(x)$ and $q(x) + \delta q(x)$.

Then, we *define* the functional derivative of $F[q]$ as

$$\frac{\delta F}{\delta q(y)} = \lim_{\delta\omega \to 0} \frac{F[q + \delta q] - F[q]}{\delta\omega} \,. \tag{2.37}$$

Taking $\delta q(y) = \delta\omega\, \delta(x - y)$, eq. (2.37) becomes

$$\frac{\delta F}{\delta q(y)} = \lim_{\delta\omega \to 0} \frac{F[q(x) + \delta\omega\, \delta(x-y)] - F[q(x)]}{\delta\omega} \tag{2.38}$$

that, in the particular case $F[q(x)] = q(x)$, reads

$$\frac{\delta q(x)}{\delta q(y)} = \delta(x - y) \,. \tag{2.39}$$

In a similar way, higher order functional derivatives can be introduced.

As an example, let us consider the functional

$$F_n[q] = \int dx_1 ... \int dx_n\, f(x_1, ..., x_n)\, q(x_1) ... q(x_n) \,, \tag{2.40}$$

where $f(x_1,...,x_n)$ is a symmetric function with respect to the variables $x_1,...,x_n$. Differentiating the functional (2.40), we get

$$\frac{\delta F_n}{\delta q(y)} = \int dx_2 ... \int dx_n \, f(y,x_2,...,x_n)\, q(x_2)...q(x_n) + ...$$

$$... + \int dx_1 ... \int dx_{n-1} \, f(x_1,...,x_{n-1},y)\, q(x_1)...q(x_{n-1}) \,. \tag{2.41}$$

Making use of the symmetry of $f(x_1,...,x_n)$ and relabeling the integration variables, we finally obtain

$$\frac{\delta F_n}{\delta q(y)} = n \int dx_1 ... \int dx_{n-1} \, f(x_1,...,x_{n-1},y)\, q(x_1)...q(x_{n-1}) \,. \tag{2.42}$$

Similarly, the higher order derivatives are

$$\frac{\delta^{(m)} F_n}{\delta q(y_1)...\delta q(y_m)} = \frac{n!}{(n-m)!} \times$$

$$\times \int dx_1 ... \int dx_{n-m} \, f(x_1,...,x_{n-m},y_1,...,y_m) q(x_1)...q(x_{n-m}) \qquad (m \leq n)$$

$$\frac{\delta^{(m)} F_n}{\delta q(y_1)...\delta q(y_m)} = 0 \qquad (m > n) \,. \tag{2.43}$$

The concept of functional derivative allows us to introduce the expression of the functional Taylor expansion for $F[q]$. In fact, under the hypothesis that $F[q]$ has derivatives of any order, we can write

$$F[q+\delta q] = F[q] +$$

$$+ \sum_{n=1}^{\infty} \frac{1}{n!} \int dx_1 ... \int dx_n \, \frac{\delta^{(n)} F}{\delta q(x_1)...\delta q(x_n)}\bigg|_{q(x)} \delta q(x_1)...\delta q(x_n). \tag{2.44}$$

Such expressions for the functional series expansion will be of fundamental relevance in the next section, where we define correlation functions as coefficients of the Taylor series of a suitable functional.

2.2.3 The functional integral

Let us consider the function $\hat{F}(...,q_i,...)$, defined in eq. (2.35), and the multiple integral

$$I = \int \{ \prod_i dq_i \} \hat{F}(...,q_i,...) \tag{2.45}$$

In such expressions, the dominion of variation for the variables q_i is uniquely determined by the dominion of variation of $q(x)$ inside the functional space $\mathcal{F}$. Let us suppose that the limit

$$\lim_{\tau \to 0} \int \{ \prod_i dq_i \} \hat{F}(...,q_i,...) \equiv \int D[q(x)]\, F[q(x)] \tag{2.46}$$

exists and is unique. The above relation *defines* the functional integral of $F[q(x)]$ over $\mathcal{F}$, with measure $D[q(x)]$. Notice that the limit $\tau \to 0$ is completely equivalent to passing from an integration over a discrete infinity of variables q_i to an integration over a continuous set of variables $q(x)$.

As an example, let us consider the *Gaussian* functional

$$F[q] \;=\; N\, e^{-\frac{1}{2}\int dx \int dx'\, q(x) A(x,x') q(x')}\,, \tag{2.47}$$

where $A(x,x')$ is an hermitean operator acting on $\mathcal{F}$. We show how the integral of the functional (2.47) can be evaluated in analogy with the integral of a n–dimensional Gaussian function. In fact, in one dimension it is

$$\frac{1}{\sqrt{2\pi}} \int_{-\infty}^{+\infty} e^{-\frac{1}{2}\lambda q^2} dq \;=\; \frac{1}{\sqrt{\lambda}}\,, \tag{2.48}$$

while the n–dimension case gives

$$\frac{1}{(2\pi)^{n/2}} \int_{-\infty}^{+\infty} dq_1 ... \int_{-\infty}^{+\infty} dq_n\, e^{-\frac{1}{2}\sum_{l,k} a_{lk} q_l q_k} \;=\; (det\ A)^{-1/2}\,. \tag{2.49}$$

In this equation, the matrix elements a_{lk} are real and symmetric under the exchange of the indices, and $\sum_{l,k} a_{lk} q_l q_k$ is a positive–definite quadratic form. Moreover, the a_{lk}'s are the entries of the matrix representation of the operator A with respect to a finite basis of a subspace of $\mathcal{F}$. In order to prove eq. (2.49) let us consider the integral

$$Z(j) \;=\; \int_{-\infty}^{+\infty} dq_1 ... \int_{-\infty}^{+\infty} dq_n\, e^{-\frac{1}{2}\sum_{l,k} a_{lk} q_l q_k + i\sum_l j_l q_l} \tag{2.50}$$

where the quantities b_l are real numbers. Let us now introduce the notation $(q_1, ..., q_n) = \mathbf{q}$, $(j_1, ..., j_n) = \mathbf{j}$, $(a_{lk}) = A$ and define the vector $\mathbf{y} = iA^{-1}\mathbf{j}$. With the position $\mathbf{q} = \mathbf{y} + \mathbf{z}$ and after some calculations, the exponent in eq. (2.50) becomes

$$-\frac{1}{2}(\mathbf{q}, A, \mathbf{q}) + i(\mathbf{j}, \mathbf{q}) \;=\; -\frac{1}{2}(\mathbf{z}, A, \mathbf{z}) - \frac{1}{2}(\mathbf{j}, A^{-1}, \mathbf{j})\,. \tag{2.51}$$

After substituting in the integral (2.50), we have

$$Z(j) \;=\; e^{-\frac{1}{2}\sum_{l,k} a^{-1}_{lk} j_l j_k} \int_{-\infty}^{+\infty} dz_1 ... \int_{-\infty}^{+\infty} dz_n\, e^{-\frac{1}{2}\sum_{l,k} a_{lk} z_l z_k}\,. \tag{2.52}$$

Let us now diagonalize the matrix (a_{lk}) by means of the orthogonal transformation $z_l = \sum_k b_{lk}\alpha_k$, in such a way that $\sum_{lk} a_{lk} z_l z_k \;=\; \sum_l \lambda_l \alpha_l^2$, with λ_l the eigenvalues of A. The Jacobian of an orthogonal transformation being equal to one and since $\prod_{l=1}^{n} \lambda_l = det\, A$, the integral $Z(j)$ becomes

$$\frac{1}{(2\pi)^{n/2}} \int_{-\infty}^{+\infty} dq_1 ... \int_{-\infty}^{+\infty} dq_n\, e^{-\frac{1}{2}\sum_{l,k} a_{lk} q_l q_k + 1\sum_l j_l q_l} \;=\; \frac{e^{-\frac{1}{2}\sum_{l,k} a^{-1}_{lk} j_l j_k}}{(det\ A)^{1/2}} \tag{2.53}$$

Then, eq. (2.49) follows, taking $j_l = 0$ in the above expression.

In analogy with these results, the functional integral of the Gaussian functional (2.47) becomes

$$\int D[q(x)]\, e^{-\frac{1}{2}\int dx \int dx'\, q(x)A(x,x')q(x')} \;=\; (det\, A)^{-1/2}\,. \tag{2.54}$$

In this expression, the substitution of the sums over the discrete indices l, k with the integrals over the continuous variables x, x' is due to the fact that the functional integral has been obtained as a limit starting from an ordinary integral over n variables.

2.3 Functional methods for correlation functions

Other than the density field $\rho(x)$ introduced in Section 2.1, let us consider the relative fluctuations described by the *contrast–density* field

$$\delta(\mathbf{x}) \;=\; \frac{\rho(\mathbf{x}) - <\rho>}{<\rho>} \tag{2.55}$$

According to this definition, the fluctuation field (2.55) has the properties $\delta(\mathbf{x}) \geq -1$ and $<\delta(\mathbf{x})> = 0$.

It is easy to show that the n–point disconnected correlation function for the density field $\rho(\mathbf{x})$ is directly related to the contrast–density field, according to

$$\xi^{(n)}_{dis}(x_1, ..., x_n) \;=\; <\delta(x_1)...\delta(x_n)>\,. \tag{2.56}$$

In fact, let us consider the space $\mathcal{F}$ of the functions $\delta(\mathbf{x})$ that satisfy the two above properties. Moreover, let $P[\delta(\mathbf{x})]$ be the probability that the density fluctuation field is described by a given $\delta(\mathbf{x}) \in \mathcal{F}$. By definition, such a probability distribution in the functional space must be be normalized so that the total probability is unity, that is

$$\int D[\delta(x)]\, P[\delta(x)] \;=\; 1\,. \tag{2.57}$$

Given a generic function $J(x)$ with finite norm, we define the *partition functional*

$$Z[J] \;=\; \int D[\delta(x)]\, P[\delta(x)]\, e^{i\int dx\, \delta(x)J(x)}\,. \tag{2.58}$$

It is easy to show that, such a functional represents the continuum limit of the integral (2.50), once we substitute the Gaussian functional (2.47) with a generic $P[\delta(x)]$. In eq. (2.58), $J(x)$ play the role of an external source, which perturbs the distribution $P[\delta(x)]$ [80,134]. Then, according to the definitions of $P[\delta(x)]$ and of $Z[J(x)]$, we get

$$<\delta(x)> = \int D[\delta(x)]\, P[\delta(x)]\, \delta(x) \;=\; i^{-1}\frac{\delta Z}{\delta J(x)}\bigg|_{J=0} \;=\; 0\,. \tag{2.59}$$

The above relation ensures the vanishing of the first derivative of the partition functional, evaluated in absence of external source. It should be observed that in eq. (2.59) we used the symbol $< \cdot >$ to indicate an average over the space $\mathcal{F}$. However, under the hypothesis of *ergodicity*, the averages taken over the (physical) configuration space are completely equivalent to the expectations taken over an ensemble of *universes, i.e.* over the functional space $\mathcal{F}$. Thus, from now on we will use the symbol $< \cdot >$ to indicate indifferently one or the other kind of average.

Let us now consider the n–point joint probability

$$\begin{aligned} \Pi^{(n)}(x_1, ..., x_n) &\equiv < \rho(x_1)...\rho(x_n) > = \\ &= \int D[\delta(x)]\, P[\delta(x)]\, \rho(x_1)...\rho(x_n) \end{aligned} \tag{2.60}$$

that at the points $x_1, ..., x_n$ the density field takes the values $\rho(x_1), ..., \rho(x_n)$. Then, according to the definition (2.55) of density–contrast field,

$$\begin{aligned} \Pi^{(n)}(x_1, ..., x_n) &= \int D[\delta(x)]\, P[\delta(x)] < \rho >^n [1 + \delta(x_1)]...[1 + \delta(x_n)] = \\ &= < \rho >^n \{1 + [< \delta(x_1)\delta(x_2) > + ...] + ... \\ &\quad [< \delta(x_1)...\delta(x_{n-1}) > + ...] + < \delta(x_1)...\delta(x_n) >]\} \end{aligned} \tag{2.61}$$

Taking into account the definition (2.21) for the disconnected correlation function, we finally obtain the fundamental relation

$$\xi^{(n)}_{dis}(x_1, ..., x_n) = < \delta(x_1)...\delta(x_n) > = i^{-n} \frac{\delta^{(n)} Z}{\delta J(x_1)...\delta J(x_n)}\bigg|_{J=0} . \tag{2.62}$$

According to eq. (2.62), the McLaurin functional series for the partition functional reads

$$\begin{aligned} Z[J] &= 1 + \sum_{n=2}^{\infty} \frac{1}{n!} \int_{-\infty}^{+\infty} dx_1 ... \int_{-\infty}^{+\infty} dx_n \, \frac{\delta^{(n)} Z}{\delta J(x_1)...\delta J(x_n)}\bigg|_{J=0} J(x_1)...J(x_n) = \\ &= 1 + \sum_{n=2}^{\infty} \frac{i^n}{n!} \int_{-\infty}^{+\infty} dx_1 ... \int_{-\infty}^{+\infty} dx_n \, \xi^{(n)}_{dis}(x_1, ..., x_n) J(x_1)...J(x_n) . \end{aligned} \tag{2.63}$$

Thus, $Z[J]$ represents the generating functional of the disconnected correlation functions, in the sense that such functions can be defined as the coefficients of the McLaurin expansion of $Z[J]$ itself.

In a similar way, we can also characterize the connected correlation functions as coefficients of the McLaurin expansion of a suitable generating functional. In fact, let us consider the functional

$$W[J(x)] = ln\, Z[J(x)] . \tag{2.64}$$

According to an important theorem of combinatorial analysis [163], it is possible to express the connected correlation functions as

$$\xi^{(n)}_{con}(x_1,...,x_n) \;=\; i^{-n}\frac{\delta^{(n)}}{\delta J(x_1)...\delta J(x_n)}W[J]\Big|_{J=0}\,. \tag{2.65}$$

The proof of this theorem is rather tricky and will not be reported here. However, in order to show how this theorem works, we check the validity of eq. (2.62) for the particular case $n = 4$, that represents the lowest order at which connected and disconnected correlation functions differ. Indeed, differentiating explicitly $W[J]$, we have

$$\begin{aligned}
\frac{\delta^{(4)}}{\delta J(x_1)...\delta J(x_4)}W[J]\Big|_{J=0} \;&=\; \frac{1}{Z[J]}\frac{\delta^{(4)}Z}{\delta J(x_1)...\delta J(x_4)}\Big|_{J=0} + \\
-\;&\Big(\frac{1}{Z^2[J]}\frac{\delta^{(2)}Z}{\delta J(x_1)\delta J(x_2)}\frac{\delta^{(2)}Z}{\delta J(x_3)\delta J(x_4)} + ...3\ \ terms\Big)\Big|_{J=0} \;= \\
=\;&\xi^{(4)}_{dis}(x_1,x_2,x_3,x_4) - [\xi^{(2)}(x_1,x_2)\xi^{(2)}(x_3,x_4) + ...3\ \ terms] \;= \\
=\;&\xi^{(4)}_{con}(x_1,x_2,x_3,x_4)\,.
\end{aligned} \tag{2.66}$$

Thus, the effect of differentiating $W[J]$ instead of $Z[J]$ is to subtract all the lower-order disconnected terms from $\xi^{(n)}_{dis}(x_1,...,x_n)$.

Accordingly, the McLaurin functional expansion

$$ln\,Z[J] \;=\; \sum_{n=2}^{\infty}\frac{i^n}{n!}\int_{-\infty}^{+\infty}dx_1...\int_{-\infty}^{+\infty}dx_n\,\xi^{(n)}_{con}(x_1,...,x_n)J(x_1)...J(x_n) \tag{2.67}$$

can be considered as completely alternative to the one for $Z[J]$.

The functional series (2.63) and (2.67) show that correlation functions determine uniquely the partition functional and, consequently, the statistics of the system too.

2.4 The spectrum of the fluctuations

It is often very useful in the analysis of the density fluctuation modes to give a representation of the correlation functions in the momentum space. For this purpose, let us define

$$\tilde{\delta}(k) \;=\; \int\frac{d^3x}{(2\pi)^{3/2}}\delta(\mathrm{x})\,e^{i\mathrm{k}\cdot\mathrm{x}} \tag{2.68}$$

as the Fourier transform of the field $\delta(\mathrm{x})$. In eq. (2.68), $k = 2\pi a(t)/\lambda$ is the comoving wave number, expressed in terms of the wavelength λ of the fluctuation. Under the

hypothesis of homogeneity and isotropy, we will have dependences only on $k \equiv |\mathbf{k}|$. According to the expression (2.62) for the 2–point correlation function, we have

$$< |\tilde{\delta}(k)|^2 > \equiv$$
$$\equiv \int \frac{d^3k_1}{(2\pi)^{3/2}} \frac{d^3k_2}{(2\pi)^{3/2}} \int D[\delta(\mathbf{x})]P[\delta(\mathbf{x})]\, \delta(\mathbf{x}_1)\delta(\mathbf{x}_2)e^{-i(\mathbf{k}_1\cdot\mathbf{x}_1+\mathbf{k}_2\cdot\mathbf{x}_2)} =$$
$$= \int D[\delta(\mathbf{x})]P[\delta(\mathbf{x})] \int \frac{d^3k_1}{(2\pi)^{3/2}} \frac{d^3k_2}{(2\pi)^{3/2}} \delta(\mathbf{x}_1)\delta(\mathbf{x}_2)e^{-i(\mathbf{k}_1\cdot\mathbf{x}_1+\mathbf{k}_2\cdot\mathbf{x}_2)}. \quad (2.69)$$

In the above relation, we introduced the *power spectrum* $< |\tilde{\delta}(k)|^2 >$ as the Fourier transform of the 2–point correlation function. Such a quantity is of fundamental importance, any theoretical prediction on its shape being directly comparable with the observed $\xi^{(2)}$, according to eq. (2.69).

However, the evolution of density fluctuations turns out to be dependent both on epoch and on scale, so that the resulting fluctuation spectrum will change its slope as the cosmic expansion goes on. For this reason, the theoretical determination of the power spectrum at the present epoch starts from the assumption of a primordial spectral distribution at a given redshift z_{pr}. In particular, we take $z_{pr} \gg z_{eq}$ (z_{eq}: redshift of the equivalence epoch, at which the non–relativistic matter density starts to dominate the cosmic expansion) and assume

$$< |\tilde{\delta}_{pr}(k)|^2 > = Ak^n. \quad (2.70)$$

The value $n = 1$ for the *spectral index* (Harrison–Zel'dovich spectrum [101,207]) is usually preferred, according to the idea that primeval perturbations originated at the inflationary stage [99,123,124] (see, however, refs. [164,126] for generalized inflationary models that predict $n < 1$). Moreover, in eq. (2.70) the proportionality constant A represents the amplitude of the fluctuation spectrum and its value is fixed once a suitable normalization prescription is assigned.

The power law (2.70) for the spectrum gives in turn a power law for the 2–point correlation function. Indeed, inverting eq. (2.69), we get

$$\xi^{(2)}(r) = \frac{A}{(2\pi)^3} \int d^3k\, k^n e^{i\mathbf{k}\cdot\mathbf{r}} = \frac{A}{2\pi^2} \int_0^{+\infty} dk\, k^{n+2} \frac{sin\, kr}{kr} =$$
$$= \frac{A}{2\pi^2} \frac{\Gamma(n+3)}{n+2} sin\left[\frac{(n+2)\pi}{2}\right] r^{-(n+3)}. \quad (2.71)$$

However, due to the successive evolution of the fluctuations, the slope of the power spectrum (2.69) is left unchanged only for $k < k_{eq}$, where k_{eq} is the wave vector corresponding to the size of the horizon at the equivalence [19]. On the contrary, the shape of the spectrum at grater wavenumbers $k > k_{eq}$ crucially depends on the kind of dark matter (DM) particles dominating the mean density of the universe. In

general, over the scales where linear gravitational evolution still represents a good approximation, the power spectrum can be expressed in the form

$$< |\tilde{\delta}(k)|^2 > = T^2(k) < |\tilde{\delta}_{pr}(k)|^2 > . \tag{2.72}$$

Here $< |\tilde{\delta}_{pr}(k)|^2 >$ corresponds to the primordial power spectrum (2.70). The *transmission function* $T(k)$ is such that $T(k) = 1$ for $k < k_{eq}$, while its shape for $k > k_{eq}$ depends on the weakly interacting particles which dominates the DM content of the Universe. In fact, the most important characteristic of such particles is the value of their thermal velocities. This is because all density perturbations with scales less than the horizon size damp completely at the relativistic stage due to free streaming [63]. In contrast, once nonrelativistic, DM particles begin to slow down and become a dust–like medium. At this stage, surviving density perturbations grow at the rate $\delta\rho/\rho \propto a$ if nonrelativistic particles dominate the cosmic mean density [151]. Otherwise, perturbations, while not completely damped, remain stagnant (Meszaros effect, [137]) up to the equivalence epoch corresponding to the redshift

$$1 + z_{eq} \simeq 4 \times 10^4 \Omega h^2 (1 + 0.68 N_\nu) \tag{2.73}$$

(N_ν is the number of massless neutrino species). To summarize, all perturbations on scales smaller than the horizon damp when weakly interacting particles become nonrelativistic, and the spectrum of perturbations acquires a sharp cutoff at short wavelengths. This shows how important it is to distinguish between scenarios dominated by DM particles that derelativize at largely different cosmic epoch. The value of the cutoff scale is a very important parameter characterizing the formation of large scale structure, as it determines the scale of the first structure that undergoes non–linearity and the time–sequence of the formation of large scale structure.

In the following subsections we describe the main features of the fluctuation evolution in the two popular scenarios of *hot dark matter* (HDM) and *cold dark matter* (CDM) dominated universes. However, we will not enter in the details of the computations and the physical motivations, that are at the basis of such scenarios (see, *e.g.*, refs. [168,20,19] for detailed reviews).

2.4.1 Hot dark matter (HDM)

DM particles are defined to be *hot* if they derelativize when the mass contained inside the horizon is much greater than the galaxy mass–scale ($\sim 10^{11} M_\odot$). Neutrinos are an example of HDM, because they become non relativistic at a rather low redshift

$$1 + z_\nu \simeq 6 \times 10^4 \frac{m_\nu}{30\, eV} , \tag{2.74}$$

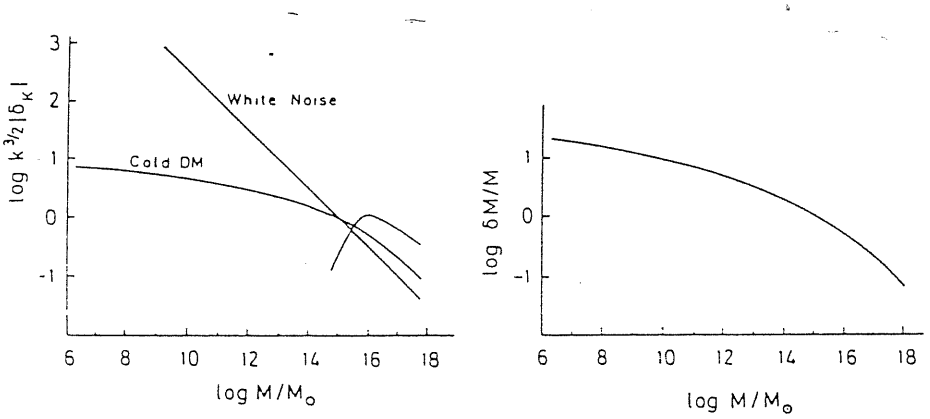

Figure 2.2: *Left panel: density fluctuation spectra as a function of the wavenumber k for isothermal white noise ($n = 0$), and adiabatic Zel'dovich ($n = 1$) neutrino and CDM spectra; right panel: mass fluctuation within a randomly placed sphere containing mass M for CDM spectrum (after [20]).*

m_ν being the neutrino mass in eV. It is interesting to note that z_{eq} is close to z_ν for m_ν several tens of eV. Thus, in a neutrino–dominated Universe, the spectrum has in practice only one characteristic scale.

At the redshift z_ν, the mass contained inside the horizon,

$$M_\nu \sim 2 \times 10^{15} \left(\frac{m_\nu}{30\, eV} \right) M_\odot \,, \tag{2.75}$$

represents the mass of the smallest surviving structure and is several orders of magnitude above the galaxy mass scale. This means that HDM cosmological models lead to the so–called *top–down* scenario in which the first structure to form are pancakes of supergalactic sizes, while galaxies are originated later by fragmentation of pancakes [64,185].

Detailed numerical computations for the evolution of adiabatic fluctuations in a massive–neutrino HDM scenario were performed by Peebles [152], while an analytical expression for the numerical data on the transmission function was suggested by Bond & Szalay [23] in the form

$$T(k) \propto 10^{-2(k/k_\nu)^{1.5}} \,,$$

$$k_\nu \simeq 0.40 \Omega_o h^2 Mpc^{-1} \,. \tag{2.76}$$

As shown in Figure 2.2, such an expression for the transmission function provides an exponential cut–off for wavenumber $k \gg k_\nu$.

2.4.2 Cold dark matter (CDM)

In the CDM cosmology, the scale of cutoff in the spectrum is too small to be of any importance for large–scale structure formation. A cutoff on small scales can happen for either of two reasons. First, the mass of particles can be so large that they become nonrelativistic very early. Candidates for such kind of DM particles are supersymmetric particles, such as gravitinos and photinos [69], with masses above $1\,GeV$. Second, there can be particles like the axion that never were in thermal equilibrium and have a very low thermal velocity dispersion despite their small masses ($\sim 10^{-5}eV$) [166].

In CDM models, the formation of structures follows the *bottom–up* scenario. It starts with small–scale structure, having mass $\sim 10^6 M_\odot$. Later galaxies form and finally clusters and superclusters.

Also for CDM scenarios, accurate numerical calculations of the spectrum of density perturbations after equivalence were performed [153,154,168]. The most popular expression for the CDM transmission function is given by Bond & Efstathiou [22] in the form

$$T(k) = \frac{1}{1 + ak + bk^{1.5} + ck^2} \tag{2.77}$$

[$a = 1.7(\Omega_0 h^2)^{-1} Mpc$, $b = 9(\Omega_0 h^2)^{-1.5} Mpc^{1.5}$, $c = 1(\Omega_0 h^2)^{-2} Mpc^2$]. According to eq. (2.77), it results $T(k) \simeq 1$ for small k values, due to the fact that perturbations on scales larger than the horizon grow as a^2, also during the radiation dominated era. In contrast, the growth of perturbations of nonrelativistic particles inside the horizon suffer stagnation [137]. This effect produces a bend in the spectrum from the initial spectral index n to $n - 4$ in correspondence to the scale of the horizon at the equivalence (see Figure 2.2).

As a concluding remark, let us observe that the importance of following the evolution of the DM spectrum lies in the fact that it determines the spectrum of the ordinary baryonic matter, after the equivalence epoch. In fact, as the temperature goes down to $T_{rec} \sim 4000\,K$ at the redshift $z_{rec} \sim 1400$, neutral baryonic gas decouples from radiation, the Jeans mass falls to about $10^6 M_\odot$ and all perturbations on larger scales could grow due to gravitational instability [202]. As a consequence, the amplitude of baryonic perturbations after decoupling grows rapidly to match that of the DM fluctuations [96].

2.5 Gaussian fluctuations

Particularly interesting is the case in which the fluctuations in the matter distribution are approximated by a random Gaussian process. This means that the density fluctuations for the matter contained inside a sphere of fixed radius and centered on a randomly chosen point has a frequency distribution of the Gaussian type [151]. Consequently, the distribution of the fluctuation amplitudes also turns out to be Gaussian, with variance determined by the 2–point correlation function.

The very important role of Gaussian perturbations in the matter distribution lies in the fact that they originated from quantum fluctuations of a free scalar field during an early phase of the expansion of the Universe. In fact, the classical scenario of inflationary expansion gives rise to primordial perturbations initially having Gaussian nature. However, several mechanisms had been also suggested for originating non–Gaussianety, still in the frame of inflation [5,117,144], or due to different physical phenomena, such as accretion of matter around cosmic string loops [201,197,16,4], percolation of cosmic explosions [145,203,205] or non–linear dynamics [81].

In the Gaussian case, the probability distribution in the functional space $\mathcal{F}$ is given by

$$P[\delta(x)] \;=\; (det\, K)^{1/2}\, exp\Big\{-\frac{1}{2}\int dx \int dx'\, \delta(x) K(x,x') \delta(x')\Big\}\,. \qquad (2.78)$$

Here $K(x,x')$ in an invertible operator acting on $\mathcal{F}$ and symmetric with respect to the variables x, x'. From eq. (2.78) it follows that such an operator determines the variance of the distribution and, more generally, the correlation properties of the fluctuation field. Let us observe that the above expression of the distribution functional is such that the normalization requirement (2.57) is satisfied. Indeed, making use of eq. (2.54) for the integral of a Gaussian functional, we get

$$(det\, K)^{1/2} \int D[\delta(x)]\, e^{-\frac{1}{2}\int dx \int dx'\, \delta(x) K(x,x') \delta(x')} \;=\; 1\,. \qquad (2.79)$$

Expressing the 2–point correlation function as the second derivative of the partition functional $Z[J]$, evaluated for $J(x) = 0$, we can show that the operator K determines the 2–point function according to

$$\xi^{(2)}(x_1, x_2) \;=\; \int \frac{dk}{(2\pi)^3}\, \frac{e^{ik(x_1 - x_2)}}{\hat{K}(k)}\,. \qquad (2.80)$$

Here $\hat{K}(k)$ is the representation of the operator K in the momentum space, where it acts as a multiplicative operator. In order to prove eq. (2.80), let us observe that the partition functional $Z[J]$ relative to the Gaussian distribution functional (2.78) is

$$Z[J] \;=\; (det\, K)^{1/2}\, e^{-\frac{1}{2}\int dx \int dx'\, J(x) K^{-1} J(x')} \int D[\delta(x)]\, e^{-\frac{1}{2}\int dx \int dx'\, \delta(x) K \delta(x')} \;=$$

$$= e^{-\frac{1}{2}\int dx \int dx' J(x)K^{-1}J(x')} . \tag{2.81}$$

Differentiating two times this expression, the 2–point function reads

$$\xi^{(2)}(x_1,x_2) = -\frac{\delta}{\delta J(x_1)}\frac{\delta}{\delta J(x_2)} e^{-\frac{1}{2}\int dx \int dx' J(x)K^{-1}J(x')}\Big|_{J=0} =$$

$$= [K^{-1}\delta(x_1-x_2) - K^{-2}J(x_1)J(x_2)]\, e^{-\frac{1}{2}\int dx \int dx' J(x)K^{-1}J(x')}\Big|_{J=0} =$$

$$= K^{-1}\delta(x_1-x_2) . \tag{2.82}$$

Eq. (2.80) follows from this expression of $\xi^{(2)}$, after performing the Fourier transform. Moreover, from eq. (2.80) we immediately obtain that the inverse of $\hat{K}(k)$ coincides with the power spectrum $< |\tilde{\delta}(k)|^2 >$.

Let us finally observe that from the expression (2.81) for the partition functional we derive a fundamental property of the Gaussian distribution. In fact, according to the definition (2.64) of $W[J]$, the generator of the connected correlation functions reads

$$W[J] = -\frac{1}{2}\int dx \int dx' J(x)K^{-1}J(x') . \tag{2.83}$$

Then, following the expression (2.65) for the connected functions, we get

$$\xi^{(n)}_{con}(x_1,...,x_n) = 0 \qquad if \quad n \neq 2 . \tag{2.84}$$

Thus, if the density fluctuation field is characterized by a Gaussian distribution, its statistics is completely determined by 2–point correlations only.

2.6 The smoothed fluctuation field

In the study of the large scale distribution of cosmic structures (galaxies or clusters of galaxies) we do not consider the details of such distribution on too small scales. In the case of galaxies, by avoiding to go down to scales of the order $R_g \sim 0.1\, Mpc$ we can neglect all the strongly non–linear dissipative processes, that dominate the dynamics on such small scales. Moreover, when we consider larger structures, the relevant scale R is suitably fixed in such a way that details on scales $< R$ do not influence the overall statistics. For example, in the case of the rich Abell clusters, their distribution can be described by a density field that does not involve fluctuations having wavelength less than $R_c \sim 10 Mpc$.

In order to describe fluctuations on scales exceeding R, let us introduce the *smoothed* fluctuation field

$$\delta_{\rm R}(\mathrm{x}) = \int d^3y\, \delta(\mathrm{x})\, Q_{\rm R}(|\mathrm{x}-\mathrm{y}|) , \tag{2.85}$$

that results from the convolution of the field $\delta(\mathbf{x})$ with the *window* function $Q_{\rm R}(|\mathbf{x}|)$. The effect of $Q_{\rm R}(|\mathbf{x}|)$ is to select the Fourier components of $\delta(\mathbf{x})$ that have frequency $> R^{-1}$. According to the requirement that the window function suitably weight the harmonics of $\delta(\mathbf{x})$, the normalization constraint

$$\int_{-\infty}^{+\infty} d^3x\, Q_{\rm R}(|\mathbf{x}|) \;=\; 1 \tag{2.86}$$

follows.

Typical examples of window functions are given by the *Gaussian filter*

$$Q_{\rm R}(|\mathbf{x}|) \;=\; V_{\rm R}^{-1}\, e^{-\frac{x^2}{2R^2}} \tag{2.87}$$

and by the *top–hat filter*

$$Q_{\rm R}(|\mathbf{x}|) \;=\; V_{\rm R}^{-1}\, \theta\Big[1 - \frac{|\mathbf{x}|}{R}\Big]\,. \tag{2.88}$$

In the above expressions, the constant $V_{\rm R}$ represents the characteristic volume associated with each window. By applying the normalization requirement (2.86) to each of the two above filters, we get

$$V_{\rm R} \;=\; \int d^3x\, e^{-\frac{x^2}{2R^2}} \;=\; (2\pi)^{3/2} R^3 \tag{2.89}$$

and

$$V_{\rm R} \;=\; \int dx^3\, \theta\Big[1 - \frac{|\mathbf{x}|}{R}\Big] \;=\; \frac{4}{3}\pi R^3\,, \tag{2.90}$$

respectively. On the other hand, the expression of the Fourier transform for the Gaussian filter,

$$\hat{Q}_{\rm R}(k) \;=\; e^{-\frac{R^2k^2}{2}}\,, \tag{2.91}$$

and that for the top–hat filter,

$$\hat{Q}_{\rm R}(k) \;=\; \frac{3(sin\, kR - kR cos\, kR)}{(kR)^3}\,, \tag{2.92}$$

show explicitly that the windows (2.87) and (2.88) act as infrared cutoffs, depressing with different efficiency the fluctuations with wavelength $\lambda \ll R$.

Associated to the smoothing scale R, we can also introduce a mass scale $M_{\rm R}$, as the expected mass contained inside the characteristic volume $V_{\rm R}$. Then, the quantity

$$M_{\rm R} \;\equiv <M_{\rm R}> = <\rho>\, V_{\rm R} \tag{2.93}$$

turns out to depend not only on the scale R, but also on the shape of the window function. More generally, the mass contained inside a sphere of radius R and centered at $\mathbf{x}$ reads

$$M_{\rm R}(\mathbf{x}) \;=\; \int d^3x\, \rho(\mathbf{y})\, Q_{\rm R}(|\mathbf{x}-\mathbf{y}|) \;=\; V_{\rm R}\rho_{\rm R}(\mathbf{x})\,, \tag{2.94}$$

where $\rho_{\rm R}(\mathbf{x})$ represents the smoothed density field, defined in analogy with eq. (2.85) [in all these consideration $\rho(\mathbf{x})$ and $<\rho>$ refer to the matter density and not to the object density].

The statistics of the field $\delta_{\rm R}(\mathbf{x})$ is described by the *smoothed* correlation functions

$$\begin{aligned}\xi^{(n)}_{dis,R}(\mathbf{x}_1,...,\mathbf{x}_n) &\equiv <\delta_{\rm R}(\mathbf{x}_1)...\delta_{\rm R}(\mathbf{x}_n)> = \\ &= \int D[\delta(\mathbf{x})]\,P[\delta(\mathbf{x})]\delta_{\rm R}(\mathbf{x}_1)...\delta_{\rm R}(\mathbf{x}_n)\,. \end{aligned} \tag{2.95}$$

Then, according to the definition (2.85) of the smoothed field and after exchanging the functional integral with the 3–dimensional ordinary ones, we obtain

$$\xi^{(n)}_{dis,R}(\mathbf{x}_1,...,\mathbf{x}_n) = \int \left\{\prod_{j=1}^{n} d^3y_j\, Q_{\rm R}(|\mathbf{x}_j-\mathbf{y}_j|)\right\} \xi^{(n)}_{dis}(\mathbf{y}_1,...,\mathbf{y}_n)\,. \tag{2.96}$$

Eq. (2.96) relates explicitly the correlation properties of the smoothed fluctuation field to that of the unsmoothed one. In particular, according to eq. (2.94) the mass variance over the scale R turns out to be

$$\begin{aligned}\sigma^2_{\rm R} &= \left\langle \left(\frac{\rho_{\rm R}(\mathbf{x})- <\rho_{\rm R}>}{<\rho_{\rm R}>}\right)^2 \right\rangle = \\ &= <\delta_{\rm R}(\mathbf{x})\delta_{\rm R}(\mathbf{x})> = \xi^{(2)}_{\rm R}(\mathbf{x},\mathbf{x}) \end{aligned} \tag{2.97}$$

and coincides with the smoothed 2–point correlation function evaluated for null separation. In turn, the behaviour of $\xi^{(2)}_{\rm R}$ is easily obtainable taking eq. (2.96) for $n=2$. In fact, after eliminating the Fourier modes with wavelength $\lambda < R$, we get

$$\xi^{(2)}_{\rm R}(r) = \frac{1}{(2\pi)^{3/2}} \int_0^{\sim 1/R} dk\, <|\tilde{\delta}(k)|^2>\, e^{ikr}\,. \tag{2.98}$$

For $r \ll R$, the exponential term in eq. (2.98) is practically constant (~ 1) in the integration range, so that, for $r \ll R$ any dependence on R disappears and $\xi^{(2)}_{\rm R}(r<R) \simeq \xi^{(2)}(R)$. As a consequence, the mass variance (2.94) depends on the smoothing scale according to $\sigma^2_{\rm R} \simeq \xi^{(2)}(R)$. Viceversa, for $r > R$ eq. (2.98) gives $\xi^{(2)}_{\rm R}(r>R) \simeq \xi^{(2)}(r)$, and, on greater scales, the effect of the smoothing becomes negligible.

Figure 2.3 shows the shape of $\xi^{(2)}_{\rm R}(r)$ for two different values of the smoothing radius and assuming a power law for the power spectrum. In particular, for a power spectrum with spectral index n,

$$\sigma^2_{\rm R} \propto R^{-(n+3)}\,. \tag{2.99}$$

Accordingly, for $n > -3$, the mass variance is a decreasing function of R, as can be reasonably expected.

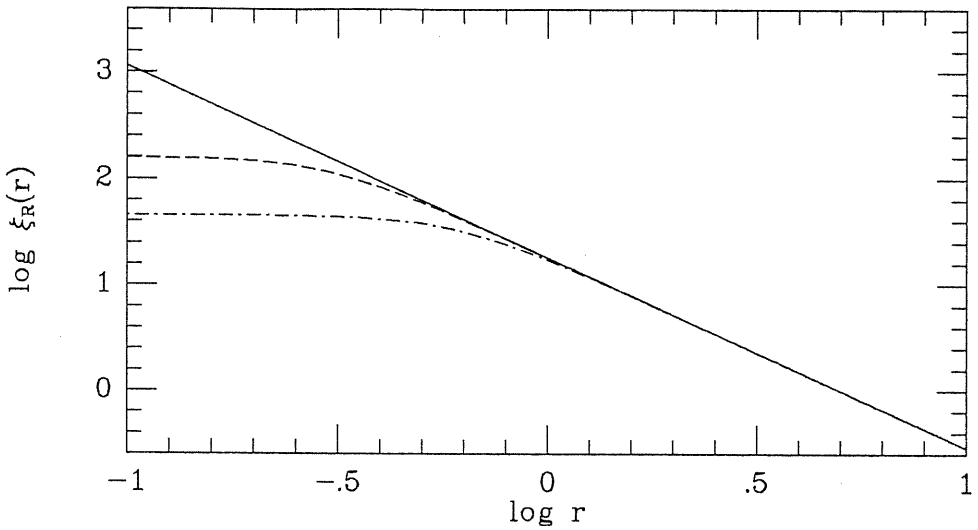

Figure 2.3: *Smoothed 2–point correlation function for two different smoothing radii. The unsmoothed function (solid line) is assumed to have a power law behaviour.*

Following eqs. (2.94) and (2.97), we can explicitly work out the dependence of the mass variance σ_R on the mass scale $< M_R >$, according to

$$\sigma_M^2 \propto < M_R >^{-\alpha} \qquad \alpha = (n+3)/3\,. \tag{2.100}$$

The above result has been obtained with the underlying assumption that different scales R are considered at the same cosmic time. In an alternative way, we can also refer to the epoch at which a fluctuation on a given scale enters the horizon. In this case, the variance on the scale M that is just crossing the horizon, reads

$$\sigma^2_{M(hor)} = \left\langle \left(\frac{\delta M}{M}\right)^2 \right\rangle \propto M^{-\beta} \qquad \beta = (n-1)/3 \tag{2.101}$$

(see, *e.g.*, [27]). In particular, if $n = 1$ according to the canonical predictions of the inflationary paradigm [12], we get $\beta = 0$. In this sense, the Zel'dovich fluctuation spectrum originated by inflation does not present any characteristic scales when these cross the horizon.

Chapter 3

Biased models for galaxy formation

3.1 Motivations for bias

The statistical investigation of the large–scale structure of the Universe represents a powerful test for any theory concerning the formation and evolution of primordial density fluctuations. However, even though such theories are able to predict the statistics of the background matter distribution, the analysis of homogeneous samples of galaxies and galaxy systems are relevant to the statistics of the object distribution. Differences between such two kinds of distribution probably exist and they origin lies in physical mechanisms and environmental effects occurring during the formation of cosmic structures. For this reason, it is of crucial importance to understand which kind of physical processes are relevant to the formation of observed structures and which is their impact in determining a possible segregation between luminous object and background matter distributions.

As we have already seen in Chapter 1, the analysis of homogeneous samples of galaxies leads to the detection of the 2-point galaxy correlation function

$$\xi_g(r) = \left(\frac{r_{o,g}}{r}\right)^{\gamma} \tag{3.1}$$

with $\gamma \simeq 1.8$ and $r_{o,g} \simeq 5\,h^{-1}Mpc$, in the range $0.1 \lesssim r \lesssim 10\,h^{-1}Mpc$ [151]. In a similar way, observational data on the distribution of rich Abell clusters indicates that

$$\xi_c(r) = \left(\frac{r_{o,c}}{r}\right)^{\gamma} \tag{3.2}$$

in the range $5 \lesssim r \lesssim 100\,h^{-1}Mpc$, with the same value of the slope γ, but with a greater clustering length, $r_{o,c} = (3-5)\,r_{o,g}$. Several evidences also exist that the amplitude of cluster correlations does depend on their richness [23,165]. Moreover, clusters shows signals of strong correlations on scales much larger than those relevant

to the galaxy distribution. As a consequence, the large–scale distribution of matter in the Universe can not be traced with the same efficiency both by galaxies and galaxy clusters. On the contrary, such results seem to suggest that neither galaxies nor clusters trace the actual matter distribution. The large correlation amplitude for rich Abell clusters was the main reason that lead Kaiser [112] to introduce the concept of *bias*. According to this model, he postulated that rich Abell clusters arise only from exceptionally high peaks of the background field and, cosequently, exhibit an enhanced clustering with respect the underlying matter.

Further supports in favour of a biased distribution of cosmic structures come from detected correlations between galaxy types and environment (see Section 1.2). Then it would the surprising if galaxy formation were not significantly affected by environmental effects segregating galaxies from the underlying matter. In the following we describe the main motivations for this suggestion and put into evidence the principal cosmological consequences.

3.1.1 Flatness of the Universe

Since the first dynamical investigation of the mass distribution in the Universe, several evidences have been found that the dynamically deduced mass exceeds the luminous matter by a factor ~ 10. Mass is in general estimated by using a relation of the type $M \sim v^2 R$, being v some observed velocity involved in a structure of size R. Accordingly, while a typical value of the mass–to–light ratio for the stellar content of galaxies is of the order $M/L \simeq 10$, data on the virial analysis of groups and clusters of galaxies suggests $M/L \simeq 200$–$500\,h$ [20], so that a value $\Omega_o \sim 0.1$-0.3 for the cosmic density parameter follows. On the other hand, if the matter were all baryonic, $\Omega_o \simeq 0.1$ would be compatible with the Big Bang nucleosyntesis constraints [204]. Thus, although the deduced amount of dark matter exceeds that of luminous matter, it is short by a factor ~ 5 from giving $\Omega_o = 1$, as predicted by canonical inflationary models [99], and leads to the suggestion of a Universe dominated by non–baryonic dark matter.

In order to reconcile the dynamical evidence for $\Omega_o \simeq 0.2$ with the theoretically preferred $\Omega_o = 1$, we are forced to suppose that the rising trend of M/L should continue on scales greater than that of rich clusters ($\sim 10\,h^{-1}Mpc$). The mass estimates on such scales are based on the application of the "cosmic virial theorem" [149,150,151] to pairs of galaxy. Such theorem, that expresses the condition for hydrostatical equilibrium of a self–gravitating system of collisionless particles, gives for the density parameter

$$\Omega_o \propto \xi(r)^{-1}(v/r)^2 \,. \tag{3.3}$$

In such expression, v is the mean pair–velocity and $\xi(r)$ is the 2-point correlation

function. The application of eq. (3.3) together with the observed amplitude of the galaxy 2-point function again seems to suggest that $\Omega_o \simeq 0.1$-0.3 [52]. If, however, galaxies cluster more than the underlying matter, the corresponding 2-point function turns out to be amplified with respect that of the background according to

$$\xi_g(r) = b^2 \xi_\rho(r) . \tag{3.4}$$

Here $\xi_\rho(r)$ represents the background 2-point correlation function, while $b \geq 1$ is the so–called *biasing parameter*. Then, by using ξ_ρ instead of ξ_g in eq. (3.3), the resulting value of Ω_o turns out to be amplified by a factor b^2 and agreement with a flat Universe is achieved for $b = 2$-3.

3.1.2 Evacuation of voids

Observational data on the three–dimensional distribution of galaxies shows that "voids" of size $\sim 50\, h^{-1} Mpc$ in such distribution are quite common. A typical number density of galaxies in these voids is $< 10\%$ of the mean. Assuming that matter is distributed like galaxies, such an underdensity corresponds at recombination to a contrast density $|\delta| \geq 10^{-2}$ if $\Omega_o = 1$ and to $|\delta| \geq 5 \times 10^{-2}$ if $\Omega_o = 0.1$, in contrast with the isotropy of the microwave background on angles $10'$–$1°$ [57].

Also in this case, the situation can be improved by assuming that galaxies are more clustered than matter. In fact, let us take as typical density contrast of galaxies in superclusters and voids the values $\delta_g = 2.5$ and $\delta_g = -0.9$, that are appropriate to the Local Supercluster (LSC) and the Boöte void, respectively. Then, assuming a bias factor $f \sim 3$, that gives $\Omega_o = 1$, the real mass density in the LSC is $\delta \simeq 0.85$, while the mass deficit in the void is $\delta \simeq -0.32$. Such values for the contrast density are compatible with $|\delta| \simeq 9 \times 10^{-4}$ and with $\delta T/T \simeq 3.5 \times 10^{-5} (\Omega_o h^2)^{-1}$, if most of the mass is assumed to be non–baryonic. The above value of the temperature fluctuation is compatible with observational constraints unless $\Omega_o h^2$ is much less than one. Thus, an open Universe with $\Omega_o \simeq 0.2$ is in trouble because it predicts no biasing between matter and galaxy distributions ($f = 1$) and, consequently, too large temperature fluctuations in the Cosmic Microwave Background.

3.1.3 Problems with CDM and HDM models

In a Universe dominated by CDM, the fluctuation spectrum after the equivalence epoch is determined by the assumptions of adiabaticity and scale–invariance of the fluctuations as generated by inflation, and by the cold nature of the DM, which prevents small–scale fluctuations to be damped by free–streaming (see Section 2.4).

Results from N–body simulations of a Universe dominated by CDM led to the conclusion that, if $\Omega_o = 1$, the large scale distribution of galaxies cannot be reproduced, unless the galaxy formation is biased [49]. In such simulation, the resulting 2-point correlation function steepens in time as steeper parts of the initial fluctuation spectrum become non–linear. If mass traces the galaxy distribution, the stage of the simulation to be considered as the present time is reached when its logarithmic slope matches that ($\gamma = 1.8$) observed for galaxies. However, such evolutionary stage corresponds to a value of the clustering length only $\simeq 1\,(\Omega_o h^2)^{-1} Mpc$, too small if compared with $r_{o,g} \simeq 5\,h^{-1} Mpc$ observed for galaxies, unless $\Omega_o h \lesssim 0.2$. Thus, assuming a flat Universe dominated by CDM requires an enhanced clustering of galaxies with respect to the background, such that $\xi_g(r) = (5 - 20)\xi_\rho(r)$ (for $h = 0.5$ and $h = 1$), which is consistent with the values of b deduced above on the ground of general considerations.

In the case of a Universe dominated by hot particles, such as neutrinos with mass $\sim 10\,eV$, free streaming washes out all the small–scale fluctuations. Consequently, the first objects to form are *pancakes* on supergalactic scales, that subsequently fragment to galaxies. The resulting neutrino correlation function rapidly steepens in time during the pancake formation and as sub–clustering develops. Fixing the slope to $\gamma = 1.8$ requires that the first collapse of pancakes must be occurred very recently, at $z \sim 1$ if $\Omega_o = 1$ [44]. In this case, the requirement that the slope of the 2-point function is $\gamma = 1.8$ implies a correlation length for neutrinos $r_o = 8\,h^{-1} Mpc$. Hence, the bias required here is in opposite sense because the resulting galaxies must be less clustered than the DM background (antibiasing).

All the above considerations argue for some kind of segregation between galaxies and background matter. On the other hand, such bias can be the natural consequence of physical processes occurring during the formation of cosmic structures and will be discussed in details in the next section. Another kind of bias, that has observational origin, is related to the fact that galaxy or cluster sample are magnitude limited (optical bias; see ref. [26]). As a consequence, objects in such samples are identified with peaks of the luminosity field, that have height greater than a fixed threshold.

3.2 Physical mechanisms for bias

In this section we describe some cosmological scenarios in which a biasing in the distribution of cosmic structure arises (see also refs. [54,57] as reviews on biased galaxy formation). The bias mechanisms we will describe in the following can be classified in two general types.

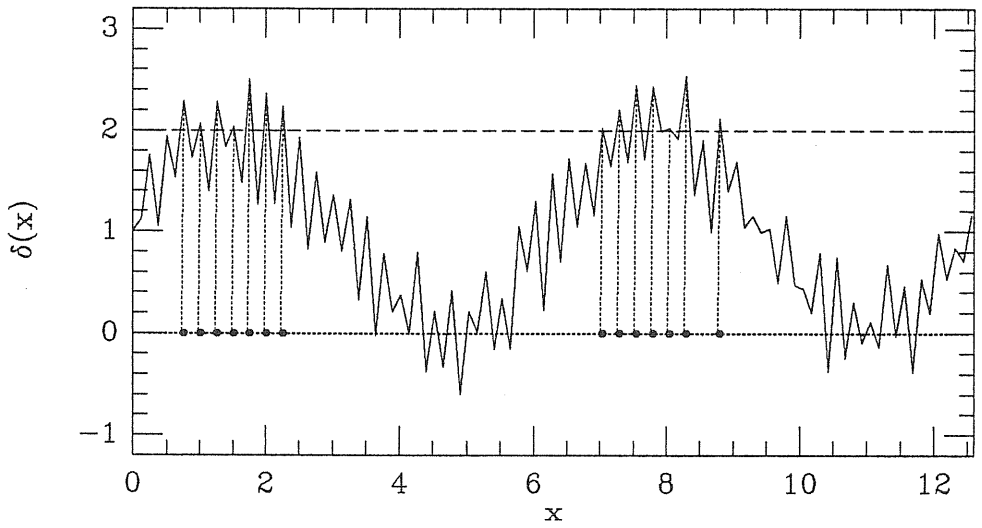

Figure 3.1: *Enhancement of the clustering of peaks higher than a fixed threshold with respect to the background peaks for a one–dimensional fluctuation field.*

i) The Universe is dominated by one kind of DM, while the baryonic component is segregated from non–baryonic DM even on scales $\sim 30\,h^{-1}Mpc$. This can provide supply for galaxy formation only in certain regions.

ii) Large–scale baryon distribution does trace the DM on scales $> 1\,h^{-1}Mpc$, but the efficiency with which baryons turns into luminous galaxies depends to other environmental effects, such as local background density or it may be the result of feedback from other galaxies. The effect may be destructive, suppressing galaxy formation, or constructive, enhancing galaxy formation in the neighborhood of other galaxies (*e.g.*, explosions).

3.2.1 Bias in hierarchical clustering

An enhanced clustering of galaxies over the background matter can arise in a *bottom–up* scenario, if galaxies formed only from those peaks of the density distribution, smoothed on the galactic scale R, that have amplitude at least ν times the *r.m.s.* value $\sigma_{\rm R}$. It was shown by Kaiser [112] that, if the power spectrum has sufficient amplitude in correspondence of small wavenumbers, high peaks occur with greater probability in the crests rather than in the troughs of a large scale fluctuation mode, so they display an enhanced clustering (see Figure 3.1). In particular, correlation functions arising from N–body simulation in a CDM–dominated Universe reproduce the observed ones if galaxies are identified with peaks at $\nu \sim 2.5$.

In this picture, the crucial point is however to understand what physical mech-

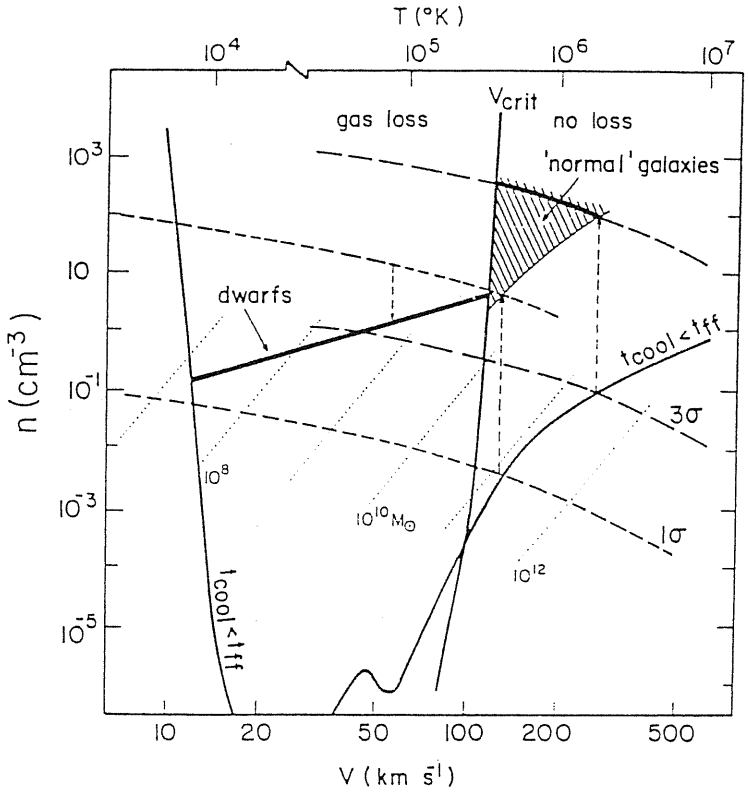

Figure 3.2: *Gas number density* vs. *virial velocity; the formation of dwarfs* vs. *"normal" galaxies in CDM halos, and the origin of biased galaxy formation (after [57]).*

anisms can provide a sharp cutoff in the efficiency of galaxy formation for density fluctuations $\delta_R < \nu\sigma_R$.

A possible mechanism is represented by the so–called *natural bias*. In order to describe such scenario, let us observe that for a galaxy to be visible at the present time, we must ask that the baryonic matter has been able to dissipate and turn into stars. In order for dissipation to occur, the redshift of collapse clearly needs to be sufficiently large that there is time for an object to cool between its formation at redshift z_{cool}, when the density fluctuation attains the critical value $\delta = \delta_c$ (it is $\delta_c \simeq 1.69$ in the linear model for spherical collapse) and the present epoch. More massive objects take longer to cool. Then, the requirement for a fluctuation on a given mass–scale M to have enough time from t_{cool} (corresponding to z_{cool}) to cool down can be traduced in the existence of a mass–dependent threshold $\nu(M)\sigma_M = \delta_c[1 + z_{cool}(M)]$.

Such situation is described in the *density–temperature* plot of Figure 3.2. The cooling curve, above which $t_{cool} < t_{dyn}$ (here $t_{dyn} \sim 1/\sqrt{G\rho}$ is the gravitational free–fall time), confines the region where the gas can contract and form stars [171,20]. The cooling curve is calculated for a primordial gas composition and under the assumption that the mean baryonic gas density is 10% of the total mass density. Each of the

dotted diagonal lines indicates in the $n-T$ diagram the positions of all the structures having the same Jeans mass $M_J \simeq 100\,T^{3/2}n^{-1/2}M_\odot$. The almost vertical line V_{crit}, which has been introduced by Dekel & Silk [58], divides the permissible region for galaxy formation in two; a protogalaxy characterized by a virial velocity $> V_{crit}$ cannot expel a large fraction of its original gas content and form a normal galaxy. A protogalaxy with $V < V_{crit}$ can produce a supernova–driven wind, which would drive a substantial fraction of the protogalactic gas out, leaving behind a diffuse dwarf. The dashed curves labeled by $\nu\sigma$ ($\nu = 1, 3$) refer to fluctuations with $\delta M/M$ equal to ν times the *r.m.s.* value, for a CDM spectrum. The corresponding parallel dashed curves refer to the protogalactic gas clouds, after a contraction of a factor 10 inside isothermal halos, to densities that are comparable to the halo densities such that star formation is possible. The two vertical arrows indicate the largest galaxies that can form out of a 1σ and a 3σ peaks, respectively. Let us observe that the most part of galaxies arising from 1σ peaks have $V < V_{crit}$, so that they would turn into dwarf galaxies. Instead, the shaded area represents the locus were normal galaxies are expected to be found. It is also evident that most of them are originated from 2σ and 3σ peaks. According to such predictions, normal galaxies, arising from exceptionally high peaks are expected to be much more correlated than the background fluctuations and lie preferentially in rich clusters. Viceversa, dwarf galaxies form from typical (*i.e.*, 1σ) peaks, consequently they are expected to be better tracers of the matter distribution.

Even though the *natural bias* prescription leads to the prediction of a *mass–dependent* critical threshold above which galaxies form, it is not clear if this effect can produce a cutoff sharp enough at $\nu\sigma_{\rm R}$. In this chapter we will investigate the effect of taking a cutoff in the fluctuation field different from the sharp one. This would be expected if one takes into account more complicated physical effects occurring during the processes of galaxy formation.

3.2.2 Bias in a top–down scenario

A bias is generated automatically in any top–down scenario, where the fluctuations on scales $\lesssim 30\,h^{-1}Mpc$ are erased by free streaming, as in a neutrino dominated Universe. As a consequence of the resulting large–scale coherence length, there are motion from proto–voids to proto–pancakes. Collapse into flat pancakes is accompanied by streaming toward their line of intersection (filaments) and toward the knots where rich clusters form. The gas then contracts dissipatively into high–density regions within which it cools. Galaxies are thus expected to be limited to very specific regions.

However, as we have seen in the previous section, the resulting clustering

length for neutrinos at the present time is larger than that observed for galaxies. Consequently one is forced to require an *antibiasing*, so to suppress galaxy formation in high–density regions or to enhance their formation in low–density regions.

3.2.3 Bias in the explosion scenario

Differently from the gravitational instability picture, in the explosion scenario positive energy perturbations of non–gravitational origin drive material away from the *seeds* of the explosions, sweeping primordial gas into dense, expanding shells that cool and fragment into galaxies [145,109]. The explosion scenario naturally accounts for the "bubbly" appearance of galaxy distribution, as revealed by the CfA redshift survey (see §1.1). Since shells enclose an appreciable amount of space, their dynamical interaction play an important role in the formation of clusters, superclusters and voids. Results from N–body simulations to study clustering in a universe formed by interacting shells [177] indicate that the explosion scenario may be able to reproduce the observed galaxy correlation function, in addition to producing large voids and bias. By identifying rich clusters of galaxies as the knots where three shells intersects, it is possible to reproduce several statistical feature of the superclustering, like the amplitude of the correlation function for rich–cluster and their richness distribution [203].

A variety of physical mechanisms might generate such perturbations. Explosions of supermassive stars [42] or supernovae from the earliest galaxies could acts as seeds [145]. However, it is at present not clear whether or not such energy sources can be sufficient to create the large voids that are observed. Holes on scales of some tens of megaparsecs would require a fantastic amount of supernovae exploding coherently. Moreover, initial conditions are needed for generating primordial galaxies that act as seeds of the explosions.

From all the above considerations about possible mechanisms for a biased galaxy formation, it looks quite obvious that the simple sharp cutoff applied to the density fluctuation field can hardly account for highly non–linear phenomena occurring during the formation of structures. For this reason it is necessary to understand the way in which different bias mechanisms affect the shape of the cut–off and check the effect of more general biased model on the statistics of the resulting object distribution.

3.3 The statistics of the biased density field

In this section we introduce the concept of *biased field* to model the observed object distributions of galaxies and galaxy clusters as suitable functionals of the background fluctuation field. In particular, we deduce the expression of the N-point joint probability for the *biased field*, and relate it to the statistical properties of the background fluctuations.

3.3.1 The concept of biased density field

In order to describe the distribution of objects, let us define the *biased* density field

$$\rho_{\nu,\mathrm{R}} = f[\delta_{\mathrm{R}}(x) - \nu\sigma_{\mathrm{R}}] \tag{3.5}$$

as a generic functional of the background matter field. In eq. (3.5), $\delta_{\mathrm{R}}(x)$ represents the density fluctuation field, smoothed on the scale R (see §2.6). The *threshold function* $f(\alpha)$ turns out to depend, other than on the smoothing radius R, also on the biasing level ν, that is related to the height of the fluctuations of the background field that correspond to observable objects. In this way, we identify different classes of objects, such as galaxies, groups and clusters, by means of different choices of ν, R, and also of $f(\alpha)$.

In eq. (3.5), the shape of the threshold function does depend on the physical meaning that we give them. A possible choice is that of considering the class of $\rho_{\nu,\mathrm{R}}(x)$ with values between 0 and 1, so that eq. (3.5) can be interpreted as the probability that a fluctuation with amplitude $\delta_{\mathrm{R}}(x)$ give rise to an observable object. In this case, the simplest example of biased field is the so–called θ–threshold,

$$\rho_{\nu,\mathrm{R}} = \theta[\delta_{\mathrm{R}}(x) - \nu\sigma_{\mathrm{R}}]\,, \tag{3.6}$$

that selects only those fluctuations with amplitude $\delta_{\mathrm{R}}(x) \geq \nu\sigma_{\mathrm{R}}$, while give zero probability to have observable structures in correspondence of fluctuations with amplitude below the critical value $\nu\sigma_{\mathrm{R}}$.

The case of the θ–threshold is the original biased model, that was introduced for the first time by Kaiser [112] for explaining the large correlation length of rich Abell clusters. He assumed that galaxy clusters arise from exceptionally high peaks of the density fluctuation field, that was assumed to have Gaussian distribution. Several other authors extended this idea to n-point correlation function [164,110], identifying objects either with the maxima of the density field [147,11] or with regions with density exceeding a limiting value [190]. Generalization to non–Gaussian background was also considered in the literature, either analitically [134,95,47], or *via* N–body simulations [136].

In the following of this chapter, we will describe a general analytical method for investigating the statistical properties of non–θ thresholds, with non–Gaussian background. In particular, we evaluate the N-point joint probability, $\Pi^{(N)}_{\nu,\mathrm{R}}(x_1,...,x_\mathrm{N})$, for a generic biased field (3.5) and, consequently, the expressions for the *disconnected* N-point correlation functions

$$\xi^{(N)}_{disc,\nu,\mathrm{R}}(x_1,...,x_\mathrm{N}) \;=\; \frac{\Pi^{(N)}_{\nu,\mathrm{R}}(x_1,...,x_\mathrm{N})}{[\Pi^{(1)}_{\nu,\mathrm{R}}]^N} - 1\,. \tag{3.7}$$

We note that in a paper by Szalay [189], an expression has been deduced for the 3-point function for a generic threshold, but still in the case of Gaussian background. In any case, such results are obtained under some approximations that severely restrict their applicability.

3.3.2 The N-point joint probability

Let us consider the expression of the N-point joint probability

$$\Pi^{(N)}_{\nu,\mathrm{R}}(x_1,...,x_\mathrm{N}) \;\equiv\; <\rho_{\nu,\mathrm{R}}(x_1)...\rho_{\nu,\mathrm{R}}(x_\mathrm{N})> \;=\; \int D[\delta(x)]\,P[\delta(x)]\,\prod_{r=1}^{N}\rho_{\nu,\mathrm{R}}(x_r) \tag{3.8}$$

that the biased field (3.5) takes the values $\rho_{\nu,\mathrm{R}}(x_1),...,\rho_{\nu,\mathrm{R}}(x_\mathrm{N})$ at the points $x_1,...,x_\mathrm{N}$, respectively. Here $P[\delta(x)]$ represents the probability distribution in the functional space of the configurations $\delta(x)$ for the fluctuation field (see §2.3).

Assuming non–Gaussian probability distribution and general shape for the *threshold function*, after a series of non trivial calculation (see Appendix A.1), we get

$$\begin{aligned}&\Pi^{(N)}_{\nu,\mathrm{R}}(x_1,...,x_\mathrm{N}) \;=\\ &=\; \sigma_\mathrm{R}^{-lN}\,e^{Nh(0)}\sum_{L=0}^{\infty}\sum_{[m_L]}\Big[\prod_{n=1}^{L}\prod_{[r_n]=1}^{N}\Big(\frac{W^{(n)}_{\mathrm{R},[r_n]}}{n!}\Big)^{m_{n,[r_n]}}\frac{1}{m_{n,[r_n]}!}\Big]\prod_{r=1}^{N}a^{(l)}_{\mathbf{m}(r)}(2^{-1/2}\nu)\,,\end{aligned} \tag{3.9}$$

where

$$W^{(n)}_{\mathrm{R},[r_n]} \;=\; \frac{h^{(n)}(0)}{(i\sigma_\mathrm{R})^n}\prod_{k=1}^{n-1}\delta_{r_k,r_{k+1}} + w^{(n)}_{\mathrm{R},[r_n]}\,. \tag{3.10}$$

The dependence on the shape of the threshold function is expressed through the derivatives of $h(\phi)$ and the integer l, both defined according to

$$(i\phi)^l\,e^{h(\phi)} \;=\; \frac{1}{\sqrt{2\pi}}\int_{-\infty}^{+\infty}d\alpha\,f'(\alpha)\,e^{i\alpha\phi} \tag{3.11}$$

(l is the order of a possible zero of the Fourier transform of $f'(\alpha)$ in the origin). Instead, the statistics of the background is taken into account by means of the quantities

$$\begin{aligned} w_{\mathrm{R},[r_n]} &= \frac{\xi^{(n)}_{con,\mathrm{R}}(x_{r_1},...,x_{r_n})}{\sigma^n_{\mathrm{R}}} \quad if \quad n>2 \\ w_{\mathrm{R},[r_n]} &= \frac{\xi^{(2)}_{\mathrm{R}}(x_{r_1},x_{r_2})}{\sigma^2_{\mathrm{R}}} \quad if \quad x_{r_1}\neq x_{r_2} \\ w_{\mathrm{R},[r_n]} &= 0 \quad if \quad x_{r_1}=x_{r_2}\,. \end{aligned} \tag{3.12}$$

Here $\xi^{(n)}_{con,\mathrm{R}}(x_{r_1},...,x_{r_n})$ represents the background n–point *connected* correlation function, smoothed on the scale R. The set of non–negative integers $m_{n,[r_n]}=m_{n,r_1,...,r_n}$ appearing in eq. (3.9) are related to the summation indices m_n by means of $\sum^N_{[r_n]} m_{n,[r_n]} = m_n$, while $\sum^L_{n=1} nm_n = L$.

Furthermore

$$\begin{aligned} a^{(l)}_m(z) &= 2^{-\frac{m+l-1}{2}} e^{-z^2} H_{m+l-1}(z) \qquad (m+l>1) \\ a^{(0)}_0(z) &= \sqrt{\frac{\pi}{2}}\, erfc(z)\,, \end{aligned} \tag{3.13}$$

where $H_n(z)$ are the Hermite polynomials and $erfc(z)$ the complementary error function. To notice also that the integers

$$\mathrm{m}(r) = \sum_{n=1}^{L}\sum_{[r_n:r_1]=1}^{N} (m_{n,r_1,r_2,...,r_n} + m_{n,r_2,r_1,...,r_n} + ... + m_{n,r_n,r_2,...,r_1}) \tag{3.14}$$

($[r_n : r_j] = r_1,...,r_{j-1},r_{j+1},...,r_n$; the role of r_1 can be played by any r_j) are different from m_r and must satisfy the constraint $\sum^N_{r=1}\mathrm{m}(r) = L$.

For $N=1$, eq. (3.9) gives the mean value of the field $\rho_{\nu,\mathrm{R}}$

$$\Pi^{(1)}_{\nu,\mathrm{R}} \equiv <\rho_{\nu,\mathrm{R}}> = \sigma^{-l}_{\mathrm{R}} e^{h(0)} \sum_{L=0}^{\infty}\sum_{[m_L]}\left[\prod_{n=1}^{L}\left(\frac{W^{(n)}_{\mathrm{R}}}{n!}\right)^{m_n}\frac{1}{m_n!}\right] a^{(l)}_L(2^{-1/2}\nu)\,. \tag{3.15}$$

Here we introduced the *pseudo–cumulants*

$$W^{(n)}_{\mathrm{R}} = \frac{h^{(n)}(0)}{(i\sigma_{\mathrm{R}})^n} + w^{(n)}_{\mathrm{R}}, \tag{3.16}$$

where the *cumulants* $w^{(n)}_{\mathrm{R}} = w^{(n)}_{\mathrm{R}}(x,...,x)$ vanish for Gaussian distribution, according to the definition (3.12).

If the threshold function $f(\alpha)$ represents the probability for a fluctuation to be selected, then $\Pi^{(1)}_{\nu,\mathrm{R}}$ can be interpreted as the fraction of volume occupied by objects. Consequently, eq. (3.15) expresses the dependence of the number density of galaxies or galaxy clusters on the shape of the threshold function.

3.4 Correlation functions of the biased field

According to eqs. (3.9) and (3.15), that describes the statistics of the biased field, we use the definition (3.7) to express the correlation function of the object distribution in terms of those of the background distribution.

To this purpose, let us write eq. (3.9) as

$$\Pi^{(N)}_{\nu,\mathrm{R}}(x_1,...,x_\mathrm{N}) = \sigma_\mathrm{R}^{-lN} e^{Nh(0)} \sum_{L=0}^{\infty} \sum_{[m_L]} \left[\prod_{n=1}^{L} \prod_{[r_n]=1}^{N} \left(\frac{W^{(n)}_{\mathrm{R},[r_n]}}{n!} \right)^{m_{n,[r_n]}} \frac{\nu^{nm_{n,[r_n]}}}{m_{n,[r_n]}!} \right] \times$$
$$\times \nu^{N(l-1)} e^{-\frac{N\nu^2}{2}} [1 + O^{(N)}_\mathrm{L}(\nu^{-2})] . \qquad (3.17)$$

Here, the constant $O^{(N)}_\mathrm{L}(\nu^{-2})$ contains all the terms of order ≥ 2 in ν^{-1}, coming from the productories of Hermite polynomials. After summing at the zero-th order in ν^{-1} the series appearing in eq. (3.17), we obtain

$$\Pi^{(N)}_{\nu,\mathrm{R}}(x_1,...,x_\mathrm{N}) = \sigma_\mathrm{R}^{-lN} \nu^{N(l-1)} e^{-\frac{N\nu^2}{2}} e^{Nh(0)} \times$$
$$\times \left\{ exp\left[\sum_{n=1}^{\infty} \nu^n \sum_{[r_n]=1}^{N} \left(\frac{W^{(n)}_{\mathrm{R},[r_n]}}{n!} \right) \right] + O^{(N)}(x_1,...,x_\mathrm{N}) \right\} . \qquad (3.18)$$

Here, all the terms of higher order in ν^{-1} are factorized into the quantity

$$O^{(N)}(x_1,...,x_\mathrm{N}) = \sum_{L=0}^{\infty} \sum_{[m_L]} \left[\prod_{n=1}^{L} \prod_{[r_n]=1}^{N} \left(\frac{\nu^n W^{(n)}_{\mathrm{R},[r_n]}}{n!} \right)^{m_{n,[r_n]}} \frac{1}{m_{n,[r_n]}!} \right] O^{(N)}_\mathrm{L}(\nu^{-2}) . \qquad (3.19)$$

Similarly, in the case $N = 1$,

$$\Pi^{(1)}_{\nu,\mathrm{R}} = \sigma_\mathrm{R}^{-l} \nu^{l-1} e^{-\frac{\nu^2}{2}} e^{h(0)} \left\{ exp\left[\sum_{n=2}^{\infty} \nu^n \frac{W^{(n)}_\mathrm{R}}{n!} \right] + O^{(1)} \right\} , \qquad (3.20)$$

where

$$O^{(1)} = \sum_{L=0}^{\infty} \sum_{[m_L]} \left[\prod_{n=1}^{L} \left(\frac{\nu\, W^{(n)}_{\mathrm{R},[r_n]}}{n!} \right)^{m_n} \frac{1}{m_n!} \right] O^{(1)}_\mathrm{L}(\nu^{-2}) \qquad (3.21)$$

and with obvious meaning of $O^{(1)}_\mathrm{L}(\nu^{-2})$.

As already remarked, in deducing eqs. (3.18) and (3.20) we summed the series over the index L only to the zero-th order in ν^{-1}. In fact, due to the dependence on L of the terms of higher order in ν^{-1}, it is impossible to factorize terms of the type ν^{-2n}, in such a way to obtain only quantities coming from the Cauchy products between series expansions on exponential functions. In any case, the evident complexity of eqs. (3.18) and (3.20) is the price to be payed for their full generality (*i.e.*, general

shapes for background distribution and threshold function). In the Gaussian case too, when $w^{(n)}_{\mathrm{R},[r_n]} = 0$ for $n > 2$, we do not have much simplification. However, as we will see in the next chapter, the expression of $\Pi^{(N)}_{\nu,\mathrm{R}}$ becomes more handleable for particular choices of the biased field $\rho_{\nu,\mathrm{R}}$.

3.4.1 The two- and three-point functions

We will now deduce the 3-point correlation function of the biased field and express it in terms of the 2-point function. This is interesting because, as already seen in Chapter 1, observational data on the clustering of galaxies and clusters allows one to deduce the 3-point function as a suitable combination of the 2-point ones. In this way it is possible to check whether or not the hierarchical expression (2.23) or the Kirkwood superposition (2.22) can be predicted by our general biased model.

According to the definition (3.7), the 2-point function can be expressed according to

$$\begin{aligned}\xi^{(2)}_{dis,\nu,\mathrm{R}}(x_1,x_2) &= \frac{\Pi^{(2)}_{\nu,\mathrm{R}}(x_1,x_2)}{[\Pi^{(1)}_{\nu,\mathrm{R}}]^2} - 1 = \\ &= -1 + C^{(2)}(x_1,x_2) + S^{-2} exp\Big[\sum_{n=1}^{\infty}\nu^n \sum_{[r_n]=1}^{2}\frac{W^{(n)}_{\mathrm{R},[r_n]}}{n!}\Big]. \qquad (3.22)\end{aligned}$$

Here we introduced the constant

$$S = \sigma^l_{\mathrm{R}}\nu^{1-l}e^{\frac{\nu^2}{2}}\Pi^{(1)}_{\nu,\mathrm{R}} \qquad (3.23)$$

as well as the function

$$C^{(N)}(x_1,...,x_{\mathrm{N}}) = S^{-N}e^{Nh(0)}O^{(N)}(x_1,...,x_{\mathrm{N}}) \qquad (3.24)$$

evaluated for $N = 2$.

Moreover, for the 3-point function we get

$$\xi^{(3)}_{dis,\nu,\mathrm{R}}(x_1,x_2,x_3) = \frac{\Pi^{(3)}_{\nu,\mathrm{R}}(x_1,x_2,x_3)}{[\Pi^{(1)}_{\nu,\mathrm{R}}]^3} - 1\,. \qquad (3.25)$$

According to eq. (3.18), the 3-point joint probability, that appears in the above expression, takes the form

$$\begin{aligned}&\Pi^{(3)}_{\nu,\mathrm{R}}(x_1,x_2,x_3) = \\ &= \sigma^{-3l}_{\mathrm{R}}\nu^{3(l-1)}e^{-\frac{3\nu^2}{2}}e^{3h(0)}\Big\{exp\Big[\sum_{n=2}^{\infty}\frac{\nu^n}{n!}\Big(\sum_{[r_n]=1,2}+\sum_{[r_n]=2,3}+\sum_{[r_n]=1,3}\Big)W^{(n)}_{\mathrm{R},[r_n]} - 3W^{(n)}_{\mathrm{R}}\Big]\times \\ &\times\ exp\Big[\sum_{n=3}^{\infty}\nu^n\Big(\sum_{j=1}^{n-2}\sum_{k=1}^{n-j-1}w^{(n)}_{\mathrm{R},[j,k,n-j-k]}\Big)\frac{1}{j!k!(n-j-k)!}\Big] + O^{(3)}(x_1,x_2,x_3)\Big\}. \qquad (3.26)\end{aligned}$$

In the above relation, we introduced the quantities

$$w^{(n)}_{\mathrm{R},[j,k,n-j-k]} = \frac{1}{\sigma^n_{\mathrm{R}}} \int \Big(\prod_{a=1}^{j} dy_a\, Q_{\mathrm{R}}(|x_1 - y_a|)\Big)\Big(\prod_{b=1}^{k} dy_b\, Q_{\mathrm{R}}(|x_2 - y_b|)\Big) \times$$
$$\times \Big(\prod_{c=1}^{n-j-k} dy_c\, Q_{\mathrm{R}}(|x_3 - y_c|)\Big)\xi^{(n)}_{con,\mathrm{R}}(y_1, ..., y_n)\,. \qquad (3.27)$$

Then, after substituting eq. (3.26) in eq. (3.25), taking into account the expression (3.22) for the 2-point function and rearranging the sums over the indices $[r_n]$, we finally obtain

$$\xi^{(3)}_{dis,\nu,\mathrm{R}}(x_1, x_2, x_3) = -1 + C^{(3)}(x_1, x_2, x_3) + \frac{B^{(3)}(x_1, x_2, x_3)}{[B^{(2)}]^3} \times$$
$$\times \{[-1 + C^{(2)}(x_1, x_2) + \xi^{(2)}_{\nu,\mathrm{R}}(x_1, x_2)] \times ...3 \;\; terms\}\,. \qquad (3.28)$$

This represents a sort of generalization of the Kirkwood superposition (2.22). The above expression of the 3-point function contains the functions

$$B^{(N)}(x_1, ..., x_{\mathrm{N}}) = S^{-N} G^{(N)}(x_1, ..., x_{\mathrm{N}}) exp\Big\{\Big[N - \binom{N}{2}\Big]\sum_{n=1}^{\infty}\frac{\nu^n}{n!}W^{(N)}_{\mathrm{R}}\Big\}\,, \qquad (3.29)$$

where, in turn, the quantity $G^{(N)}$ appears, to be evaluated for $N = 3$:

$$G^{(3)}(x_1, x_2, x_3) = exp\Big[\sum_{n=3}^{\infty}\nu^n\Big(\sum_{j=1}^{n-2}\sum_{k=1}^{n-j-1} w^{(n)}_{r,[j,k,n-j-k]}\Big)\frac{1}{j!\,k!\,(n-j-k)!}\Big] \qquad (3.30)$$

It is easy to show that, in the case $N = 2$, $G^{(2)}(x_1, x_2) = 1$, so that $B^{(2)} = const.$

3.4.2 The N-point functions

The generalization of the above calculations to higher correlation orders enable us to work out the expression of the N-point correlation functions in terms of the 2-point function. Indeed, according to eq. (3.18) we express the N-point joint probability as

$$\Pi^{(N)}_{\nu,\mathrm{R}}(x_1, ..., x_{\mathrm{N}}) =$$
$$= \sigma_{\mathrm{R}}^{-Nl}\nu^{N(l-1)}e^{-\frac{N\nu^2}{2}}e^{Nh(0)}\Big\{exp\Big[\sum_{n=2}^{\infty}\frac{\nu^n}{n!}\Big(\sum_{[r_n]=1,2} + ...\binom{N}{2}\;\; terms\Big)W^{(n)}_{\mathrm{R},[r_n]} +$$
$$- \binom{N}{2}W^{(n)}_{\mathrm{R}} + \Big(\sum_{[r_n]=1}^{N-1} + ...N\;\; terms\Big)W^{(n)}_{\mathrm{R},[r_n]} - NW^{(n)}_{\mathrm{R}}\Big]F^{(N)}(x_1, ..., x_{\mathrm{N}}) +$$
$$+ O^{(N)}(x_1, ..., x_{\mathrm{N}})\Big\}\,, \qquad (3.31)$$

that is completely analogous to eq. (3.26). Here, the functions

$$F^{(N)}(x_1,...,x_{\rm N}) \;=\; exp\Big\{\sum_{n=N}^{\infty}\nu^n\sum_{[j_i]}\frac{w^{(n)}_{{\rm R},[j_i]}}{\prod_{i=1}^{N}j_i!}\Big\} \tag{3.32}$$

contain sums over the non–negative indices $[j_i]=j_1,...,j_{\rm N}$, that satisfy the condition $\sum_{i=1}^{N}j_i=n$. Moreover, in eq. (3.32) it appear the functions $w^{(n)}_{{\rm R},[r_n]}$, that, in analogy with the quantities (3.27), can be written as

$$w^{(n)}_{{\rm R},[j_i]} \;=\; \frac{1}{\sigma^n_{\rm R}}\int\prod_{i=1}^{N}\Big(\prod_{a_i=1}^{j_i}dy_{a_i}\,Q_{\rm R}(|x_i-y_{a_i}|)\Big)\xi^{(n)}_{con,{\rm R}}(y_1,...,y_n)\,. \tag{3.33}$$

Taking into account the deduced expression for $\xi^{(2)}_{\nu,{\rm R}}$, we can finally express the N-point function for the biased field in terms of the 2-point function according to

$$\begin{aligned}\xi^{(N)}_{\nu,{\rm R}}(x_1,...,x_{\rm N}) \;&=\; -1+C^{(N)}(x_1,...,x_{\rm N})+\frac{B^{(N)}(x_1,...,x_N)}{[B^{(2)}]^{\binom{N}{2}}}\times\\ &\times\;\;[-1+C^{(2)}(x_1,x_2)+\xi^{(2)}_{\nu,{\rm R}}(x_1,x_2)]\times...\binom{N}{2}\;\;terms\end{aligned} \tag{3.34}$$

In the expression (3.29) for $B^{(N)}$ it appears the function $G^{(N)}$ that is the generalization of the quantity $G^{(3)}$ and that can be written as

$$\begin{aligned}G^{(N)}(x_1,...,x_{\rm N}) \;&=\; \Big[G^{(3)}(x_1,x_2,x_3)\times...\binom{N}{2}\;\;terms\Big]\times...\\ ...\times&\Big[G^{(N-1)}(x_1,...,x_{\rm N-1})\times...N\;\;terms\Big]\,F^{(N)}(x_1,...,x_{\rm N})\,.\end{aligned} \tag{3.35}$$

By comparing eqs. (3.34) and (2.22), it is easy to see that the N-point correlation function for the biased field takes a form that looks like a generalization of the Kirkwood superposition.

Let us finally observe that our general procedure for investigating the statistical properties of a generic biased field, in the presence of a non–Gaussian background, allows us to deduce rather complex expressions for the correlation function. However, as we will see in the next section, there exist some physically relevant cases in which the above relations for $\xi^{(N)}_{\nu,{\rm R}}$ can be written in a much more simple way.

3.5 The high–threshold approximation

According to the original idea of bias proposed by Kaiser [112], an enhancement of the clustering of galaxies and galaxy clusters with respect to the background matter

naturally follows from the assumption that observable cosmic structures arise from exceptionally high peaks of the density field, smoothed over a suitable scale R.

From an analytical point of view, assuming that $f[\delta_{\rm R}(x)-\nu\sigma_{\rm R}]$ acts only on the very high maxima of the background is equivalent to taking $\nu \gg 1$ in the argument of the threshold function. In this *high-threshold* approximation, the expression (3.13) for the coefficients $a^{(l)}_{\mathbf{m}}(z)$, that appears in the N-point joint probability, modifies into

$$a^{(l)}_{\mathbf{m}}(z) \simeq (2^{1/2}z)^{m+l-1}e^{-z^2}\,. \tag{3.36}$$

Here we used the asymptotic expression for the Hermite polynomials, $H_n(z) \simeq (2z)^n$. As a consequence of the high-ν limit, all the terms of order ≥ 2 appearing in eq. (3.18) vanish, so that $O^{(N)}(x_1,...,x_{\rm N}) = 0$, $C^{(N)}(x_1,...,x_{\rm N}) = 0$ and the joint probability takes the much simpler form

$$\Pi^{(N)}_{\nu,{\rm R}}(x_1,...,x_{\rm N}) = \sigma_{\rm R}^{-lN}\nu^{N(l-1)}e^{-\frac{N\nu^2}{2}}e^{Nh(0)}exp\Big\{\sum_{n=1}^{\infty}\frac{\nu^n}{n!}\sum_{[r_n]=1}^{N}W^{(n)}_{{\rm R},[r_n]}\Big\}\,. \tag{3.37}$$

Taking into account the definition (3.10) for the functions $W^{(n)}_{{\rm R},[r_n]}$, we get

$$\begin{aligned}
&\Pi^{(N)}_{\nu,{\rm R}}(x_1,...,x_{\rm N}) = \\
&= \sigma_{\rm R}^{-lN}\nu^{N(l-1)}e^{-\frac{N\nu^2}{2}}e^{Nh(0)}exp\Big\{\sum_{n=1}^{\infty}\frac{\nu^n}{n!}\sum_{[r_n]=1}^{N}\Big[w^{(n)}_{{\rm R},[r_n]}+\frac{h^{(n)}(0)}{(i\sigma_{\rm R})^n}\prod_{k=1}^{n-1}\delta_{r_k,r_{k-1}}\Big]\Big\} = \\
&= \sigma_{\rm R}^{-lN}\nu^{N(l-1)}e^{-\frac{N\nu^2}{2}}exp\Big\{\sum_{n=0}^{\infty}\frac{\nu^n}{n!}\Big[N\frac{h^{(n)}(0)}{(i\sigma_{\rm R})^n}+\sum_{[r_n]=1}^{N}w^{(n)}_{{\rm R},[r_n]}\Big]\Big\} = \\
&= \sigma_{\rm R}^{-lN}\nu^{N(l-1)}e^{-\frac{N\nu^2}{2}}e^{Nh(\frac{\nu}{i\sigma_{\rm R}})}exp\Big\{\sum_{n=2}^{\infty}\frac{\nu^n}{n!}\sum_{[r_n]=1}^{N}w^{(n)}_{{\rm R},[r_n]}\Big\}\,.
\end{aligned} \tag{3.38}$$

In the case $N = 1$, the fraction of volume occupied by objects in the high-threshold limit is

$$\Pi^{(1)}_{\nu,{\rm R}} = \sigma_{\rm R}^{-l}\nu^{l-1}e^{-\frac{\nu^2}{2}}e^{h(\frac{\nu}{i\sigma_{\rm R}})}exp\Big\{\sum_{n=3}^{\infty}\frac{\nu^n}{n!}w^{(n)}_{\rm R}\Big\} \tag{3.39}$$

Let us observe that the above expressions for the joint probabilities coincides with those obtained by Kaiser [112], once we assume Gaussianety for the background distribution.

Particularly interesting are the expressions for the 2-point correlation functions

$$\xi^{(2)}_{\nu,{\rm R}}(x_1,x_2) = -1+exp\Big\{\sum_{n=2}^{\infty}\frac{\nu^n}{n!}\Big[\sum_{[r_n]=1}^{2}w^{(n)}_{{\rm R},[r_n]}-2w^{(n)}_{\rm R}\Big]\Big\} \tag{3.40}$$

and for the disconnected 3-point function

$$\xi^{(3)}_{\nu,{\rm R}}(x_1,x_2,x_3) = -1+G^{(3)}(x_1,x_2,x_3)[1+\xi^{(2)}_{\nu,{\rm R}}(x_1,x_2)]\times ...3\ \ terms\,. \tag{3.41}$$

As it is easy to show, the relevant properties of the correlation functions evaluated in the high–ν regime are that any dependence on the shape of the threshold function different from the sharp one has completely disappeared. This interesting feature is essentially due to the fact that, in the limit $\nu \gg 1$, the details of the selection criterion for the lower peaks are completely lost.

In the case of Gaussian distribution for the background matter, eq. (3.40) takes the even simpler form

$$\xi^{(2)}_{\nu,\mathrm{R}}(x_1,x_2) \;=\; -1 + exp\left\{\left(\frac{\nu}{\sigma_{\mathrm{R}}}\right)^2 \xi^{(2)}_{\mathrm{R}}(x_1,x_2)\right\}, \tag{3.42}$$

and for large separations, when $\xi^{(2)}_{\nu,\mathrm{R}} \ll 1$,

$$\xi^{(2)}_{\nu,\mathrm{R}}(x_1,x_2) \;=\; \left(\frac{\nu}{\sigma_{\mathrm{R}}}\right)^2 \xi^{(2)}_{\mathrm{R}}(x_1,x_2)\,. \tag{3.43}$$

Thus, in the limits of validity of such approximations, the effect of a biased distribution of object is that of amplifying the clustering and, consequently, the correlation strength of the background by a factor $(\nu/\sigma_{\mathrm{R}})^2$.

In particular, if we assume the power law $\xi^{(2)}_{\mathrm{R}}(r) = (r_o/r)^\gamma$ holds, as suggested by observational data (see Chapter 1), eq. (3.43) gives

$$\xi^{(2)}_{\nu,\mathrm{R}}(r) \;=\; \left(\frac{\nu}{\sigma_{\mathrm{R}}}\right)^2 \left(\frac{r_o}{r}\right)^\gamma \;=\; \left(\frac{r'_o}{r}\right)^\gamma, \tag{3.44}$$

where the correlation length for the biased field is

$$r'_o \;=\; \left(\frac{\nu}{\sigma_{\mathrm{R}}}\right)^{\frac{2}{\gamma}} r_o\,. \tag{3.45}$$

This relation shows how an increase in the clustering, due to the effect of the bias, implies an increase of the correlation length r_o. In particular, if the galaxy distribution and the cluster one are characterized by different values of the biasing level ν and of the smoothing radius R, the respective clustering lengths also turn out to be different, as suggested by observational evidences.

As far as the 3-point correlation function is concerned, from eq. (3.41) we can extract its connected part in the form

$$\begin{aligned}
&\zeta^{(3)}_{\nu,\mathrm{R}}(x_1,x_2,x_3) \;= \\
&\quad= \; G^{(3)}(x_1,x_2,x_3)\,[\xi^{(2)}_{\nu,\mathrm{R}}(x_1,x_2)\,\xi^{(2)}_{\nu,\mathrm{R}}(x_2,x_3) + ...3 \;\; terms] + \\
&\quad+ \; \xi^{(2)}_{\nu,\mathrm{R}}(x_1,x_2)\,\xi^{(2)}_{\nu,\mathrm{R}}(x_2,x_3)\,\xi^{(2)}_{\nu,\mathrm{R}}(x_3,x_1) + \\
&\quad+ \; [G^{(3)}(x_1,x_2,x_3) - 1]\,[1 + \xi^{(2)}_{\nu,\mathrm{R}}(x_1,x_2) + ...3 \;\; terms]\,.
\end{aligned} \tag{3.46}$$

The above expression is completely identical to that deduced in the literature for the θ-threshold case [134]. It is easy to show that for a non–Gaussian background we have $G^{(3)} \neq 1$. In the Gaussian case, $G^{(3)} = 1$ and we recover the scaling relation

$$\xi^{(3)}_{\nu,\mathrm{R}}(x_1, x_2, x_3) \;=\; [1 + \xi^{(2)}_{\nu,\mathrm{R}}(x_1, x_2)] \times ...3 \;\; terms \tag{3.47}$$

deduced by Kirkwood [114] in the study of the distribution of the molecules in a real gas. If $\xi^{(2)}(r) < 1$, the cubic term in eq. (3.47) becomes negligible. However, for the distributions of galaxies and clusters there results $\xi^{(2)}(r) > 1$ for the range of separations r where $\xi^{(3)}$ is investigated, so that the cubic term should be dominant. However, as we have already seen in Chapter 1, analysis of homogeneous galaxy samples indicates that

$$\zeta^{(3)}_g(x_1, x_2, x_3) \;=\; Q\,[\xi^{(2)}_g(x_1, x_2)\xi^{(2)}_g(x_2, x_3) + ...3 \;\; terms] \tag{3.48}$$

with $Q \simeq 1$, in contrast with eq. (3.47). (Let us however remember that a good fit of data on the 3-point function in the Zwicky sample has been also obtained by assuming the Kirkwood expression [26].) Several lines of evidence also exist that a relation similar to eq. (3.48) holds for the statistics of the distribution of galaxy clusters. Such discrepancies between the observed distribution of objects and the predictions of the biased model could indicate that the limits in which we deduced the relation (3.47) (*i.e.*, $\nu \gg 1$ and Gaussian background distribution) are not satisfied. In particular, the distribution of galaxies can arise from the distribution of matter only after a moderate bias ($\nu \sim 1$) has been applied, while non–Gaussianity in the background statistics can also play a role.

3.6 Galaxy–cluster cross–correlations

As we have seen in §1.3, the joint analysis of homogeneous samples of galaxies and clusters gives informations about the relative distribution of the two classes of objects by means of the galaxy–cluster cross–correlation function. In order to see how cross–correlations arise in the biased model described in the previous section, let us consider the two biased fields $\rho_g(x)$ and $\rho_c(x)$, that represent the distributions of galaxies and clusters respectively. The two fields involve different choices for the biasing level ν, for the smoothing radius R and for the threshold function $f(\alpha)$, because different scales and physical formation processes are involved.

Accordingly, let us assume that the biased field

$$\rho_g(x) \;=\; f_g[\delta_{\mathrm{R}_g}(x) - \nu_g \sigma_{\mathrm{R}_g}] \tag{3.49}$$

describes the spatial distribution of galaxies, while

$$\rho_c(x) \;=\; f_c[\delta_{\mathrm{R}_c}(x) - \nu_c \sigma_{\mathrm{R}_c}] \tag{3.50}$$

represents the distribution of clusters. Then, the joint probability of finding a cluster at the point x_1 and a galaxy at x_2 is defined by

$$\Pi^{(2)}_{cg}(x_1,x_2) \equiv < \rho_c(x_1)\rho_g(x_2) > = \int D[\delta(x)]\, P[\delta(x)]\rho_c(x_1)\rho_g(x_2)\,, \qquad (3.51)$$

while the galaxy–cluster cross-correlation function is

$$\xi^{(2)}_{cg}(x_1,x_2) = \frac{\Pi^{(2)}_{cg}(x_1,x_2)}{\Pi^{(1)}_c \Pi^{(1)}_g} - 1\,. \qquad (3.52)$$

Following the calculations reported in Appendix A.2, we get for the joint probability (3.51) the expression

$$\Pi^{(2)}_{cg}(x_1,x_2) = \sigma_{\mathrm{R}_c}^{-l_c}\sigma_{\mathrm{R}_g}^{-l_g} e^{h_c(0)+h_g(0)} \sum_{L=0}^{\infty}\sum_{[m_L]}\Big[\prod_{n=1}^{L}\prod_{j=0}^{n}\Big(\frac{W^{(n)}_{[\mathrm{R}_c,j;\mathrm{R}_g,n-j]}}{j!\,(n-j)!}\Big)^{m_{n,j}}\frac{1}{m_{n,j}!}\Big] \times$$
$$\times\; a_{\mathbf{m}}(2^{-1/2}\nu_c)\, a_{L-\mathbf{m}}(2^{-1/2}\nu_g)\,. \qquad (3.53)$$

Here, the quantities

$$W^{(n)}_{[\mathrm{R}_c,j;\mathrm{R}_g,n-j]} = w^{(n)}_{[\mathrm{R}_c,j;\mathrm{R}_g,n-j]} + \frac{h_c^{(j)}(0)}{(i\sigma_{\mathrm{R}_c})^j}\,\delta_{nj} + \frac{h_g^{(n-j)}(0)}{(i\sigma_{\mathrm{R}_g})^{n-j}}\,\delta_{0j} \qquad (3.54)$$

and

$$w^{(n)}_{[R_c,j;R_g,n-j]} = \frac{\xi^{(n)}_{con,[R_c,j;R_g,n-j]}}{\sigma^j_{R_c}\sigma^{n-j}_{R_g}}$$
$$w^{(2)}_{[R_c,j;R_g,n-j]} = 0 \qquad if \quad x_{r_1} = x_{r_2} \qquad (3.55)$$

represent the generalizations of the analogous quantities defined in the previous section by eqs. (3.10) and (3.12), respectively. Moreover, in eq. (3.53) there appear the integers $m_{n,j}$, such that $\sum_{j=0}^{n} m_{n,j} = m_n$, while $\mathbf{m} = \sum_{n=1}^{L}\sum_{j=1}^{n} j m_{n,j}$.

In this case too, the evident complexity of eq. (3.53) is a direct consequence of its generality. In order to simplify the expression of the cross–correlation function, let us consider the high–threshold approximations $\nu_c \gg 1$ and $\nu_g \gg 1$, for both the galaxy and cluster biased fields. In this limit, eq. (3.52) becomes

$$\xi^{(2)}_{cg}(x_1,x_2) = -1 + exp\Big[\sum_{n=2}^{\infty}\sum_{j=1}^{n-1}\nu_c^j\nu_g^{n-j}\frac{w^{(n)}_{[\mathrm{R}_c,j;\mathrm{R}_g,n-j]}}{j!\,(n-j)!}\Big]\,, \qquad (3.56)$$

so that the high–threshold approximation still gives a result that is independent of the non–θ shape of the threshold function.

As already seen in S1.3, the galaxy background cross–correlation function has been used in literature for investigating the distribution of galaxies around Abell

clusters [182,121]. In fact, the joint probability $\Pi^{(2)}_{cg}(x_1, x_2)$ evaluated for $x_1 = x_2$ represents the probability that at a point we find a galaxy contained inside a cluster. Then, $\Pi^{(1)}_c$ being the fraction of volume occupied by clusters, the quantity $\Pi^{(2)}_{cg}(x,x)/\Pi^{(1)}_c$, that describes the fraction of cluster volume occupied by galaxies, is tightly related to the galaxy density inside clusters.

A generalization of cross–correlations to higher orders is also possible. For example, at the third order, we can define

$$\begin{aligned} \Pi^{(3)}_{cgg}(x_1,x_2,x_3) &= \Pi^{(1)}_c [\Pi^{(1)}_g]^2 \times \\ \times \; [1 + \xi^{(2)}_{cg}(x_1,x_2) + \xi^{(2)}_{gg}(x_2,x_3) + \xi^{(2)}_{gc}(x_3,x_1) + \zeta_{cgg}(x_1,x_2,x_3)] & \end{aligned} \tag{3.57}$$

as the joint probability of having a cluster in x_1 and two galaxies in x_2 and x_3. The dependence of eq. (3.57) on the threshold function $f(\alpha)$, on ν and on R can be deduced in a similar fashion to the procedure reported in Appendix A.2 to obtaine $\Pi^{(2)}_{cg}$.

The concept of cross–correlations can be generalized to include any joint statistical analysis of two different distributions. In Chapter 5 we will describe a method for investigating the cross–correlation properties of galaxy and background matter distributions that is based on the analysis of spiral galaxy rotation curves.

3.7 Two examples of threshold functions

In this section, we shall consider two distinct threshold functions from the analytical point of view. The shapes of these thresholds, that are shown in Figure 3.3, are chosen in view of their possible physical meanings, to be considered in the next chapter, where we also investigate their effects on the mass function and on the 2-point correlation function of galaxy clusters.

3.7.1 The erfc-threshold

A first example we shall treat is given by

$$\rho_{\nu,\mathrm{R}}(x) = \frac{1}{\sqrt{2\pi\Delta^2}} \int_{-\infty}^{\delta_{\mathrm{R}}(x)-\nu\sigma_{\mathrm{R}}} dy\, e^{-\frac{y^2}{2\Delta^2}} . \tag{3.58}$$

We indicate this threshold as *erfc*-threshold. It is clear that, for $\Delta \to 0$, the *erfc*-threshold gives back the usual θ-threshold. For $\Delta \neq 0$, this threshold describes a situation with non–zero probability for fluctuations below $\nu\sigma_{\mathrm{R}}$ to turn into real objects, and with a symmetrical probability that also fluctuations exceeding $\nu\sigma_{\mathrm{R}}$ be

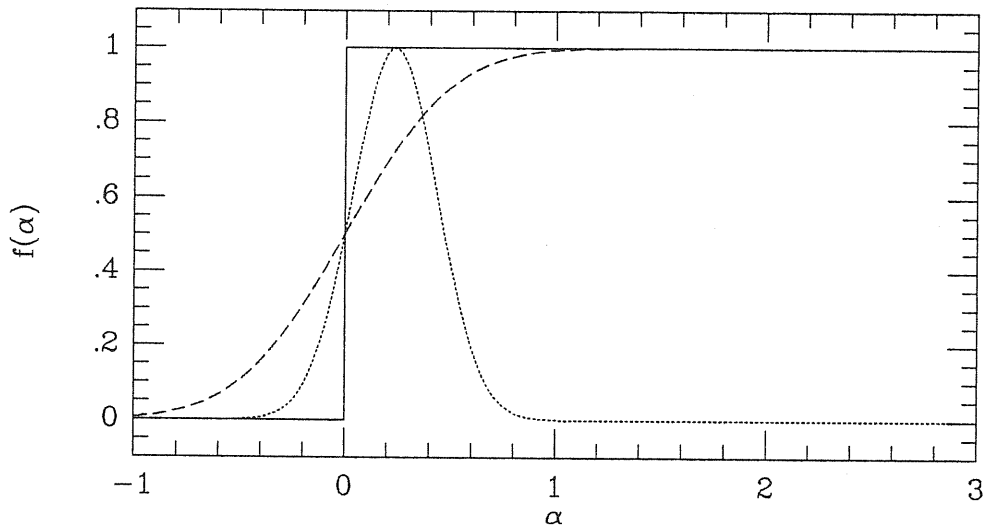

Figure 3.3: *The shapes of different threshold functions. The solid lines represents the θ-threshold 3.6, the dashed curve correspond to the erfc-threshold 3.58, while the dotted line is the Gaussian threshold 3.64.*

sterile. Owing to eq. (3.11), we find

$$\frac{1}{\sqrt{2\pi}}\int_{-\infty}^{+\infty} d\alpha\, f'(\alpha)e^{i\alpha\phi} \;=\; \frac{1}{2\pi\Delta}\int_{-\infty}^{+\infty} dz\, e^{-\frac{z^2}{2\Delta^2}+i\phi z} \;=\; \frac{e^{-\frac{\Delta^2\phi^2}{2}}}{\sqrt{2\pi}}. \tag{3.59}$$

Hence $l = 0$, while the expression of

$$h(\phi) \;=\; -\frac{1}{2}\,ln\,(2\pi) - \frac{1}{2}\Delta^2\phi^2$$

turns out to be fairly easy to handle and yields

$$h(0) \;=\; -\frac{1}{2}\,ln\,(2\pi) \quad ; \quad h"(0) \;=\; -\Delta^2 \quad ; \quad h^{(n)}(0) \;=\; 0 \quad for\ n \neq 0,2\,. \tag{3.60}$$

Therefore, $W^{(n)}_{\mathrm{R},[r_n]} = w^{(n)}_{\mathrm{R},[r_n]}$ for all $n \geq 2$.

In the high–threshold limit, the N-point joint probability will then read

$$\Pi^{(N)}_{\nu,\mathrm{R}}(x_1,...,x_N) \;=\; (2\pi\nu^2)^{-N/2}e^{-\frac{N\nu^2}{2}[1-(\frac{\Delta}{\sigma_\mathrm{R}})^2]}exp\Big\{\sum_{n=2}^{\infty}\frac{\nu^n}{n!}\sum_{[r_n]=1}^{N} w^{(n)}_{\mathrm{R},[r_n]}\Big\} \tag{3.61}$$

and, in particular, the fraction of volume occupied by objects is

$$\Pi^{(1)}_{\nu,\mathrm{R}} \;=<\rho_{\nu,\mathrm{R}}(x)> \;=\; (2\pi\nu^2)^{-1/2}e^{-\frac{\nu^2}{2}[1-(\frac{\Delta}{\sigma_\mathrm{R}})^2]}exp\Big\{\sum_{n=3}^{\infty}\frac{\nu^n}{n!}w^{(n)}_{\mathrm{R}}\Big\}\,. \tag{3.62}$$

It should be noted that $\Pi^{(1)}_{\nu,\mathrm{R}}$ turns out to be an increasing function of Δ. If we consider the ratios

$$\frac{[\Pi^{(N)}_{\nu,\mathrm{R}}]_{erfc}}{[\Pi^{(N)}_{\nu,\mathrm{R}}]_{\theta}} \;=\; exp\Big[\frac{N}{2}\Big(\frac{\nu\Delta}{\sigma_\mathrm{R}}\Big)\Big] \tag{3.63}$$

between the joint probabilities obtainable from $erfc$-threshold and θ-threshold, we see that, for $\Delta \to 0$ they give back 1, as expected.

3.7.2 The Gaussian threshold

A further significant example of threshold function is given by

$$\rho_{\nu,\mathrm{R}}(x) = exp\left\{-\frac{1}{2\Sigma^2}[\delta_{\mathrm{R}}(x) - \kappa\nu\sigma_{\mathrm{R}}]^2\right\}, \tag{3.64}$$

that we shall denote as the *Gaussian* threshold (not to be confused with the Gaussian or the non–Gaussian nature of the background distribution). In eq. (3.64), $\kappa = 1 + \Sigma(2\log 2)^{1/2}$ is defined such that fluctuations with $\delta = \nu\sigma_{\mathrm{R}}$ have probability 1/2 to develop into an object, in analogy with the $erfc$-threshold. The characteristic of this threshold is to select fluctuations in a given range of amplitudes. This range is centered on $\kappa\nu\sigma_{\mathrm{R}}$ and its amplitude is fixed by the parameter Σ. In this way, further to exclude small amplitude fluctuations from generating observable objects, very large fluctuations on a given scale are also supposed not to leave any visible imprint on such a scale. In the limit $\Sigma \to 0$, the Gaussian threshold degenerates into a Dirac delta–function and the only selected fluctuations are those with amplitude exactly equal to $\kappa\nu\sigma_{\mathrm{R}}$. On the other hand, there are no limits where the θ-bias case is recovered. Possible physical meaning of the *Gaussian* threshold will be discussed in the next chapter.

As for the $erfc$-threshold, the shape of

$$h(\phi) = ln\left(\frac{1}{\Sigma}\right) - \frac{\phi^2}{2\Sigma^2}$$

obtained according to eq. (3.11), is such that $W^{(n)}_{\mathrm{R},[r_n]} = w^{(n)}_{\mathrm{R},[r_n]}$ for all $n \geq 2$. The behaviour at the origin, instead, gives $l = 1$. Accordingly, the joint probability expression in the high–threshold limit reads

$$\Pi^{(N)}_{\nu,\mathrm{R}}(x_1,...,x_{\mathrm{N}}) = \left(\frac{\Sigma}{\sigma_{\mathrm{R}}}\right)^N e^{-\frac{N\kappa^2}{2}\frac{\nu\Sigma}{\sigma_{\mathrm{R}}}\left[\left(\frac{\sigma}{\Sigma}\right)^2-1\right]} exp\left\{\sum_{n=2}^{\infty}\frac{(\kappa\nu)^n}{n!}\sum_{[r_n]=1}^{N} w^{(n)}_{\mathrm{R},[r_n]}\right\}, \tag{3.65}$$

while the ratios

$$\frac{[\Pi^{(N)}_{\nu,\mathrm{R}}]_{gauss}}{[\Pi^{(N)}_{\nu,\mathrm{R}}]_{\theta}} = (2\pi)^{N/2}\left(\frac{\nu\Sigma}{\sigma_{\mathrm{R}}}\right) e^{-\frac{N\kappa^2}{2}\frac{\nu\Sigma}{\sigma_{\mathrm{R}}}\left[\left(\frac{\sigma_{\mathrm{R}}}{\Sigma}\right)^2-1+\kappa^{-2}\left(\frac{\sigma_{\mathrm{R}}}{\Sigma}\right)^2\right]} \tag{3.66}$$

are increasing functions of $(\nu\Sigma/\sigma_{\mathrm{R}})$.

For large ν, the fraction of volume occupied by objects reads

$$\Pi^{(1)}_{\nu,\mathrm{R}} = \left(\frac{\Sigma}{\sigma_{\mathrm{R}}}\right) e^{-\frac{\kappa^2}{2}\frac{\nu\Sigma}{\sigma_{\mathrm{R}}}\left[\left(\frac{\sigma}{\Sigma}\right)^2-1\right]} exp\left\{\sum_{n=3}^{\infty}\frac{(\kappa\nu)^n}{n!} w^{(n)}_{\mathrm{R}}\right\}. \tag{3.67}$$

In the Gaussian background case, the exponential factor becomes 1.

As a final remark, let us observe that, according to eqs. (3.62) and (3.67), it is possible to relate in a simple way the number densities obtained with the *erfc* and *Gaussian* thresholds to the θ-threshold expression. These relations read

$$< \rho_{\nu,\mathrm{R}} >_{erfc} \;=\; < \rho_{\nu,\mathrm{R}} >_{\theta} \; exp\Big[\Big(\frac{\nu\Delta}{\sqrt{2}\sigma_{\mathrm{R}}}\Big)^2\Big]\,; \tag{3.68}$$

$$< \rho_{\nu,\mathrm{R}} >_{Gaussian} \;=\; < \rho_{\nu,\mathrm{R}} >_{\theta} \; \Big(\frac{\nu\Sigma}{\sigma_{\mathrm{R}}}\Big)\, exp\Big[\Big(\frac{\nu\Sigma}{\sqrt{2}\sigma_{\mathrm{R}}}\Big)^2\Big] \tag{3.69}$$

and hold for both Gaussian and non–Gaussian background matter distributions.

3.8 The exponential biased field

Even though the class of threshold function we considered in §3.3 is quite general, however it does not contain all the possible choices for the biased field. From a technical point of view, the restriction lies in the fact that eq. (3.11) requires the existence of the Fourier transform for $f'(\alpha)$, the first derivative of the threshold function. However, there exist also particular threshold functions of physical interest for which such a hypothesis does not hold. A significant example is represented by the biased field

$$\rho_{\nu,\mathrm{R}}(x) \;=\; A\, e^{\frac{\nu}{\sigma_{\mathrm{R}}}\delta_{\mathrm{R}}(x)}\,, \tag{3.70}$$

that was introduced by Kaiser & Davis [113] for relating the luminosity field generated by galaxies to the underlying matter distribution. It is easy to show that for the field (3.70) it is not possible to define the function $h(\phi)$ and the integer l according to eq. (3.11).

In this section we generalize the procedure introduced in the previous sections to a more general class of threshold functions that includes the exponential threshold (3.70). Let us consider the class of threshold functions that can be written in the form

$$\rho_{\nu,\mu,R}(x) \;=\; e^{\frac{\nu}{\sigma_{\mathrm{R}}}\delta_{\mathrm{R}}(x)} f[\delta_{\mathrm{R}}(x) - \mu\sigma_{\mathrm{R}}]\,. \tag{3.71}$$

Here $f(\alpha)$ is such that its first derivative can be Fourier–transformed. In the field (3.71), the parameters μ and ν both play a role in defining the selected fluctuation.

According to the definition (3.8) for the N-point joint probability, after some calculations (see Appendix A.3), we get

$$\Pi^{(N)}_{\nu,\mu,\mathrm{R}}(x_1,...x_{\mathrm{N}}) \;=\; \sigma_{\mathrm{R}}^{-lN} e^{-\frac{N\nu^2}{2}} e^{Nh(i\frac{\nu}{\sigma_{\mathrm{R}}})} \times$$

$$\times \sum_{L=0}^{\infty} \sum_{[m_L]} \left[\prod_{n=1}^{L} \prod_{[r_n]=1}^{N} \left(\frac{W^{(n)}_{\mathrm{R},[r_n]}}{n!} \right)^{m_{n,[r_n]}} \frac{1}{m_{n,[r_n]}!} \right] \times \prod_{r=1}^{N} A^{(l)}_{\mathbf{m}(r)}[2^{-1/2}(\mu - \nu)] \,. \quad (3.72)$$

In this expression, we used the functions

$$W^{(n)}_{\mathrm{R},[r_n]} = \frac{h^{(n)}(i\nu/\sigma_{\mathrm{R}})}{(i\sigma_{\mathrm{R}})^n} \prod_{k=1}^{n-1} \delta_{r_k, r_{k+1}} + w^{(n)}_{\mathrm{R},[r_n]} \,. \quad (3.73)$$

that represents the analogous of the quantities (3.10). Moreover, in eq. (3.72), we introduced the coefficients

$$A^{(l)}_{\mathbf{m}(r)}(z) = \sum_{k=0}^{\mathbf{m}(r)} \frac{\mathbf{m}(r)!\,(-\nu)^{\mathbf{m}(r)-k}}{k!\,(\mathbf{m}(r)-k)!}\, a^{(l)}_k(z) \,. \quad (3.74)$$

From the expression (3.72) for the joint probability, it is possible to reproduce the same results obtained in Sections 3.4 and 3.5 for the correlation functions of the biased field. Let us observe that, in this case, the high–threshold limit is given by the condition $z \equiv \mu - \nu \gg 1$. Under this condition, the asymptotic form of eq. (3.74) is

$$A^{(l)}_{\mathbf{m}(r)}(z \gg 1) \simeq a^{(l)}_{\mathbf{m}(r)}(z \gg 1) \simeq (2^{1/2} z)^{\mathbf{m}(r)+l-1} e^{-z^2} \,. \quad (3.75)$$

Consequently, the joint probability (3.72) becomes

$$\Pi^{(N)}_{\nu,\mu,\mathrm{R}}(x_1, \ldots x_{\mathrm{N}}) =$$
$$= \sigma_{\mathrm{R}}^{-lN} \nu^{N(l-1)} e^{-\frac{N\nu^2}{2}} e^{Nh(0)} exp\left\{ \sum_{n=2}^{\infty} \frac{\nu^n}{n!} \sum_{[r_n]=1}^{N} w^{(n)}_{\mathrm{R},[r_n]} \right\} , \quad (3.76)$$

so that the correlations of the biased field turn out to be independent of the shape of the threshold function also in this case. This result generalizes what previously obtained by Kaiser & Davis [113] and by Szalay [189]; indeed, they found that, in the high threshold limit and for Gaussian background distribution, the 2-point correlation function for the field (3.70) coincide with that of the θ–threshold.

The contents of this chapter, with the exception of the first two sections, are included in two papers that have been already published in *Astronomy & Astrophysics* [30] and in the *Astrophysical Journal* [31].

Chapter 4

Observational tests for biased models

There can be little doubt that the bias paradigm has marked a significant step forward in our understanding of the relation between matter and light large–scale distributions. Indeed, the success of the bias approach in accounting for the observed different clustering length of galaxies and galaxy systems suggests that a functional relation should exist that relates the background matter distribution to the object distribution. However, tentative applications of the Kaiser's original bias prescription [112] (*i.e.*, only peaks with amplitude above a fixed threshold are identified with observable objects) to the study of the correlation functions and multiplicity function of cosmic structures seems to indicate a possible agreement with observational data only at the zero-th order level.

In this chapter we shall pursue the idea that this is mostly due to the need of perfecting the analytical tool. In particular we will use the technical background described in Chapter 3 for general biased models to include the effects of non–linear phenomena, that probably occur during the formation of the observable structures (see §3.2).

In what follows we restrict our analysis only to statistical properties of galaxy systems (*i.e.*, groups and clusters). Indeed, a comparison between predictions of biased models and observational data does not involve serious problems on cluster scales, while it gets more difficult on galaxy scales. In fact, on the latter scales, the evolution of fluctuations can be widely non–linear and the only adequate approach seems to be based on N–body simulations [66,49,135,198].

4.1 Tentative analysis of non–sphericity and merging effects

In this section we tentatively relate the *erfc* and the *Gaussian* thresholds introduced in §3.7 to non–sphericity in gravitational growth and to merging among different scale fluctuations.

The smoothing operation of the fluctuation field, that we discussed in §2.6, tends to erase all morphological details of primeval fluctuations below the smoothing scale R. The eventual growth of their amplitude, due to self–gravity effects, is however known to show traces of such features. Pancake formation in non–spherical collapses has been widely discussed. The formation of *caustics* and fragmentation effects are however not so relevant in the present discussion. In a *hierarchical* bottom–up scenario, in which we are primarily concerned, smaller scale objects need not form during a larger scale collapse and the dynamics of collapses above galactic scale is not substantially affected by dissipative effects. Attention should be rather focused on the alteration of the time and density scales occurring because of non sphericity. It has been known for years (see, *e.g.*, [91]) that a fairly precise schedule characterizes spherical collapses. If t_1 is the time at which an overdense lump of matter reaches its maximum expansion, collapse is expected to follow until a time $t_2 \simeq 2\,t_1$ and virialization is reached at about $t_3 \simeq 3\,t_1$. The density contrasts at the times t_1, t_2, t_3 depend on the present density parameter Ω_o, and, for $\Omega_o = 1$, are $\delta = 4.55, \simeq 300, \simeq 400$ respectively. This time and density sequence is however connected with the assumption of sphericity. Numerical experiments [55] show that substantial discrepancies arise when non–spherical geometries are considered. It is also interesting to compare the above value for the density contrast with those obtainable extrapolating a linear theory. They are much smaller and, for the times t_1 and t_2, amount to 1.06 and 1.69 respectively.

The degree of evolution and the value of the density contrast, that a fluctuation on a given scale has reached at the present time t_o cannot be therefore uniquely related to its primeval amplitude at – say – recombination end. Let us assume that, under pure sphericity assumption, an object on scale R would have formed if $\delta_{\rm R} > \nu\sigma_{\rm R}$. A–sphericity gives place to a spread around the critical value $\nu\sigma_{\rm R}$, so that an *erfc*-threshold is the simplest way of correcting for alteration of the time–density-contrast sequence.

It is however clear that the importance of the correction will be strictly related to the average height of the peaks considered over each mass–scale. Very large fluctuations tend to be increasingly spherical and the dependence of the Δ parameter, that specify the shape of the *erfc*-threshold, on R or on the related mass–scale $M_{\rm R}$

should make this point evident. Thus, assuming

$$\Delta(M) = \left(\frac{\tilde{M}}{M}\right)^{\beta} \tag{4.1}$$

with $\beta > 0$ seems therefore reasonable. In eq. (4.1) the normalization of Δ is provided by the reference mass scale $\tilde{M}$. In §4.2 and §4.3 we shall report the result of an approach to observational data on multiplicity function and rich–cluster 2-point correlation functions, respectively, based on the *erfc*-threshold.

Besides a–sphericity effects, an important role is likely to be played by the disruption of fluctuations during their collapse or virialization stages, because of their merging within wider fluctuations which contained them, but whose gravitational growth had a longer time–scale.

It is then likely that the possibility of observing an object on a given mass–scale decreases if we consider systems which had a large time to interact with and/or within other objects. The *Gaussian* threshold is an attempt to take also these effects into account. That observable objects are those sufficiently old to reach an appreciable contrast and sufficiently young not to vanish in wider structures is certainly an appealing idea. Problems can rather arise from approximating the increase and the decrease of the observational probability, around the critical value $\kappa\nu\sigma_R$, by a strictly symmetrical function. Furthermore greater amplitudes are encountered with smaller frequency, unless with are faced with very peculiar and highly non–Gaussian background distributions.

4.2 Comparison with data on multiplicity function

In this section we consider the impact of non–sphericity on the shape of the multiplicity function (see §1.4). After a review of some theoretical models for describing the mass spectrum of galaxy systems, we propose a tentative fit to the general multiplicity function for Turner & Gott (TG) groups and Abell clusters, by considering the *erfc* threshold to select background fluctuations.

4.2.1 Theoretical approaches to the mass function

Detailed expressions for the mass function of cosmic structures, $n(M)$, based on the simple (*i.e.*, with θ-threshold) biased theories, have been obtained by several authors [190,142,133,127,46,45] (see also ref. [146] for a detailed review). Both Gaussian and non–Gaussian background distributions were considered and objects were assumed to be defined either by volumes above a critical density threshold or by peaks of the

fluctuation field. A comparison with observed luminosity functions $\Phi(L)$ was then performed mostly under the assumption of a constant M/L ratio, allowing one to assume $\Phi(L) \propto n(M)$.

It is widely recognized that observational data that have been used for defining the multiplicity function $\Phi(L)$ are fairly inhomogeneous, being obtained with different techniques and definitions over different scale ranges [180,93,6]. In spite of these problems, it is usual to consider the so–called *universal Schechter function*

$$\Phi(L) \;=\; \Phi^* \left(\frac{L}{L^*}\right)^{\alpha} e^{-\left(\frac{L}{L^*}\right)}, \tag{4.2}$$

that we have already introduced in §1.4, as a good fit to observations.

Fitting $\Phi(L)$ data by a product of a power–law times an exponential cut–off was however initially suggested by the outputs of the classical Press & Schechter model [167], where the growth of clustering in the Universe was studied, starting from primeval Gaussian perturbation with mass–variance $\sigma_{\rm M} = (M_o/M)^{\beta}$ ($\beta = const$). According to this model, we can work out the expression (1.31), that can be rewritten in the form

$$n(M) \;=\; n^* \left(\frac{M}{M_c}\right)^{\beta-2} e^{-\left(\frac{M}{M_c}\right)^{2\beta}}. \tag{4.3}$$

Here

$$n^* \;=\; (1+f)\beta\sqrt{\pi}\,\rho_b\, M_c^{-2} \tag{4.4}$$

($f \sim 1$ accounts for a possible secondary matter infall; see, *e.g.*, ref. [98]), while $M_c = (\delta_c/\sqrt{2})^{1/\beta} M_o$; δ_c is the critical density contrast allowing a density fluctuation to become observable (if, for example, we assume that structures become observable after the recollapse, then $\delta_c = 1.69$).

It should be emphasized that the expression (4.3) for the Press & Schechter mass–function already assumes the validity of a simple bias approach, discriminating fluctuations after comparing them with a precise density contrast. A number of possible effects are therefore excluded from this result: each mass scale is assumed to have a separate evolution and all lumps of matter undergoing gravitational density growth are assumed to follow nearly similar patterns, the only difference being a possible shift in the time–scales.

The impact of such restrictions can actually be severe, as effects like merging, tidal disruption, non–spherical collapses, *etc.* are likely to be important. Should they be the dominant features, the Press & Schechter scenario should perhaps be abandoned in favour of the so–called *kinetic* approach to the mass function. Attempts in this direction were performed by several authors (see ref. [128], for a review). Doubtless, these features are critically relevant in a top–down scenario. In the framework

of this approach it is still possible to obtain an expression

$$n(M) \;=\; n^{*}\Big(\frac{M}{M_c}\Big)^{-\lambda} e^{-\left(\frac{M}{M_c}\right)} \tag{4.5}$$

for the multiplicity function, for $M > M_c$, and a more complex expression for low M. The meaning of M_c is however quite different from above, while λ is assumed to derive from the collapse/fragmentation dynamics, having nothing to do with the primeval spectrum of fluctuations. If the real world is to be related to this latter approach, tracing direct information on *initial* conditions from clustering data seems to be difficult or even vain.

Here we plan to pursue an intermediate program. Still keeping within the *bias* approach, we try to account for a number of other features through suitable forms of the threshold function. As already outlined in the previous chapter, our idea is that the *threshold function* can be used to account for effects other than overcoming a given fluctuation level.

As a matter of fact, a comparison between eqs. (4.3) and (4.2) easily shows that, for a constant M/L ratio, no value of β can furnish the observed Schechter function for galaxy groups and clusters. This fact seems to be independent of the nature (Gaussian or non–Gaussian) of the background matter distribution. The question is then whether effects like merging of different scale fluctuations, non–sphericity in the gravitational growth, *etc.* are responsible for the discrepancy between the shape of $\Phi(L)$ and the expression of $n(M)$ obtained starting from a θ-threshold function. If so, an analysis of $\Phi(L)$ could furnish significant informations on the above effects.

4.2.2 A fit to multiplicity function allowing for non–spherical growing

In the following a tentative fit of data on the multiplicity function of TG groups and Abell clusters will be performed. We shall assume a primeval fluctuation spectrum $|\tilde{\delta}(k)|^2 = Ak^n$ and the CDM transmission factor (see §2.4, eq. (2.77)). According to eq. (2.98), they allow us to work out the dependence on the scale R of the mass variance

$$\sigma_R^2 \;=\; A\,(2\pi)^{-3}\int_0^\infty dk\, k^{2+n}T^2(k)\,\hat{Q}_R^2(kR)\,. \tag{4.6}$$

Here $\hat{Q}_R$ is the Fourier transform of the window function Q_R (see §2.6). The normalization constant A is fixed by requiring that

$$\sigma_{R_g=8h^{-1}Mpc} \;=\; b_g^{-1}\,. \tag{4.7}$$

Here, the *bias parameter* b_g is defined as the ratio between the 2-point correlation functions for galaxies and background, evaluated at the scale R_g. [Let us remember

that, according to Davis & Peebles [52], the variance in the distribution of galaxies is unity at $R_g = 8h^{-1}Mpc$.]

Then if $\Pi^{(1)}_{\delta_c,\mathrm{M}}$ represents the probability of finding an object of mass M (here $\delta_c = \nu\sigma_{\mathrm{R}}$ is the value of the critical threshold), the number density of objects with mass between M and $M + dM$ is given by

$$n(M)\,dM \;=\; (1+f)\,\frac{<\rho_b>}{M}\left|\frac{d\Pi^{(1)}_{\delta_c,\mathrm{M}}}{dM}\right| dM\,. \tag{4.8}$$

In the above expression, the mass scale M is related to the smoothing scale R according to $M = (4\pi/3) <\rho_b> R^3$, once we assume the top–hat filter (2.88).

In order to introduce the effect of non–sphericity in gravitational collapse, let us take the expression

$$\begin{aligned}\Pi^{(1)}_{\delta_c,\mathrm{M}} \;&=\; \frac{1}{2}\,erfc\left(\frac{\delta_c}{\sqrt{2}\sigma_{\mathrm{M}}}\right) + \\ &+\; \frac{1}{\sqrt{2\pi}}\sum_{l=1}^{\infty}\left(\frac{\Delta^2}{2\sigma^2_{\mathrm{M}}}\right)^l \frac{2^{-\frac{l-1}{2}}}{l!}\,exp\left(-\frac{\delta_c^2}{2\sigma^2_{\mathrm{M}}}\right) H_{2l-1}\left(\frac{\delta_c}{\sqrt{2}\sigma_{\mathrm{M}}}\right),\end{aligned} \tag{4.9}$$

that represents the probability of having an object on the scale M, in the case of *erfc*-threshold. In the *r.h.s.* of eq. (4.9) the first term coincides with the contribution obtainable from a θ-threshold. In the second term, the dependence on $\Delta(M)$ appears [see eq. (4.1)]. It can be easily verified that this term vanishes for $\Delta \to 0$. Both $\Delta(M)$ and the critical density contrast δ_c turn out to be always divided by the mass variance σ_{M}. It is therefore convenient to keep the values of δ_c and σ_{M} obtainable from a linear theory.

After differentiating eq. (4.9) with respect to M and substituting in eq. (4.8), we get

$$n(M) \;=\; \frac{<\rho_b>}{M}\,\frac{\delta_c}{\sqrt{\pi}\sigma^2_{\mathrm{M}}}\left|\frac{d\sigma_{\mathrm{M}}}{dM}\right| |1+\Lambda(M)|\,exp\left(-\frac{\delta_c^2}{2\sigma^2_{\mathrm{M}}}\right), \tag{4.10}$$

where the non–sphericity effects are expressed through the term

$$\begin{aligned}\Lambda(M) \;&=\; \sum_{l=1}^{\infty}\frac{2^{-\frac{l+1}{2}}}{l!}\left(\frac{\delta_c}{\sqrt{2}\sigma_{\mathrm{M}}}\right)^{2l-1}\left(\frac{\Delta}{\delta_c}\right)^{2l}\times \\ &\times\; \left[H_{2l+1}\left(\frac{\delta_c}{\sqrt{2}\sigma_{\mathrm{M}}}\right) + \left(\frac{4l}{\Delta}\right)H_{2l-1}\left(\frac{\delta_c}{\sqrt{2}\sigma_{\mathrm{M}}}\right)\frac{d\Delta/dM}{d\sigma_{\mathrm{M}}/dM}\right].\end{aligned} \tag{4.11}$$

For the critical density contrast, in general we shall take

$$\delta_c \;=\; 1.69\,j \tag{4.12}$$

and, in the sequel, the values $j = 1$ (recollapse at the time t_2) and $j = 1.3$ [virialization at $t_3 = (3/2)t_2$] will be considered.

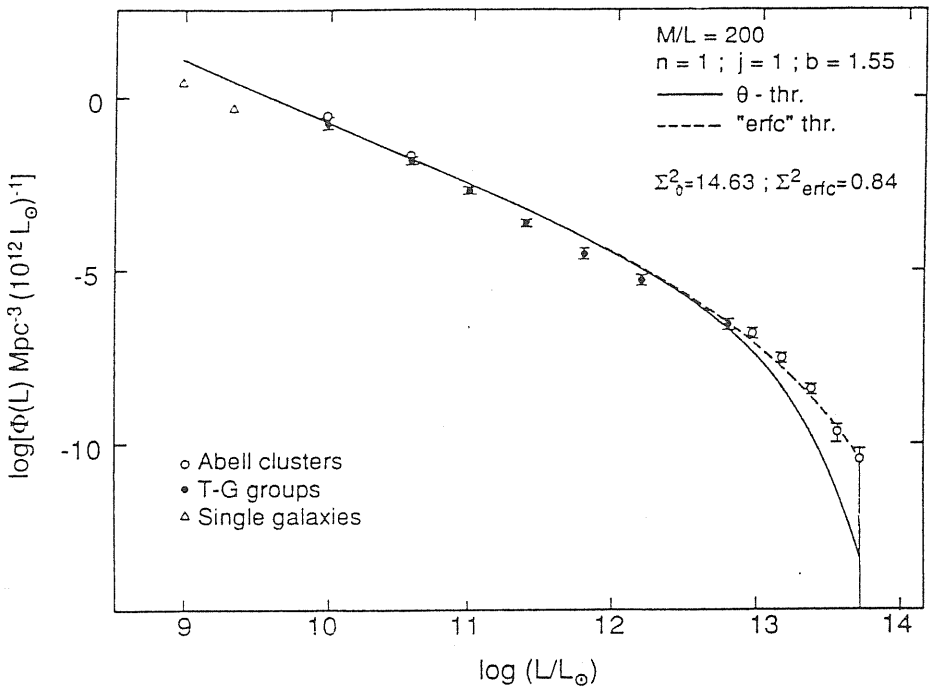

Figure 4.1: *Multiplicity function for galaxy systems. The θ-threshold case and the* erfc-*threshold cases are compared. The values of n and j are selected* a–priori. *The ratio M/L and the bias parameter b are obtained fitting TG data with a θ-threshold. The effects of an* erfc-*threshold are quite relevant in the Abell cluster region.*

In Figure 4.1 we report some fits of data obtained as follows. We assume given *a–priori* values of j and of the spectral index n. Then we determine the best–fit values for the biasing parameter b_g and for the M/L ratio, by considering the TG sample *only* and assuming a θ-threshold function. No attempt is therefore made, at this stage, to fit also Abell cluster data and this avoids treating on the same footing data obtained with different criteria. In the figures, however, also Abell cluster data are shown and we can immediately appreciate how far from theoretical curves, based on the TG groups, the Abell cluster data are apparently set.

Among the different cases we studied, we shall report in Figure 4.1 the case $j = 1$ and $n = 1$. The effect of passing from a θ-threshold to an *erfc*-threshold is clearly visible. One should notice that the correction due to $\Delta \neq 0$ is almost negligible in the mass–range used to fit M/L and b_g. In the Abell cluster mass range, instead, it allows the theoretical curve to rise up to 3 orders of magnitude, allowing a fit which would otherwise appear very poor. The results plotted in Figure 4.1 are obtained with the best fit values $\tilde{M} = 10^{-5.95} M_\odot$ and $\beta = 0.035$. They yield an almost constant $\Delta \sim 0.2$. Keeping such a constant value of Δ in eq. (4.11) would still provide a good fit to data. While this means that the improved fit is obtainable with just one extra parameter, we maintained the 2-parameter starting point in order to show that a nearly constant Δ seems to be actually implied by observational data.

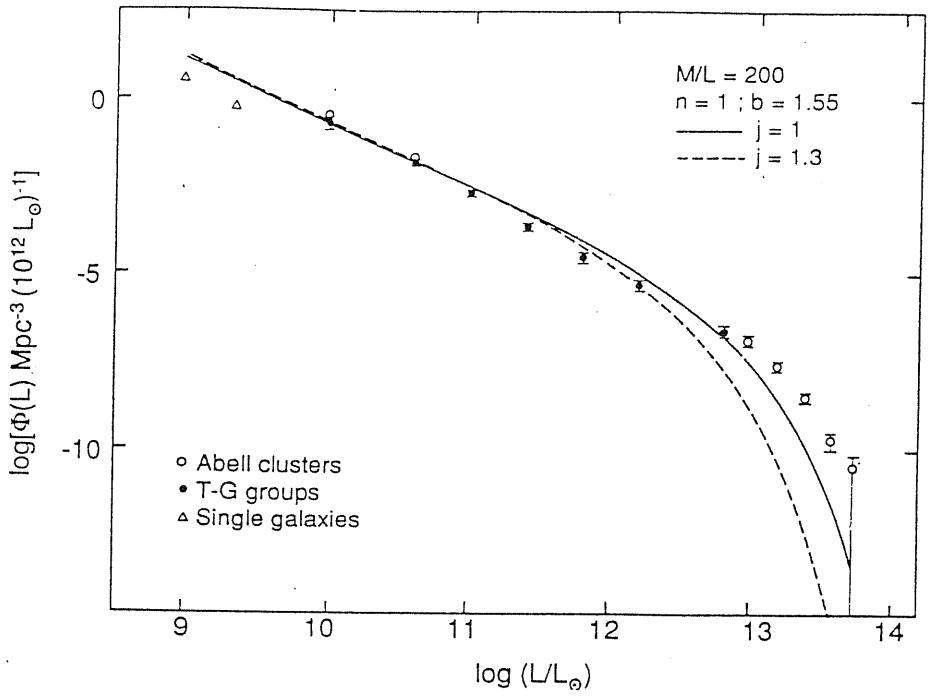

Figure 4.2: *Here the possibility of improving the data fit passing from $j = 1$ to $j = 1.3$ is tested. The dashed curve ($j = 1.3$) seems however to indicate a worse approximation to data. Accordingly, it seems reasonable to conclude that observed clusters are far from virialization.*

All the above fits were ordinary least–squares fits, on a logarithmic scale, obtained by giving all points the same statistical weight (points from individual galaxies were never taken into account). A significant quantity is therefore

$$\Sigma^2 = \sum_{i=1}^{N} (t_1 - \alpha_i)^2 , \tag{4.13}$$

where t_i and α_i are theoretical and observational values on the $N = 12$ mass–scales taken into account. The effect of keeping $\Delta \neq 0$ lowers Σ^2 from 14.65 to 0.84.

The analytical reason which makes the correction so significant on large mass–scales is connected with the behaviour of the ratio $\Delta(M)/\sigma_M$. Just before the Abell cluster mass-range, the transmission factor $T(k)$ shows a significant bend–over, corresponding to a value of $\sigma_M \sim 10^{-1}$. [Let us remember that this value is controlled by the bias parameter b_g, while the mass–scale is determined by the M/L parameter; both were obtained on the basis of the TG sample.] Accordingly, $\Delta(M)/\sigma_M$ approaches unity and, above this critical value, the enhancement of $\Pi^{(1)}_{\delta_c,M}$ becomes particularly significant.

Figure 4.2 shows the effect of passing from $j = 1$ to $j = 1.3$, for the same value of b_g. Although some improvement seems to be possible in the TG luminosity–range, this surely makes the theoretical curve more distant from data in the Abell cluster region.

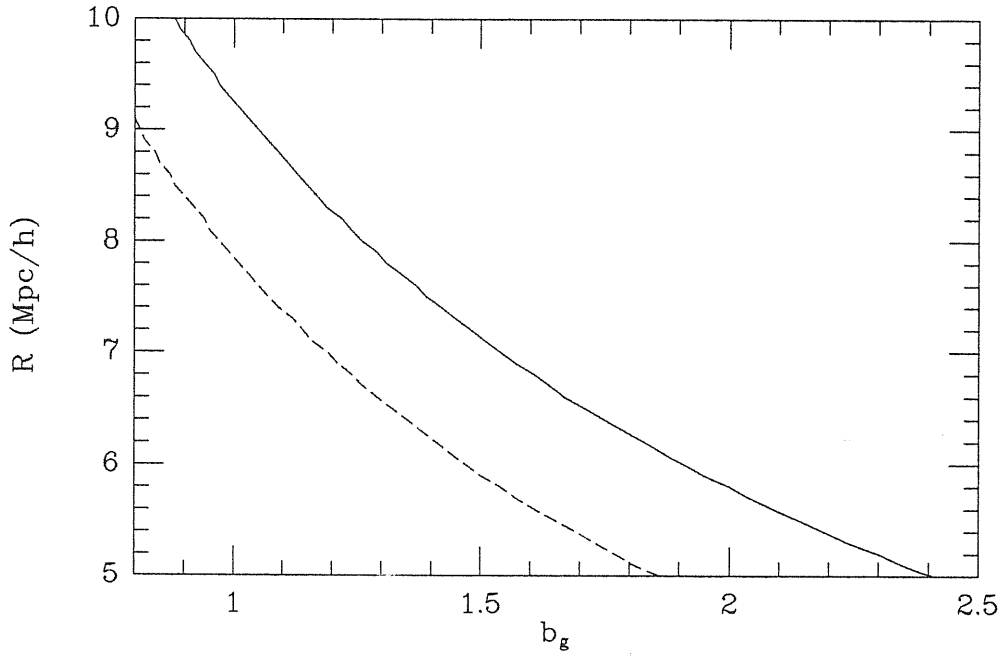

Figure 4.3: *The relation between the smoothing radius R and the galaxy bias factor b_g in the θ–bias case, for the CDM background spectrum, assuming a top–hat winwow function. The solid line corresponds to $j = 1$ (end of recollapse), the dashed line to $j = 1.3$ (virialization).*

A first point which seems to follows from the above fits is that taking a–sphericity into account is significant and that fits of data obtained neglecting it might be misleading. Also the fact that the correction seems to concentrate its effects on the Abell cluster mass range, raising the abundance of such objects with respect to a pure θ-threshold model, might be connected with the observational relevance of the Abell clusters themselves. Their aspect and abundance were such as to attract the observer's attention. The idea that is very tentatively suggested here is that their peculiarities – as well as their connection with lower scale objects – is to be ascribed to the dynamics of non–spherical gravitational growth.

A further significant pattern would be opened if a better observational definition of the multiplicity function $\Phi(L)$ is reached. As already outlined, the definition of Abell clusters [1] and of galaxy groups [194] are significantly different. In spite of that, there seems to be some physical continuity between data concerning these two kinds of samples (see Figures 4.1 and 4.2). This fact is doubtless remarkable, but it is also reasonable to wonder how much it may be altered even by minor changes in the very definition of groups and/or clusters. The Gott & Turner search, based on the 2-dimensional Zwicky sample, assumed an angular density of galaxies σ_g that must be 7.95 times the average density for defining a group (see eq. (1.26)). It is clear that no particular physical meaning is to be attributed to this value of σ_g. In

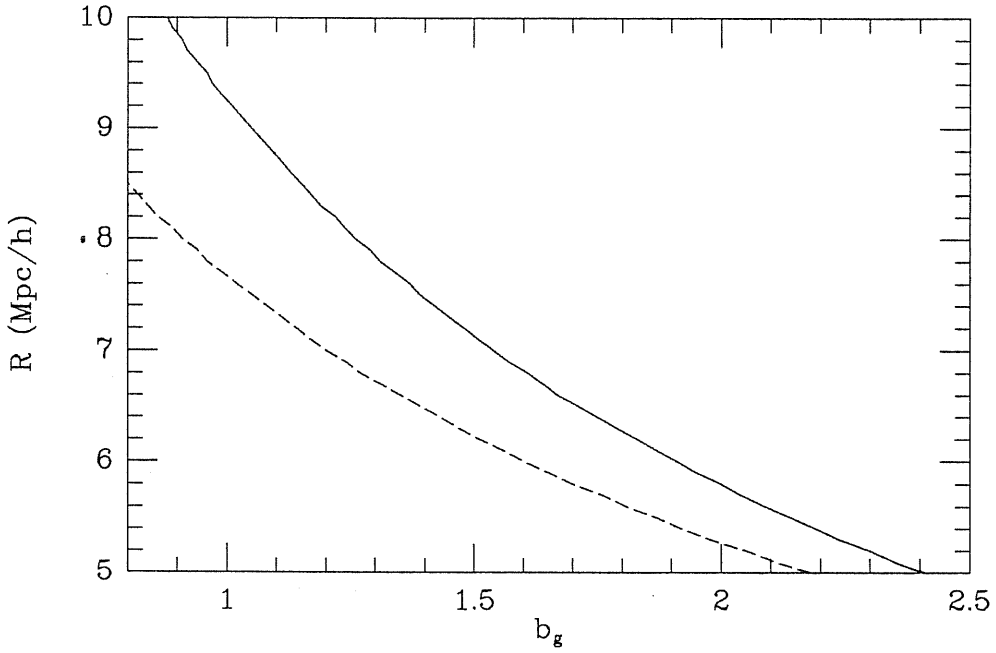

Figure 4.4: *The relation between the smoothing radius R and the galaxy bias factor b_g in the θ–bias case, for different window functions and assuming a CDM background spectrum. The solid line corresponds to the top–hat window, while the dashed line to the Gaussian window.*

this sense, it would be fair to outline the dependence of both $n(M)$ and $\Phi(L)$ on σ_g, replacing the above symbols by $n_{\sigma_g}(M)$ and $\Phi_{\sigma_g}(L)$, or making clear the dependence of theoretical and observational data on parameters like the density contrast.

In our opinion, however, a decisive step for a direct test of any theoretical model would be possible only with the availability of a mass–function directly deduced from observational data, without the need to pass through any assumption about the value of the M/L ratio.

4.3 Comparison with data on cluster correlation function

The possibility of using linear theory on the scales of clustering of rich clusters leads some authors to test biased models *vs* the detected 2-point correlation function of Abell clusters [132,47]. However, despite the simple feature of the rich–cluster 2-point function, agreement with the predictions of the θ-threshold biasing can be achieved only at a qualitative level.

Taking into account non–spherical gravitational growing and merging between fluctuations on different scales by means of the *erfc* and *Gaussian* thresholds respectively, we directly compare our model for the cluster 2-point correlation function,

$$\xi^{(2)}_{\delta_c,\mathrm{R}}(x_1,x_2) \;=\; 1+\frac{\Pi^{(2)}_{\delta_c,\mathrm{R}}(x_1,x_2)}{[\Pi^{(1)}_{\delta_c,\mathrm{R}}]^2}\,, \tag{4.14}$$

with the corresponding observational results obtained by Sutherland & Efstathiou [188] from the analysis of the deep cluster redshift survey of Geller & Huchra [85].

From a general point of view, let us observe that eq. (4.14), together with the normalization requirement (4.7) for the spectrum, causes the cluster 2-point correlation function to depend on the smoothing radius R (rather than on the shape of the window function) and on the bias factor b_g. However, a relation between these two parameter can be found, so reducing the degrees of freedom in our problem. In fact, from the ratio between $\Pi^{(1)}_{\delta_c,\mathrm{R}}$ (fraction of volume occupied by the objects) and the characteristic volume of each object [$V_{\mathrm{R}} = \frac{4}{3}\pi R^3$ for the top-hat window, or $V_{\mathrm{R}} = (2\pi R^2)^{3/2}$ for the Gaussian window], we obtain a prediction for the object number density. The relation between R and b_g is then found by constraining the predicted cluster number density to be equal to the observed one, $n_g = 7\times 10^{-6}h^3 Mpc^{-3}$. However, $\Pi^{(1)}_{\delta_c,\mathrm{R}}$ being dependent on the value of the critical density δ_c, the form of this relation turns out to be dependent on the evolution parameter j. In particular, for a fixed value of R, the corresponding value of b_g is a decreasing function of j (see Figure 4.3). The functional dependence of the smoothing radius R on the bias factor b_g for different window functions is shown in Figure 4.4, while the effects of taking different threshold functions $f(\alpha)$ and different background spectra are shown in Figures 4.6 and 4.8.

Indications on the value of the smoothing radius, and, consequently, of the bias factor too, are obtained through a comparison between the prediction of our model and the observational data on the cluster 2–point correlation function (see Figures 4.5, 4.7, and 4.9). In the case of a top–hat window, a reasonable value for the smoothing radius turns out to be $R = 9\,h^{-1}Mpc$, while $R = 7.5\,h^{-1}Mpc$ for Gaussian window. Indeed, while for smaller values of R the 2–point correlation function is too steep for small separations r, for greater values the correspondent bias factor becomes < 1, in contrast with the idea that galaxies are clustered *at least* as the background matter. Moreover, corresponding to the above value of R, a reasonable galaxy bias factor b_g is obtainable only for $j = 1$, while $j = 1.3$ implies an anti–biasing ($b_g < 1$) in the galaxy distribution. This seems to indicate that clusters of galaxies are observed at about the epoch of recollapse, still far from full virialization (this conclusion is in agreement with other evidence from cluster X–ray emission [76,43]).

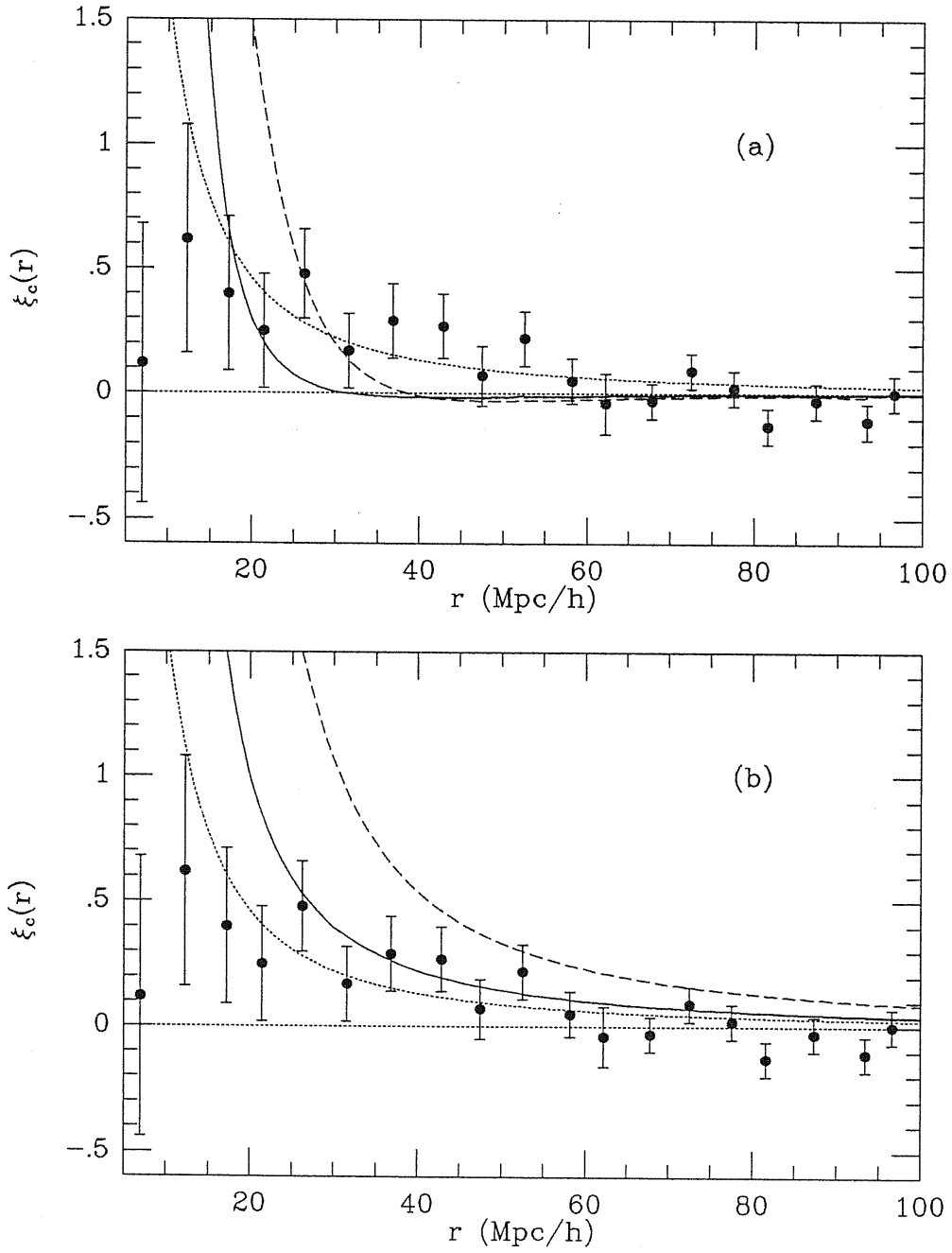

Figure 4.5: *Rich–cluster 2–point correlation function in the case of θ-threshold for (a) CDM spectrum, and for (b) scale-free spectrum with spectral index $n = -1.2$. The solid lines correspond to the choice of the top–hat window with smoothing radius $R = 9h^{-1}Mpc$ [the resulting galaxy bias factor is $b_g = 1.06$ for both (a) and (b) cases] and the dashed line to the choice of the Gaussian window with smoothing radius $R = 7.5h^{-1}Mpc$ [also in this case the resulting galaxy bias factor is $b_g = 1.06$ for both (a) and (b) cases] The observational data refer to the 2–point cluster correlation function obtained by Sutherland & Efstathiou [188] from the analysis of Geller & Huchra's [85] deep redshift survey, while the dotted curve represents the best fit power law $\xi_c(r) = (r_{o,c}/r)^{1.8}$, with $r_{o,c} = 13h^{-1}Mpc$.*

4.3.1 Cluster correlations with the erfc-threshold

In order to evaluate the 2-point cluster correlation function from eq. (4.14), let us consider the quantities

$$\Pi^{(1)}_{\delta_c,\mathrm{R}} = \frac{1}{\sqrt{2\pi}} \sum_{L=0}^{\infty} \left(\frac{\Delta^2}{2\sigma_\mathrm{R}^2}\right)^L \frac{1}{L!}\, a^{(0)}_{2L}\left(\frac{\delta_c}{\sqrt{2}\sigma_\mathrm{R}}\right) \tag{4.15}$$

and

$$\Pi^{(2)}_{\delta_c,\mathrm{R}}(x_1,x_2) = \frac{1}{2\pi} \sum_{L=0}^{\infty} \Bigg[\sum_{m_{2,[r_2]}} \left(\frac{\Delta^2}{2\sigma_\mathrm{R}^2}\right)^{m_{2;1,1}+m_{2;2,2}} \frac{1}{m_{2;1,1}!\, m_{2;2,2}!} \times$$

$$\times \left(\frac{\xi^{(2)}_\mathrm{R}(x_1,x_2)}{2\sigma_\mathrm{R}^2}\right)^{m_{2;1,2}+m_{2;1,2}} \frac{1}{m_{2;1,2}!\, m_{2;1,2}!}\Bigg] \times a^{(0)}_{\mathrm{m}(1)}\left(\frac{\delta_c}{\sqrt{2}\sigma_\mathrm{R}}\right) a^{(0)}_{\mathrm{m}(2)}\left(\frac{\delta_c}{\sqrt{2}\sigma_\mathrm{R}}\right), \tag{4.16}$$

which can be deduced from eqs. (3.15) and (3.9), respectively, evaluated for the *erfc*-threshold, and taking a Gaussian background. In eq. (4.16) the sum over the indices $m_{n,[r_n]}$ has been written explicitly. According to the properties of such indices, we have

$$m_{2;1,1} + m_{2;1,2} + m_{2;2,1} + m_{2;2,2} = m_2 = \frac{L}{2}, \tag{4.17}$$

while, according to eq. (3.14), it is

$$\begin{aligned} \mathrm{m}(1) &= 2m_{2;1,1} + m_{2;1,2} + m_{2;2,1} \\ \mathrm{m}(2) &= 2m_{2;2,2} + m_{2;1,2} + m_{2;2,1} \end{aligned} \tag{4.18}$$

Following eq. (4.14), it is now easy to obtain the 2-point correlation function for the *erfc-threshold*. From a numerical evaluation of the eqs. (4.15) and (4.16), we obtain the shapes for $\xi^{(2)}_{\delta_c,\mathrm{R}}(r)$ reported in Figure 4.7*a* (for a canonical CDM spectrum) and in Figure 4.7*b* (for a scale–free spectrum with $n = -1.2$). A comparison with the data and with the *best–fit* power law shows that in the CDM model the correlation is too steep for small separations, while a better agreement is reached with the scale–free spectrum. However, in the *θ–threshold* limit there are some problems for both spectra in reproducing the small scale behaviour of the cluster 2-point function. As shown in Figure 3, the situation is even worse assuming a Gaussian window, which increases the correlation strength on small scales; for this reason, in the following we will take the top–hat function as the window acting on the background field. Some marginal improvement is however obtained taking with $\Delta = 0.4$ in the *erfc*-threshold, which has the effect of reducing the excess of correlation for small separation (see Figure 4.7). Further improvement can be obtained with larger values of the parameter Δ, the only problem in this case being the difficulty in getting numerical convergence of the series (4.15) and (4.16) at small separations.

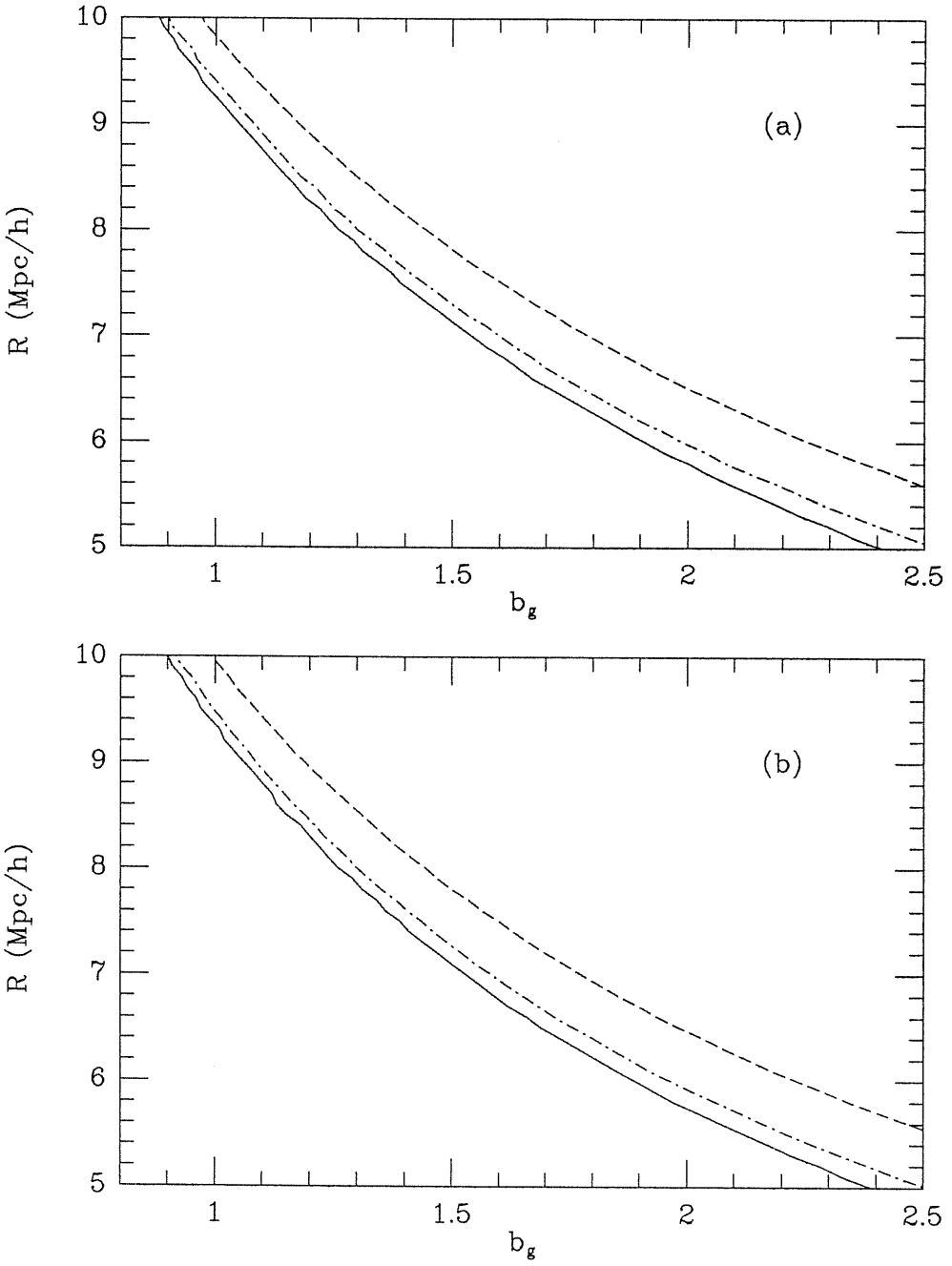

Figure 4.6: *The relation between the smoothing radius R and the galaxy bias factor b_g, in the case of erfc-threshold for (a) CDM spectrum and for (b) scale-free spectrum with spectral index $n = -1.2$. The solid line corresponds to $\Delta = 0$ (θ-threshold), the dot–dashed line to $\Delta = 0.2$, and the dashed line to $\Delta = 0.4$.*

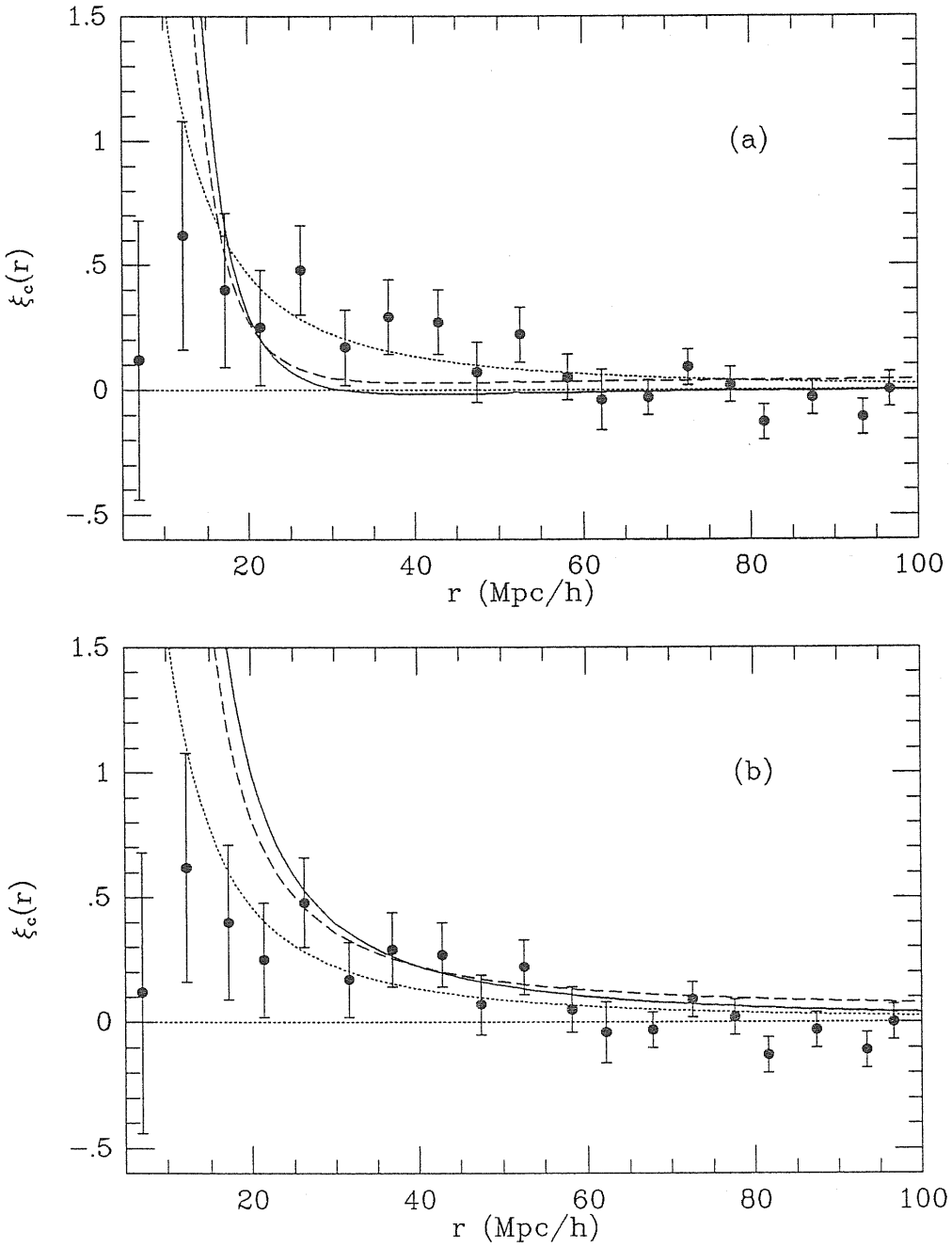

Figure 4.7: *Rich-cluster 2-point correlation function in the case of erfc-threshold for (a) CDM spectrum, and for (b) scale-free spectrum with spectral index* $n = -1.2$. *The smoothing radius is* $R = 9h^{-1}Mpc$ *in all cases. The solid lines correspond to* $\Delta = 0$ *[the resulting galaxy bias factor is* $b_g = 1.06$ *for both (a) and (b) cases] and the dashed line to* $\Delta = 0.4$ *[with* $b_g = 1.18$ *for (a) and* $b_g = 1.20$ *for (b)].*

4.3.2 Cluster correlations with the Gaussian threshold

Following the same approach as in the case of the *erfc*-threshold, let us evaluate the fraction of volume occupied by objects

$$\Pi^{(1)}_{\delta_c,\mathrm{R}} = \frac{\Sigma}{\sigma_{\mathrm{R}}}\sum_{L=0}^{\infty}\left(\frac{\Sigma^2}{2\sigma^2_{\mathrm{R}}}\right)^L \frac{1}{L!}\, a^{(1)}_{2\mathrm{L}}\left(\frac{\kappa\delta_c}{\sqrt{2}\sigma_{\mathrm{R}}}\right), \tag{4.19}$$

and the 2-point joint probability

$$\Pi^{(2)}_{\delta_c,\mathrm{R}}(x_1,x_2) = \frac{\Sigma}{\sigma_{\mathrm{R}}}\sum_{L=0}^{\infty}\Big[\sum_{m_{2,[r_2]}}\left(\frac{\Sigma^2}{2\sigma^2_{\mathrm{R}}}\right)^{m_{2;1,1}+m_{2;2,2}} \frac{1}{m_{2;1,1}!\, m_{2;2,2}!}\times$$

$$\times\left(\frac{\xi^{(2)}_{\mathrm{R}}(x_1,x_2)}{2\sigma^2_{\mathrm{R}}}\right)^{m_{2;1,2}+m_{2;1,2}} \frac{1}{m_{2;1,2}!\, m_{2;1,2}!}\Big] \times a^{(1)}_{\mathrm{m}(1)}\left(\frac{\kappa\delta_c}{\sqrt{2}\sigma_{\mathrm{R}}}\right) a^{(1)}_{\mathrm{m}(2)}\left(\frac{\kappa\delta_c}{\sqrt{2}\sigma_{\mathrm{R}}}\right). \tag{4.20}$$

After numerical calculation, we get the shape of the 2-point correlation function. This is represented in Figures 4.9*a* and 4.9*b* (together with the θ–bias outputs), respectively for CDM and scale–free spectra, with the value $\Sigma = 0.12$ for the selection parameter. Taking too large fluctuations out by means of the *Gaussian* threshold results in an even greater reduction of the value of the 2–point function at small distances. However, in this case too CDM model appears to be inadequate to describe the observed *cluster* 2-point correlation function, which is positive up to $r \sim 60\, h^{-1}Mpc$. A significant improvement is obtained with the *scale-free* spectrum, which provides a quite good fit to the data, (see Figure 4.9*b*). A further approach to the power–law shape is obtainable for smaller values of Σ, which however leads to the undesirable case $b_g < 1$.

4.3.3 Discussion of the results

By comparing our general biased models and observational data on the 2-point correlation function of rich Abell clusters, we obtain the two following results.

First, the CDM model for the background spectrum seems to have trouble in reproducing the behaviour of the data (see Figures 4.7*a* and 4.9*a*). In fact, the predicted 2–point cluster function is too steep and rapidly goes nearly to zero for $r \sim 30\, h^{-1}Mpc$, while the data show no significant anticorrelation up to $r \sim 60\, h^{-1}Mpc$. This should not surprise us, as it is a direct effect of the non–scale-invariance of the CDM spectrum, as shown in §2.4. Because the correlation functions for the CDM particles steepen with time, the shape of the spectrum is fixed by requiring that its slope *on galaxy clustering scales* at the present time reproduce the observed shape of the 2–point *galaxy* function. As a consequence, the clustering scale of rich clusters will be characterized by an effective spectral index $n_{eff} = 1$, which is however

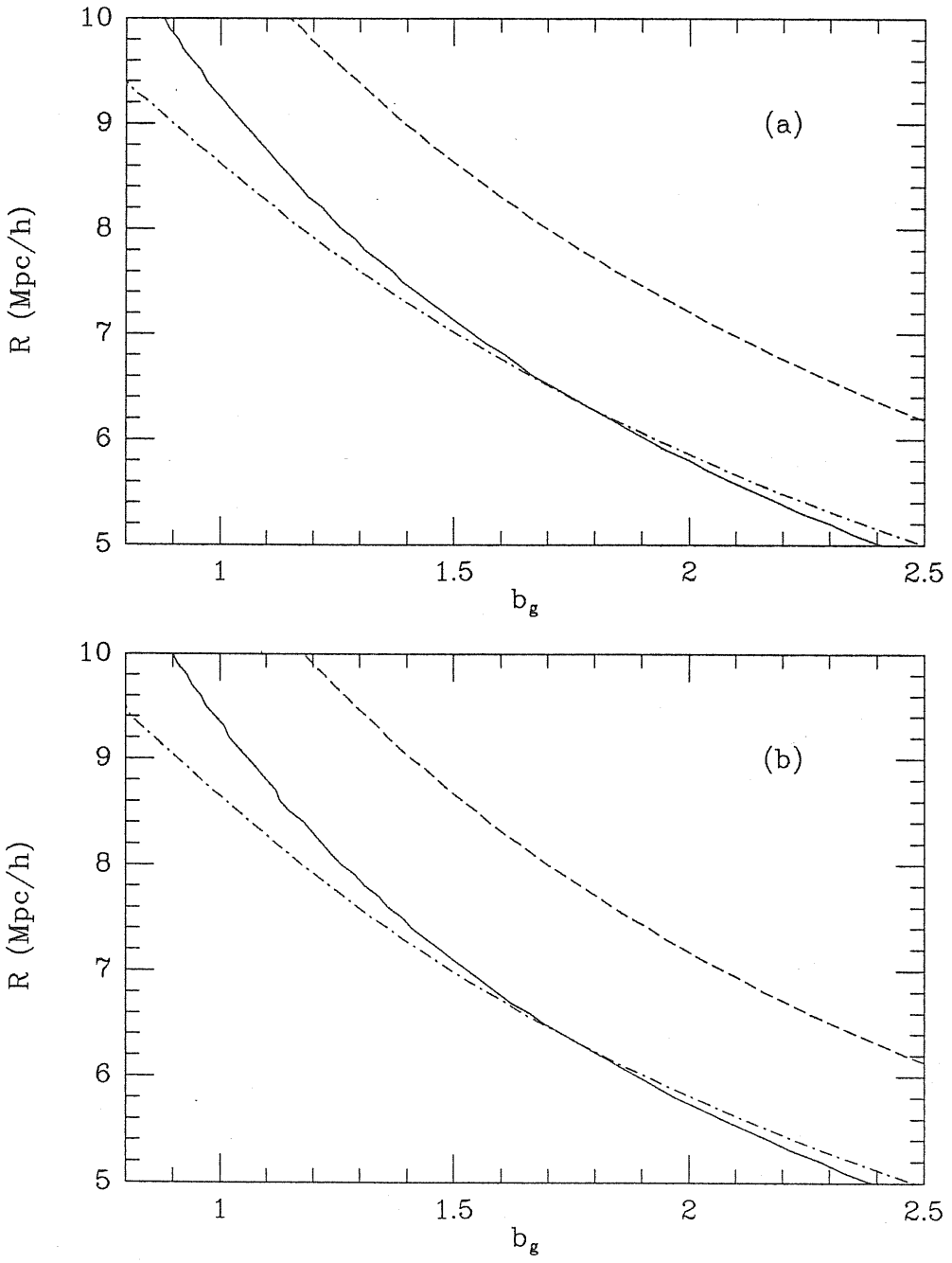

Figure 4.8: *Relation between the smoothing radius R and the galaxy bias factor b_g, in the case of Gaussian-threshold, for (a) CDM spectrum, and for (b) scale–free spectrum. The solid line corresponds to the θ-threshold case, the dot–dashed line to $\Sigma = 0.1$, and the dashed line to $\Sigma = 0.3$.*

unable to reproduce the observed power–law for the rich–cluster 2-point function. On the other hand, a *scale–free* spectrum with spectral index $n = -1.2$ (independent of scale) avoids these difficulties. In fact, as shown in Figures 4.7*b* and 4.9*b*, the resulting cluster 2-point function turns out to reproduce quite well the smooth behaviour of the power law fit up to small separations. Strictly speaking, even though the scale-free spectrum provides a fairly good fit, the large uncertainties in the data do not permit us to rule out any dependence of n on the scale. Indeed, no significant modifications of the 2-point function occurs for $-1.5 \lesssim n \lesssim -1$.

Second, the introduction of non–sharp thresholds does give substantial modifications to the 2-point correlation function. This shows how misleading it can be to ignore physical effects in the formation of cosmic structures. Taking tentatively into account non–sphericity and merging by means of the *erfc* and *Gaussian* threshold respectively leads to a systematically better agreement with the data. In particular, the excess of correlation strength on small scales turns out to be sensitive by an amount which depends on the threshold parameters. Indeed, a good fit is obtained by taking the *Gaussian–threshold* with selection parameter $\Sigma = 0.12$ (see Figure 4.9).

In our opinion, the outputs of the general biased models described in this chapter can be useful to parametrize non–linear dynamics relevant to structure formation and to investigate the influence on the large–scale distribution of objects. Our method replaces a fully dynamical treatment which should instead fix the values of those parameters which we actually leave free and to be compared with observational outputs. On the other hand, there can be little doubt that an improvement on the observational side would also help to clarify the situation.

However, already in the present context, we think that one conclusion can be reached. Although the fluctuation spectrum is expected to change its slope between galaxy and cluster scales (as in the CDM model), nevertheless non–linear dynamics could offset the difference and produce 2-point functions of similar slopes on both scales. Our investigation, however, suggests that no *reasonable* non–linear effects can cancel features which are rooted into the primeval fluctuation field. This realization avoids the introduction of unpleasant *fine–tuning* requirements to obtain the same correlation–function slope in both galaxy and cluster regimes. Let us suppose however that non–linear dynamics cancels primordial spectral features. In this case no primeval features can be inferred from observations and no bias is warranted. Alternatively, if a primeval mark is imprinted on the observed clustering features, one would be compelled to conclude that observations suggest a virtually *scale–free* post–recombination spectrum.

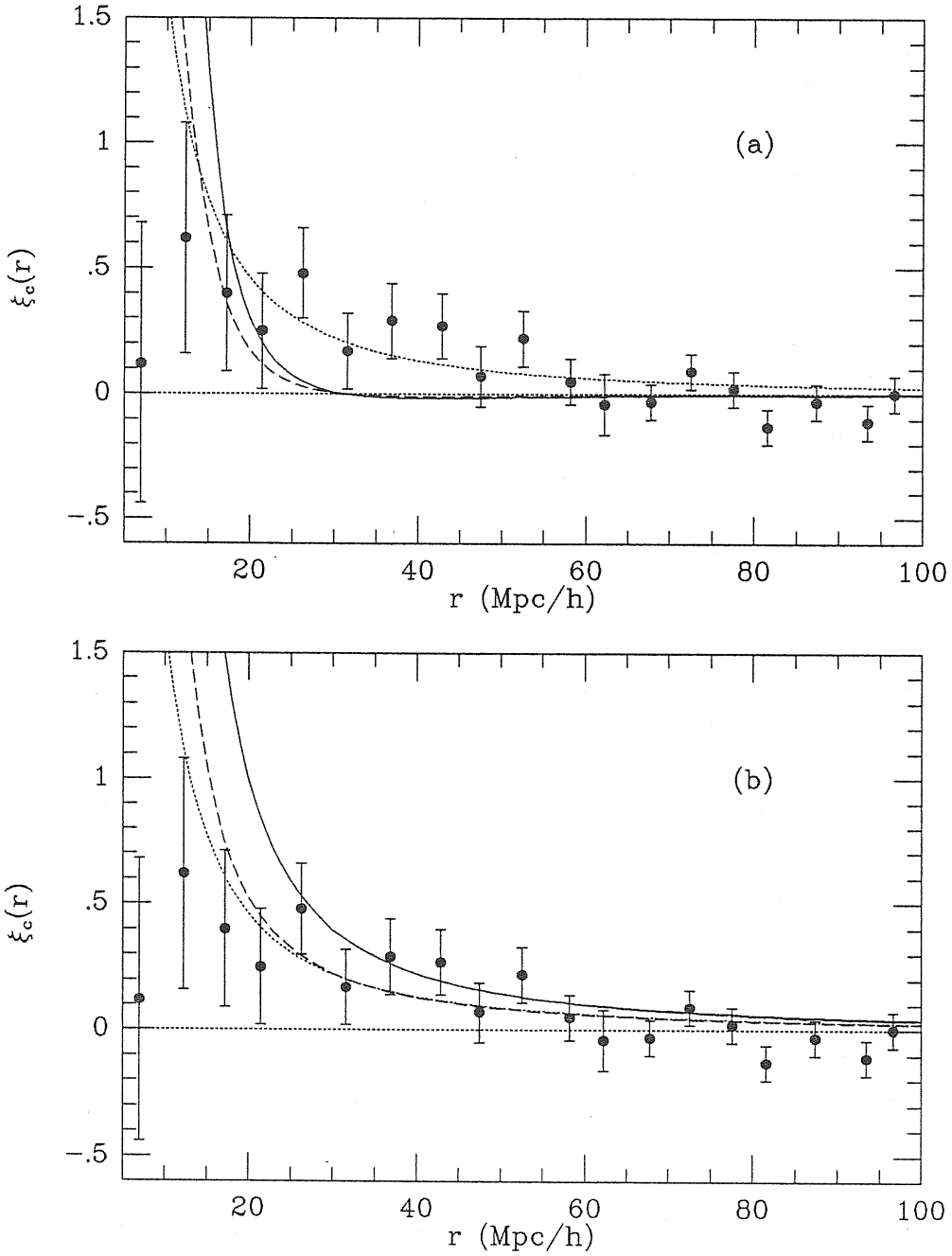

Figure 4.9: *Rich-cluster 2-point correlation function for (a) CDM spectrum, and for (b) scale-free spectrum with spectral index* $n = -1.2$. *The smoothing radius is* $R = 9h^{-1}Mpc$ *in all cases. The solid line corresponds to the* θ*-threshold case and the dashed line to the Gaussian threshold with* $\Sigma = 0.12$ *[the corresponding galaxy bias factor is* $b_g = 1.0$ *for both (a) and (b) cases].*

The content of §4.2 is a part of a paper already published in the *Astrophysical Journal* [31], and it has been presented at the *Durham Symposium on the Epoch of Galaxy Formation* [24]. Moreover, the content of §4.3 is included in a second paper, that is in press in *Astronomy & Astrophysics* [29].

Chapter 5

Galaxy halos and matter statistics

The statistical analysis of homogeneous samples of galaxies and galaxy systems furnishes a precise description of the clustering pattern of luminous matter on large scales (see Chapter 1). There exists however several indications, both of observational and theoretical origin, that a great amount of dark matter (DM) should exist, that is not traced by the distribution of observable objects. In this frame, the *biased theories* for the formation of cosmic structures, that we formulated in Chapter 4, constitute a statistical tool for relating the different correlation properties of background matter and galaxy distributions. However, up to now the lack of a method for investigating the DM clustering pattern made no possible a direct test of a possible segregation between galaxies and background matter.

In this chapter we describe a new method to explore matter correlation properties at galaxy scales. In particular, we investigate the statistics of halo matter surrounding galaxies rather than studying galaxy number counts, as is usually done in the analyses of homogeneous samples. It should be pointed out that the features of mass distribution in *individual* galaxies follow from rotation curves, while the *statistical* properties of matter distribution are derived from extended sets of objects with different radii, peripheral velocities, luminosities. The latter quantities are used to formulate a statistics for the expected density enhancements within given distances from galactic centers.

5.1 How to investigate the matter distribution

If we require that the clustering pattern of galaxies, as inferred from their observed distribution, be stable over a Hubble time (H_o^{-1}), then we conclude that large-scale peculiar motions trace the distribution of matter in the Universe [72]. Quite similarly, circular velocities in spiral galaxies trace the galaxies' internal mass distribution.

Though on different scales, both sorts of motion highlight some degree of clumpiness, or clustering, in the distribution of matter.

The analysis of peculiar velocity fields over very large scales, $R \sim 100\,Mpc$ [1], leads to precise predictions on the amplitude of the mass excess $\delta M/M$ associated to a given mass concentration [17]. Peculiar velocities are in general obtainable from redshift surveys, where they make the galaxy clustering pattern appear elongated along the line of sight [87]. Peebles [155] extended such arguments down to the scale, $R \sim 1\,Mpc$, typical of close galaxy pairs. If the mass distribution within the pair is modeled as the linear sum of spherical halos of radius R and mass $\delta M_{\rm R}$ centered on each galaxy, and the *r.m.s.* peculiar velocity dispersion within the pair is $\sigma_v(R)$, then the mass excess is $\delta M_{\rm R} \simeq \sigma_v(R)^2\, R/G$. Since the mean mass density in a FRW Universe is $\rho = 3H_o^2\Omega_o/8\pi G$, the associated mass fluctuation is

$$\frac{\delta M_{\rm R}}{M_{\rm R}} \;=\; \frac{2}{\Omega_o}\left(\frac{\sigma_v(R)}{H_o R}\right)^2 \tag{5.1}$$

[$M_{\rm R} = (4/3\pi)\,\rho\, R^3$ is the mean mass within R].

In the same paper, Peebles stressed also the importance of comparing the mass fluctuations, $\delta M_{\rm R}/M_{\rm R}$, with the galaxy number fluctuations, $\delta N_{\rm R}/N_{\rm R}$, which represents the mean number of galaxies in excess of random within a distance R of a galaxy, and is given by

$$\frac{\delta N_{\rm R}}{N_{\rm R}} \;=\; \frac{3}{4\,\pi\, R^3}\int_0^R \xi_{gg}(r)\; d^3r \;=\; \frac{3}{3-\gamma}\left(\frac{r_{o,gg}}{R}\right)^{\gamma}. \tag{5.2}$$

In eq. (5.2) we indicated with ξ_{gg} the two-point galaxy correlation function measured from galaxy number counts and, as already seen in Chapter 1, on scales 0.2–20 Mpc is modeled as a power law, $\xi_{gg} = (r_{o,gg}/r)^{\gamma}$ with $\gamma = 1.77 \pm 0.03$ and $r_{o,gg} \simeq 10^{+4}_{-2}\,Mpc$. On the other hand, the analysis of galaxy peculiar motions in the CfA1 redshift survey leds Davis & Peebles to detect a pair velocity dispersion $\sigma_v(r) = (310 \pm 35)\,(r/Mpc)^{0.13\pm0.04}\; km\, s^{-1}$ [52]. Then, we see fron eq. (5.1) that $\delta M/M$ and $\delta N/N$ both vary with r in about the same way, as $r^{-1.76\pm0.04}$, supporting the hypothesis of a stable clustering pattern. From this similarity in the r dependences, Peebles [155] argued that "whatever gathered galaxies together to make the present clustering pattern gathered mass in the same proportion".

If mass and number counts fluctuations do coincide, so that

$$\delta N/N \;=\; \delta M/M\,, \tag{5.3}$$

then from eqs. (5.1) and (5.2) and related quantities one estimates the galaxy contribution to the mean mass density to be $0.3 \lesssim \Omega_o \lesssim 0.6$ [155]. On the other hand, the

[1] In the following of this chapter we use a value $H_o = 50\; km\; s^{-1} Mpc^{-1}$ for the Hubble constant.

already discussed observational evidence for different clustering properties of galaxies and clusters of galaxies [118,23,8], as well as the need for reconciling the observed velocity dispersion within binary galaxies with the theoretical prejudice for $\Omega_o = 1$, motivate the possibility that

$$\delta N/N \; = \; b \, \delta M/M \, , \tag{5.4}$$

where $b > 1$ is the biasing parameter (see also §3.1). Thus, the galaxy contribution to the mean mass density can still be reconciled with a flat Universe ($\Omega_o = 1$), provided that $b \simeq$ 2-3. In general, for a *biased* distribution of galaxies eq. (5.4) gives the bias parameter b once a particular value of Ω_o is assumed.

If the Universe is dominated by dark matter on the larger scales, then, on the scale of galaxies, continuity arguments invite us to consider only their dark mass components rather than their overall mass distribution in order to meaningfully compare the clustering properties of matter at small and large scales. To this purpose we use the rotation curves of spiral galaxies instead of the *r.m.s.* velocity dispersion within galaxy pairs. In fact, although both galaxies within pairs and the stars within galaxies (from which rotation curves come) behave as equivalent test particles in the background gravitational field, the relevant radial distance scales are substantially smaller for the stars ($R \sim$ 5-50 kpc) than for binary galaxies ($R \sim 500\, kpc$-1 Mpc), so rotation curves provide a deeper probe into the distribution of matter than velocity dispersion measurements.

In order to study the background (dark) matter statistics starting from observed galaxy rotation velocities, a proper general technique for decomposing rotation curves into the contributions of luminous and dark components is required. By applying such a technique to a sample of galaxies spanning a broad range of luminosities, the knowledge of the physical parameters of DM in the halos would permit to investigate the correlation properties of dark matter surrounding galaxies. Until quite recently, however, a general mass decomposition technique was not available, so *direct* investigations of background statistics on galaxy scales could not be attempted. A suitable method, which extracts the DM content of spiral galaxies at the optical disk radius from the profiles of rotation curves, was recently devised by Persic & Salucci [158,161] and constitute the key starting point for the present study.

In doing such analysis, we take a sample of 58 spiral galaxies [159,160] (hereafter PS90 sample). These are all non–local galaxies for which both good (blue) photometry (*r.m.s.* errors $< 0.05\, mag$) and high–quality, extended (out to $R \geq 0.8\, R_{opt}$) rotation curves were available in the literature by the end of 1988. They span the (absolute blue) magnitude range from -17.5 up to -23.2. Disk radii range between about 3 and 55 kpc. Peripheral velocities range between about 120 and 400 $km\ s^{-1}$. They are of morphological types Sb through Sc, apart from two Sa and one Sab cases

(see Table 5.1).

5.2 Dark matter in spiral galaxies

Dark matter has long been recognized as a fundamental component of the internal structure of galaxies [70]. The overall matter distribution, as revealed dynamically by observed rotation curves, is strikingly different from the distribution of luminous matter in the optical disk region [175] and extends out to large radii where no velocity falloff is observed [37,7,40,41]. Therefore huge amounts of matter, not traced by light, dominate the overall dynamics and structure of galaxies. One may then naturally expect a link between internal galaxy structure and background matter statistics.

In spiral galaxies, the optical disk radius, R_{opt}, is both the only observable lengthscale of their internal structure (R_{opt} is ~ 3 times the scale of the exponential light distribution [77,200]) and the innermost radius where DM affects strongly and systematically the observed dynamics [175,158]. For this reason, R_{opt} is the appropriate reference radius suitable for studying the statistical properties of DM at one same radius (in galaxy normalized units) for all galaxies.

Let $V_{opt} = V(R_{opt})$ be the value of the observed velocity at R_{opt}, and $V_{h,opt}$ the halo component of V_{opt}; let also M_{disk} and M_{halo} be the disk and halo masses evaluated at R_{opt}. Then, from the relation

$$V^2_{h,opt} = V^2_{opt} \frac{M_{halo}}{M_{disk} + M_{halo}}, \tag{5.5}$$

$V_{h,opt}$ is obtainable as soon as the mass ratio at the right hand side of eq. (5.5) is known. According to Persic & Salucci [158,159] the disk–to–total mass ratio in spiral galaxies at the optical disk radius is directly obtainable from the profiles of optical rotation curves. They use a two–component mass model including a spherical dark halo and a luminous thin disk with exponential surface brightness distribution $I(R) = I_o\, e^{-R/R_D}$, while no halo matter density profile is assumed. According to such mass–decomposition technique for ordinary spirals, the disk–to–total mass ratio at the optical radius is

$$\frac{M_{disk}}{M_{disk} + M_{halo}} = \frac{0.8 - \frac{d\ logV}{d\ logR}|_{R_{opt}}}{0.1\ \frac{d\ logV}{d\ logR}|_{R_{opt}} + 1.1} \tag{5.6}$$

(see Appendix B). Therefore $V_{h,opt}$ is obtainable from the observable quantities V_{opt} and its logarithmic derivative $\frac{d\ logV}{d\ logR}|_{R_{opt}}$. (In this section velocities V and distances R are expressed in $km\ s^{-1}$ and kpc respectively, unless otherwise stated.)

Based on eq. (5.6), an analysis of available data shows a number of systematic properties of dark matter (hereafter DM) in spiral galaxies: *a)* the disk kinematics

of fainter galaxies shows steeper velocity gradients ($\frac{\partial logV}{\partial logR}|_{R_{opt}} \sim 0.6$) hence is mostly halo–dominated ($M_{disk}/M_{tot} \sim 0.2$), while in brighter galaxies (whereby $\frac{\partial logV}{\partial logR}|_{R_{opt}} \sim -0.05$) the kinematics is mostly disk–dominated ($M_{disk}/M_{tot} \sim 0.8$). Between these extremes there is a continuous distribution of M_{disk}/M_{tot} values; and *b)* the M_{disk}/M_{tot} distribution, owing to the correlation between galaxy luminosity and $\frac{\partial logV}{\partial logR}|_{R_{opt}}$, maps into the luminosity sequence of galaxies [158].

Let us now consider the condition of centrifugal equilibrium for the halo at R_{opt}, *i.e.* $M_{halo} = G^{-1} V_{opt}^2 R_{opt}$. It implies that the volume–averaged density in the spherical halo is

$$\frac{\bar{\rho}_{h,opt}}{g\ cm^{-3}} = 4 \times 10^{-27} \left[\frac{(V_{h,opt}/km\ s^{-1})}{(R_{opt}/kpc)}\right]^2 \tag{5.7}$$

Owing to eqs. (5.5) and (5.6), $\bar{\rho}_{h,opt}$ is therefore directly obtainable from velocity data.

According to the Friedman equations, the critical density of the Universe reads

$$\frac{\rho_c}{(g\ cm^{-3})} = 1.9 \times 10^{-27} \left(\frac{H_o}{km\ s^{-1} kpc^{-1}}\right)^2 . \tag{5.8}$$

Dividing eq. (5.7) by eq. (5.8), we obtain

$$\frac{\bar{\rho}_{h,opt}}{\rho} = \left(\frac{\tilde{R}_o}{R_{opt}}\right)^2 \tag{5.9}$$

where $\rho = \Omega_o\, \rho_c$ is the actual density of the Universe. In eq. (5.9)

$$\begin{aligned} \left(\frac{\tilde{R}_o}{Mpc}\right) &= (2.1\, \Omega_o^{-1})^{1/2} \frac{(V_{h,opt}/km\ s^{-1})}{(H_o/km\ s^{-1} Mpc^{-1})} = \\ &= 7 \left[\left(\frac{V_{h,opt}}{250\ km\ s^{-1}}\right) \Omega_o^{-1/2} h_{50}^{-1}\right] . \end{aligned} \tag{5.10}$$

Eqs. (5.9) and (5.10) are true for each individual galaxy. If no statistical correlation existed between R_{opt} and $V_{h,opt}$, eq. (5.9) would define the correlation between $\bar{\rho}_{h,opt}$ and R_{opt} (correlation length $\tilde{R}_o$, given by eq. (5.10) with $V_{h,opt}$ replaced with $< V_{h,opt} >$, and slope $\gamma = 2$). From Table 5.1 and eq. (5.5), however, we test that a correlation between $V_{h,opt}$ and R_{opt} does exist (see also Figure 5.3), so that

$$\frac{\bar{\rho}_{h,opt}}{\rho} = \left(\frac{R_o}{R_{opt}}\right)^{\gamma} \tag{5.11}$$

with $R_o \sim \tilde{R}_o$ and $\gamma < 2$.

A procedure of linear regression analysis of the PS90 sample (see Table 5.1) through eqs. (5.5), (5.6) and (5.11) yields $\gamma = 1.76 \pm 0.12$ and $R_o = (8.5 \pm 1.5)\ Mpc$

in the 3-50 *kpc* distance range (see Figure 5.1), quite in agreement with the above arguments. The match of γ with the canonical value of the two-point galaxy–galaxy correlation function slope is a consequence of the underlying link between eq. (5.11) and the clustering properties of the background matter.

Table 5.1
The PS90 sample of spiral galaxy rotation curves

Object	M_B	R_{opt}	V_{opt}	$\frac{M_{disk}}{M_{tot}}$	$log\bar{\rho}_{h,opt}$	Object	M_B	R_{opt}	V_{opt}	$\frac{M_{disk}}{M_{tot}}$	$log\bar{\rho}_{h,opt}$
N 488	-22.52	33.3	379	0.52	-24.51	N 4682	-20.85	15.4	179	0.49	-24.47
N 753	-22.60	20.8	209	0.66	-24.77	N 4800	-20.00	4.2	165	0.56	-23.48
N 1035	-19.69	7.4	138	0.31	-23.92	N 5033	-21.30	38.4	219	0.59	-25.17
N 1085	-22.55	32.0	310	0.70	-24.86	N 5055	-21.55	18.9	200	0.71	-24.80
N 1300	-21.47	20.8	200	0.71	-24.88	N 5290	-21.51	17.6	220	0.62	-24.53
N 1325	-20.87	18.2	209	0.27	-24.32	N 5371	-22.60	32.6	240	0.67	-25.06
N 1417	-22.28	25.6	308	0.50	-24.45	N 5383	-22.50	19.2	209	0.77	-24.88
N 1421	-20.80	26.6	225	0.30	-24.61	N 5426	-21.24	20.2	157	0.71	-25.07
N 1620	-21.90	28.5	265	0.36	-24.56	N 5673	-20.50	11.2	125	0.50	-24.50
N 2336	-22.50	50.6	252	0.69	-25.41	N 5905	-21.84	52.8	250	0.58	-25.33
N 2708	-20.60	13.8	283	0.21	-23.78	N 5908	-22.00	29.8	350	0.68	-24.65
N 2715	-21.21	28.5	177	0.34	-24.89	N 7083	-22.40	38.4	223	0.67	-25.26
N 2742	-20.54	12.2	190	0.34	-24.10	N 7171	-21.25	23.7	227	0.58	-24.72
N 2815	-22.00	29.4	286	0.65	-24.78	N 7331	-22.40	33.9	226	0.66	-25.12
N 2997	-21.19	21.1	160	0.71	-25.09	N 7531	-21.14	12.2	180	0.71	-24.51
N 2998	-22.00	26.6	214	0.58	-24.86	N 7537	-21.23	11.8	137	0.72	-24.72
N 3054	-21.63	17.3	239	0.50	-24.32	N 7591	-21.21	20.5	195	0.71	-24.89
N 3145	-22.58	35.8	276	0.64	-24.97	N 7606	-22.54	26.6	257	0.84	-25.13
N 3198	-20.60	13.8	158	0.56	-24.53	N 7631	-21.17	17.9	208	0.47	-24.45
N 3200	-22.87	47.4	288	0.58	-25.12	N 7664	-21.60	11.2	183	0.71	-24.42
N 3223	-22.64	37.1	255	0.69	-25.14	N 7723	-21.57	15.4	209	0.71	-24.58
N 3672	-21.75	19.8	190	0.65	-24.80	I 467	-20.55	15.0	143	0.51	-24.66
N 3963	-22.37	23.7	177	0.69	-25.07	U 807	-21.80	37.1	211	0.71	-25.34
N 3992	-21.70	28.2	277	0.61	-24.73	U 2259	-17.50	5.1	89	0.23	-23.94
N 4062	-19.50	13.1	201	0.21	-24.04	U 4375	-20.02	10.6	189	0.57	-24.16
N 4254	-21.51	14.1	204	0.45	-24.24	U11810	-21.10	28.2	182	0.58	-25.06
N 4321	-21.53	22.1	227	0.50	-24.58	U12417	-20.05	11.2	165	0.14	-24.02
N 4565	-23.20	42.2	254	0.71	-25.29	U12810	-22.40	35.8	225	0.62	-25.13
N 4605	-18.59	3.2	95	0.08	-23.39	WR 66	-20.77	25.6	171	0.62	-25.08

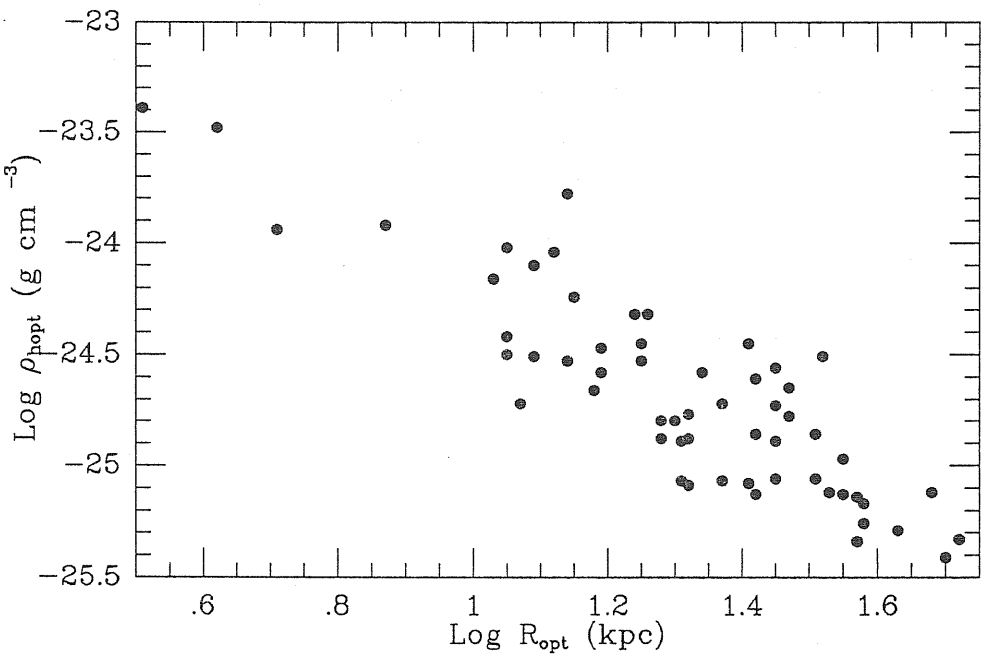

Figure 5.1: *The mean halo matter density at the optical disk radius, $\bar{\rho}_{h,opt}$ as a function of the optical disk radius, R_{opt}, for the PS90 sample of 58 Sb–Sc spiral galaxies with extended rotation curves.*

The comparison between eq. (5.11) and the two-point galaxy–galaxy correlation function should be made with some caution, as the latter is known over the significantly different $20\,kpc$–$10\,Mpc$ distance range [97]. Therefore, although we can obtain a valid measure of the correlation function at the physically meaningful radius R_{opt}, we need to sample the density–radius correlation farther out in the halos, *i.e.* at radii $R \gg R_{opt}$, in order to extend its radial overlap with the galaxy function.

To this purpose let us *define* an effective halo radius, R_h, as the radius encompassing an amount of DM η times greater than M_{disk}. Consequently the mean halo density at R_h is $\bar{\rho}_h = \eta M_{disk}/(\frac{4}{3}\pi R_h^3)$. Observed rotation curves are nearly flat for $R > R_{opt}$, with a value $\sim V_{opt}$ [37,15]. Therefore, the centrifugal equilibrium condition at R_h reads

$$\bar{\rho}_h = 4 \times 10^{-27} \frac{V_{opt}^2}{R_h^2}. \tag{5.12}$$

The halo radius, appearing in eq. (5.12), is not directly observable. However, by our definition of R_h and by eq. (5.6), it can be related to the observable quantities R_{opt} and $\frac{dlogV}{dlogR}|_{R_{opt}}$, being

$$R_h = \eta\, R_{opt}\left(\frac{0.8 - \frac{d\ logV}{d\ logR}|_{R_{opt}}}{0.1\ \frac{d\ logV}{d\ logR}|_{R_{opt}} + 1.1}\right). \tag{5.13}$$

If one takes $\eta = const$ for all galaxies, it is the variation of M_{disk}/M_{halo} with luminosity

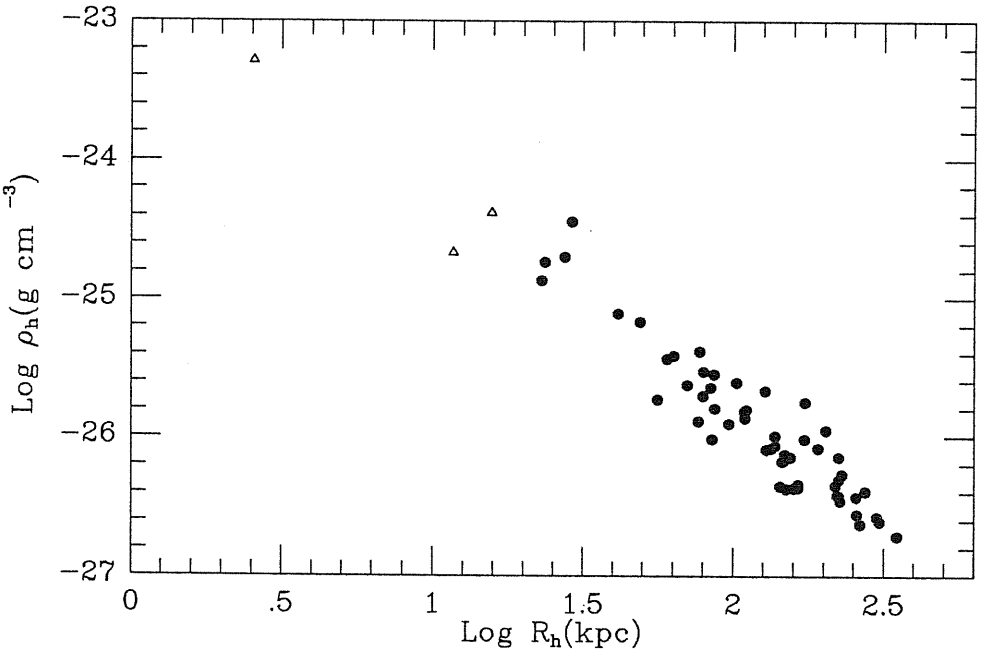

Figure 5.2: *The mean halo matter density, $\bar{\rho}_h$, as a function of the effective halo radius, R_h (see text), for the same sample as in Figure 1. The three empty triangles represent the galaxies NGC 4605, UGC 2259, and UGC 12417, which are not considered in the moment analysis as they fall in a non–contiguous and insufficiently populated radial bin.*

which induces a range of R_h. Here again, should the variations of V_{opt} and R_h be statistically independent, in a sample of galaxies one would find $\bar{\rho}_h/\rho = (\tilde{R}_o/R_h)^2$ with $\tilde{R}_o \sim 7\,Mpc$ for $\Omega_o = 1$, $h_{50} = 1$, and $V_{opt} \sim 250\,km\,s^{-1}$. However, arguments similar to the ones made for the R_{opt} case lead us to expect a softer slope, $\gamma < 2$. A rough estimate, neglecting the luminosity dependence of $M_{disk}/(M_{disk} + M_{halo})$ (which would increase γ) and using the V_{opt}-R_{opt} correlation given by Rubin *et al.* [174] alongside eqs. (5.12) and (5.13), yields

$$\frac{\bar{\rho}_h}{\rho} = \left(\frac{R_o}{R_h}\right)^{\gamma} \tag{5.14}$$

with $\gamma \simeq 1.5$ and $R_o \simeq 10\ Mpc$ for $\Omega_o = 1$ and $h_{50} = 1$ [for $\eta = 10$, the correlation between V_{opt} and R_h, inserted in eq. (5.14), leads to values for γ and r_o which are consistent with the above estimates]. We remark that these estimates of the scale R_o are compatible with the actual value appearing in eq. (5.11). This circumstance hints that quantities relevant to the DM distribution on intermediate scales can be directly estimated from observed galaxy kinematics.

In what follows we take $\eta = 10$ [20,57]. We have verified that different choices for η reflect very mildly on R_o, and only to the extent that $\gamma \neq 2$, according to $R_o \propto \eta^{\frac{\gamma-2}{\gamma}}$ [see eqs. (5.12), (5.13) and (5.14)]; no variation of γ is induced if η is chosen to be uncorrelated with luminosity. Then we work out the extended halo

parameters for the PS90 sample. By using eq. (5.13) and data from Table 5.1, we compute R_h, and then $\bar{\rho}_h$ accordingly. In Figure 5.2 we plot the computed halo densities *vs* their respective effective radii. Then we calculate the moments of mass distribution reported in Table 5.2 which will be used in the following to work out the galaxy–background correlation functions.

5.3 Two-point function analysis

Let $\xi_{bb}(r)$ be the 2-point background matter correlation function. According to the definition of the 2-point correlation function we gave in §2.1, we can express the amount of matter contained within a sphere of radius R centered on a randomly chosen point, according to

$$< M >_{\rm R} = \rho V_{\rm R} + \rho\ 4\pi \int_0^R r^2 dr\ \xi_{bb}(r), \tag{5.15}$$

where ρ is the average matter density (assumed to be equal to the critical density $\rho = 5 \times 10^{-30} h^2 g\ cm^{-3}$).

If the point is not random, but is selected to coincide with [the center of] a galaxy, then equation (5.15) modifies into

$$< M >_{\rm R} = \rho V_{\rm R} + \rho\ 4\pi \int_0^R r^2 dr\ \xi_{gb}(r), \tag{5.16}$$

to give the mass contained within a radius R of the galaxy center. Here $\xi_{gb}(r)$ is the *galaxy–background* cross–correlation function.

Taking now $\xi_{gb}(r) = (r_o/r)^\gamma$ and for $R \ll r_o$, from eq. (5.16) we obtain

$$\frac{< M >_{\rm R}}{\tilde{M}_{\rm R}} = \xi_{gb}(R) K_1, \tag{5.17}$$

with $\tilde{M}_{\rm R} = \rho V_{\rm R}$ ($V_{\rm R} = 4\pi R^3/3$) and $K_1 = 3/(3-\gamma)$.

Dividing numerator and denominator of the l.h.s. of (5.17) by $V_{\rm R}$, the ratio $\bar{\rho}_{\rm R}/\rho$ is obtained. This is to be compared with relation (5.14) when R is the halo radius. In spite of the approximate significance of eq. (5.14), it is worth to perform a comparison, which shows that

$$R_o = K_1^{1/\gamma} r_o. \tag{5.18}$$

Henceforth from the numerical value of R_o given in (5.10) one could work out a tentative value for the *clustering length* r_o ranging around 6.2 Mpc and with an error of $\sim 40\%$. An actual value of the clustering length will be deduced from the homogeneous PS90 sample in the rest of this section (see Table 5.2).

Much of the simplicity of eq. (5.17) depends on the power–law assumption for the 2-point function. We can compare the results of this assumption with observational behaviours. In the analysis of the 2-point function one might simply consider the value of M, estimated for each single galaxy of the sample from its average internal density and radius, as a function of the galaxy (halo) size R (see Figure 5.2).

However, in view of further applications, we prefer to collect actual objects into 5 bins, each having the same logarithmic amplitude, $\kappa = 1.74$, and a characteristic radius $r_k = 17.0\, k\, kpc$ which coincides with the logarithmic center of the bin itself (see Table 5.3).

More in detail, from a theoretical point of view, the average performed inside the k-th bin corresponds to the output of the integration

$$\frac{< M >_k}{\tilde{M}_k} = K_1 \int_{r_k}^{r_{k+1}} \xi_{gb}(r) p_r dr \tag{5.19}$$

where p_r is a weight function fulfilling the normalization requirement $\int_{r_k}^{r_{k+1}} p_r dr = 1$. Taking $p_r = N(\alpha) r^\alpha$, [$N(\alpha)$ is the normalization factor], we have

$$log \frac{< M >_k}{\tilde{M}_k} = \Phi(\alpha, \gamma, r_o, k), \tag{5.20}$$

where

$$\Phi(\alpha, \gamma, r_o, k) = \gamma\ log\ \frac{r_o}{\kappa r_k} + log\ K_1 + log \frac{\kappa^{\alpha+1-\gamma} - 1}{\kappa^{\alpha+1} - 1} - log \frac{\alpha + 1 - \gamma}{\alpha + 1}. \tag{5.21}$$

Minimizing

$$\Sigma_\alpha = \sum_{k=1}^{5} \left\{ \frac{\Phi(\alpha, \gamma, r_o, k)}{log[< M >_k / \tilde{M}_k]} - 1 \right\}^2 \tag{5.22}$$

with respect to γ and r_o does therefore correspond to an ordinary least–square fit with unweighted points. (Although each $< M >_k / \tilde{M}_k$ ratio is obtained by averaging different points and could be therefore attributed a formal error, such 'errors' are not random but systematic, and can be used to extract further information on the matter distribution.) Indeed, it should be noticed that, quite differently from what happens in usual correlation function analysis, the observational values coming from each bin are statistically independent, being built from different objects.

Best–fit values of r_o and γ and standard deviations (for $\eta = 10$ and $\Omega_o = 1$) are reported in Table 5.2 for different values of α. We find $\gamma = 1.71 \pm 0.03$ independent of α, and $r_o \simeq (6.4 \pm 0.6)\, Mpc$ only slightly dependent on α.

Table 5.2
Correlation length and slope of the 2–point function for different weighting in the bins.

α	$r_o\ (Mpc)$	γ
1	6.28 ± 0.58	1.71 ± 0.03
2	6.44 ± 0.60	1.71 ± 0.03
3	6.59 ± 0.62	1.71 ± 0.03

The value of r_o we find here is somewhat bigger than the one, $r_o \simeq 5\ Mpc$, implied by our results at R_{opt} [see eqs. (5.10) and (5.18)]. This difference is real and can be explained in the framework of a pseudo–isothermal halo density law, $\rho_h(R) = \rho_o\,[1-(R/a)^2]^{-1}$, as an effect due to the different density regimes [*i.e.*, $\rho_h(R) \sim const$ for $R \lesssim a$, and $\rho_h(R) \sim R^{-2}$ for $R > a$] where the density–radius correlation is sampled. If, in fact, $a \sim R_{opt}$ (see, *e.g.*, [199]), then the flattening of the density profile at $R \lesssim R_{opt}$ implies an estimate of the halo mass (at R_{opt}), $M_{halo}^{flat} \simeq (4/3)\,\pi\,\rho_o\,a^3$. On the other hand, if we do not take the density flattening into account and only consider the $\sim R^{-2}$ asymptotical profile, an estimate $M_{halo}^{asympt} \simeq 4\pi\rho_o a^3$ ensues. The latter mass estimate exceeds the former by a factor of ~ 2.5. The variation of the radial density profile of course reflects into the data used for estimating the mean densities, so it is not surprising to find a systematic difference between the zero-points of the density-radius correlations computed at R_{opt} and R_h. Such a difference turns into a difference by factor of $\sim 2.5^{1/\gamma} \sim 1.7$ between the estimates of r_o in the flat- and asymptotical- density regimes. Therefore we expect that the value of r_o does depend on the density regime where the density-radius correlation is sampled, being smaller (higher) in the flat- (asymptotical)-density regime, that is at small (large) distances from the galaxy centers.

A comparison between our results on ξ_{gb} and current results on the *galaxy* covariance function shows that both functions are well modeled by power laws having virtually equal slopes ($\gamma = 1.77 \pm 0.04$ for the *galaxy–galaxy* case). On the other hand, the *galaxy–galaxy* correlation length is estimated to be $8 \leq r_o \leq 15\ Mpc$ ([151,83]; and references therein), therefore it is marginally greater than the value we find. If this is the case, then our results suggest that on these scales the luminosity distribution is the shadow of the matter distribution (or vice versa), the one being obtained from the other through only a moderate bias.

5.4 N–point function analysis

Let us consider the joint expected mass value in n infinitesimal volume elements $\delta V_1, ..., \delta V_n$ at distances $r_1, ..., r_n$ from the center of a galaxy. This can be written as

$$< \delta M_1 ... \delta M_n > = \rho^n \, \delta V_1 ... \delta V_n \, [1 + \xi^{(n+1)}_{dis,01...n}], \tag{5.23}$$

where $\xi^{(n+1)}_{dis,01...n}$ is by definition the *disconnected* correlation function between a galaxy (chosen as the origin of the axes and labeled with zero in the following) and n points lying in the background. The disconnected function contains all the lower–order correlation terms that yield the $(n-m)$-point function when m points are removed, and the *connected* terms that vanish when one point is sufficiently far away (see §2.1).

Integrating n times over a sphere of radius R centered on the galaxy, we obtain

$$< M^n >_R = \rho^n \int_0^R \delta V_1 ... \int_0^R \delta V_n [1 + \xi^{(n+1)}_{dis,01...n}]. \tag{5.24}$$

We average eq. (5.24) over each bin and obtain the quantities $< M^n >_k$. These generalize the quantity $< M >_k$, defined in eq. (5.19), to higher correlation order.

Introducing now the *central moments*

$$s^{(n)}_k = \left\langle \left[\frac{M}{\tilde{M}_k} - \frac{< M >_k}{\tilde{M}_k} \right]^n \right\rangle^{1/n}_k \tag{5.25}$$

and using the binomial expansion, it can be shown that

$$\frac{< M^n >_k}{< M >^n_k} = \sum_{j=0}^{n} \frac{n!}{(n-j)!\, j!} \, \frac{(s^{(j)})^j}{(< M >_k / \tilde{M}_k)^j}. \tag{5.26}$$

The importance of eq. (5.26) owes to the fact that it gives the connection between the observational value of $s^{(n)}_k$ (reported in Table 5.3 up to $n = 5$) and the $(n+1)$-point correlation functions. Due to the large–clustering (*e.g.*, $\xi \gg 1$) regime, in what follows we forget the non–leading contributions from disconnected terms in $\xi^{(n)}_{dis}$.

Table 5.3

Central moments and population of the radial bins.

Bin limits (kpc)	$\frac{<M>_k}{\tilde{M}_k}$	$s^{(2)}_k$	$s^{(3)}_k$	$s^{(4)}_k$	$s^{(5)}_k$	Galaxies/bin
20-40	46400	17552	16740	21288	21704	4
40-70	10100	4584	2382	5109	3361	5
70-120	4350	1779	1759	2416	2627	14
120-200	1820	955	1125	1440	1604	18
200-350	808	285	272	387	413	14

A priori, the hierarchical model leads to expecting that

$$\frac{< M^n >_k}{< M >_k^n} \sim \mathcal{K}_n n^{n-2} Q_{n,a} \tag{5.27}$$

where $\mathcal{K}_n$ are geometrical factors and n^{n-2} is the total numbers of graphs of order n. Figure 5.2 shows that the scatter ΔM about $< M >_k$ in each radial bin is small. Thus, $< M^n >_k \simeq < M >_k^n$. This is in agreement with eq. (5.27) provided it is $Q_{n,a} \simeq \mathcal{K}^{-1} n^{2-n}$. One can therefore state that a hierarchical pattern is consistent with the data.

This general conclusion can be refined by means of a more detailed analysis, based on the comparison between the values obtained for $Q_{n,a}$ and those predicted in different realizations of BBGKY hierarchy. We shall show that it is possible to fit the relations expected amongst different order $Q_{n,a}$ by one of these realizations, while another case is farther from the outputs of our fit.

Following the procedure outlined in the Appendix C, it is possible to work out suitable combinations of the hierarchical coefficients (up to the sixth order):

$$\begin{aligned} Q &= 0.43 \pm 0.02, \\ Q_{4,a} + 0.36\, Q_{4,b} &= 0.18 \pm 0.02, \\ Q_{5,a} + 11.43\, Q_{5,b} + 9.90\, Q_{5,c} &= 0.67 \pm 0.11, \\ Q_{6,a} + 18.06\, Q_{6,b} + 13.39\, Q_{6,c} + 49.50\, Q_{6,d} + 43.59\, Q_{6,e} + 52.04\, Q_{6,f} &= 0.44 \pm 0.12. \end{aligned} \tag{5.28}$$

No distinctions is made here between the terms, entering in $\xi_{dis}^{(n)}$, which come from galaxy–background and purely background correlations respectively. We shall return to the effects of bias in the following.

It is however important that, according to eqs. (5.28), the galaxy–background correlation functions turn out to be safely detectable up to the sixth order. It is through such outputs on high–order correlations that, in the next section, we compare the predictions of the BBGKY equation with the actual distribution of matter in halos.

5.5 Discussion of the results

The range of scales considered in this paper has already been sampled by studying *galaxy* correlations at short distances (see Chapter 1). Groth & Peebles [97] extended the canonical behaviour $\xi_{gg}(r) = (10/r)^{1.77}$ of the two-point function deduced from the Lick catalog down to $20\,kpc$. Gott & Turner [94] and Lake & Tremaine [119] claimed the canonical form to hold down to $\sim 6\,kpc$. (Three–dimensional data do not pertain to the scale range being considered here.)

A comparison between our results on the two-point galaxy–background correlation function and the corresponding galaxy–galaxy function shows that the two

functions have strikingly similar slopes. The respective clustering lengths, however, seem to be somewhat different, being $r_{o,gb} < r_{o,gg}$. If such discrepancy is real, then the lower value of $r_{o,gb}$ can be interpreted as the signature of a biasing in the distribution of galaxies. The amount of bias, measured by the biasing parameter

$$b \;=\; \xi_{gg}/\xi_{gb}\,, \tag{5.29}$$

can be evaluated by comparing $r_{o,gg} \simeq 10\,Mpc$ and $r_{o,gb} \simeq 6.4\,\Omega_o^{-1/\gamma} Mpc$. Then,

$$b \;=\; \left(\frac{r_{o,gg}}{r_{o,gb}}\right)^{\gamma} \;\simeq\; 2.2\,\Omega_o \tag{5.30}$$

with a $\sim 20\%$ uncertainty. The above value of b is consistent with that deduced in §3.1 on the basis of very general (and different) grounds, whereby $b \sim$ 2-3. Due to the very mild dependence of $r_{o,gb}$ on η, our inferred value of b is hardly affected by the choice of η. We emphasize that eq. (5.29) is the first *direct* estimate of the biasing parameter b on the scale of galaxies, and is uniquely related to our capability of investigating the background (dark) matter statistics.

Thus, we can push our investigation to the (yet unknown) purely background functions. By analogy with eq. (5.29), the background and galaxy–background two-point functions are related by $\xi_{gb} \;=\; b\,\xi_{bb}$. Consequently, the clustering length of the DM distribution, $r_{o,bb}$, turns out to be

$$r_{o,bb} \;=\; b^{-1/\gamma} r_{o,gb} \;=\; (3.9 \pm 0.7)\, h_{50}^{-1} Mpc\,, \tag{5.31}$$

that is about one half the (canonical) value of the clustering length of galaxies. We similarly link our n-point (1 galaxy and $n-1$ background points) function to its background counterpart (*i.e.*, n background points). Indeed, due to the differences in the galaxy and background correlation properties, the 3-point correlation function we deduced in the previous section can be expressed in terms of the purely background one according to background one

$$\xi^{(3)}_{gbb} \;=\; <\delta_g \delta_b \delta_b> \;=\; b\,\xi^{(3)}_{bbb} \tag{5.32}$$

(with a transparent meaning of symbols). By assuming a similar rescaling for all the higher–order functions, and assuming the hierarchical pattern (2.23) to strictly hold only for the purely background functions, the corresponding hierarchical coefficients becomes

$$\begin{aligned}
Q^{(b)} \;&=\; 0.99 \pm 0.16 \\
R_a^{(b)} + 0.35\, R_b^{(b)} \;&=\; 0.92 \pm 0.25 \\
Q_{5,1}^{(b)} + 11.43 Q_{5,2}^{(b)} + 9.90 Q_{5,3}^{(b)} \;&=\; 7.0 \pm 3.2 \\
Q_{6,1}^{(b)} + 18.06 Q_{6,2}^{(b)} + 13.79 Q_{6,3}^{(b)} + 49.50 Q_{6,4}^{(b)} + 47.96 Q_{6,5}^{(b)} + 43.59 Q_{6,6}^{(b)} \;&=\; 9.4 \pm 5.7
\end{aligned} \tag{5.33}$$

[due to the very structure of the hierarchical pattern, the coefficients appearing in eq. (2.23) are affected by the presence of bias when going from galaxy–background

to background statistics]. Thus, according to eqs. (5.33), we are able to safely (*i.e.*, at $> 3\sigma$ level) detect background functions up to the fourth order.

Moreover, to obtain the n-point correlation function for the purely galaxy case requires a rescaling of the actual values of the corresponding galaxy–background functions by a factor b^{n-1} However, due to the very structure of the hierarchical pattern, the coefficients appearing in eq. (2.23) are left unchanged by the presence of bias when going from galaxy–background to purely galaxy statistics.

Finally, the statistically significant signal for the combinations of hierarchical coefficients allows a comparison with Fry's [79,80] and Hamilton's [100] hierarchical solutions of the BBGKY equation in the fully relaxed regime (see, *e.g.*, [53]). According to Fry, all the *trees* in eq. (2.23) have equal amplitudes

$$Q_{n,a} = Q_n = \left(\frac{4Q}{n}\right)^{n-2} \frac{n}{2n-2}. \tag{5.34}$$

On the other hand, Hamilton argues that eq. (2.23) can be taken as a solution of the BBGKY equation when only contributions from *snake* graphs are considered. Consequently,

$$Q_{n,snake} = Q^{n-2}, \qquad Q_{n,non-snake} = 0. \tag{5.35}$$

In Table 5.4 we report the value for the combinations of hierarchical coefficients (5.28) on the basis of the two solutions (5.34) and (5.35) of the BBGKY equations, and compare them with our results. There are indications that Fry's solutions are in significantly better agreement, as they predict values of those combinations remarkably well up to the fifth order, and still within $\sim 1.5\,\sigma$ for the sixth order. It is rather surprising that quantities of vastly different magnitudes entering in the combinations (5.28) concur to values of the combinations themselves which nicely compare with our computed values. In the case of purely background functions, however, we can not discriminate between Fry's and Hamilton's solutions. In fact at the fourth order both solutions overlap with our signal, and no meaningful comparison is allowed at higher orders.

Table 5.4

Values of combinations of the hierarchical coefficients, from observations and from Fry's and Hamilton's solution of the BBGKY equation.

Correlation order	4^{th}	5^{th}	6^{th}
Observations	0.175 ± 0.015	0.675 ± 0.107	0.44 ± 0.12
Fry	0.167 ± 0.015	0.567 ± 0.081	0.70 ± 0.13
Hamilton	0.123 ± 0.011	0.787 ± 0.110	1.49 ± 0.28

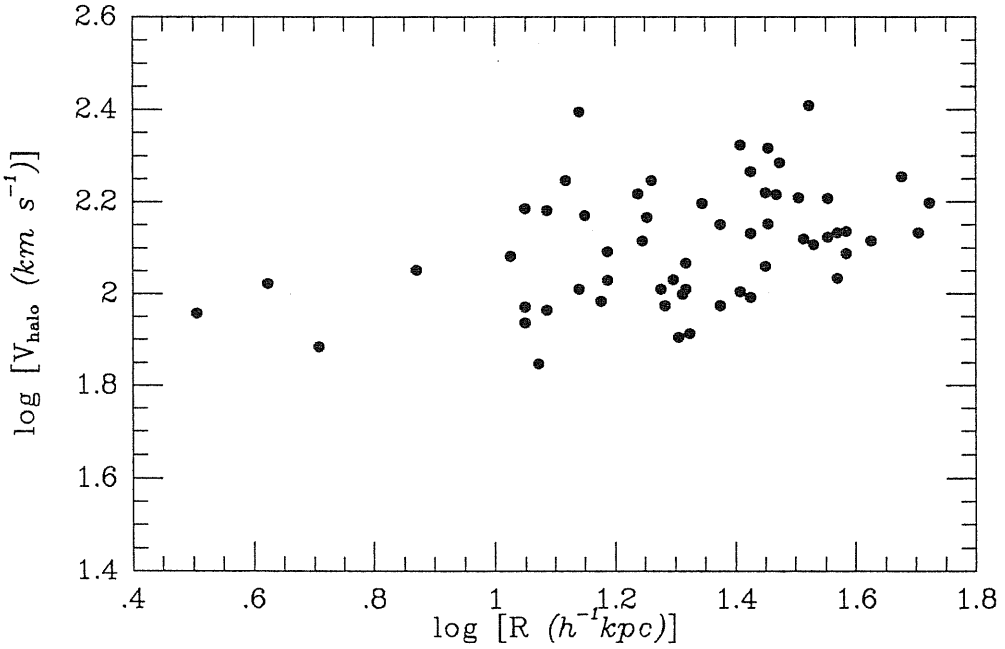

Figure 5.3: *The r.m.s halo components of the observed velocity as a function of the optical radius for our sample of spiral galaxies.*

Comparing our higher–order results with BBGKY predictions is particularly relevant in that the BBGKY equation predicts a hierarchical pattern for higher–order correlations only in the statistical equilibrium limit [53]. Statistical equilibrium is in fact expected on the scale of galaxies, where relaxation processes have already taken place, while it is hardly expected on the much larger scales of galaxy clustering.

We conclude this section by pointing out that the PS90 sample, upon which our analysis is based, does not involve any obvious bias other than the requirement that its galaxies should have good–quality photometric and kinematic data, to insure a reliable determination of both the luminous and the total mass distributions. Any possible error coming from inaccuracies in the rotation curve data and data analysis is not included in the quoted formal errors.

5.6 The Cosmic Virial Theorem inside spirals

Instead of deducing the amount of halo matter contained inside the optical radius by imposing the condition of centrifugal equilibrium (5.7) to each galaxy, we can alternatively require a stability condition that is valid in statistical sense. To this purpose, let us observe that, at dynamical equilibrium, rotation velocity supports the action of the gravitational field. This implies that the *expected* mass excess for the

halo component inside the radial distance R is

$$\delta M_{\rm R} \;=\; G^{-1}\, V_{halo}^2(R)\, R\,. \tag{5.36}$$

The corresponding mass fluctuation (in a FRW Universe) associated with this scale,

$$\frac{\delta M_{\rm R}}{M_{\rm R}} \;=\; \frac{2}{\Omega_o}\left(\frac{V_{halo}}{H_o R}\right)^2, \tag{5.37}$$

is the analogous of eq. (5.1), that holds for the relative motions of galaxy pairs. In eq. (5.37), R is the optical disk radius, and V_{halo} is the halo component of the observed rotation velocity in the plane of the disk, V.

According to eq. (5.37), $\delta M_{\rm R}/M_{\rm R}$ can be obtained by searching our sample of galaxies for a correlation between V_{halo} and R. From the data plotted in Figure 5.1*a* we derive the correlation

$$\left(\frac{V_{halo}}{km\,s^{-1}}\right)^2 \;=\; A\left(\frac{R}{kpc}\right)^{\alpha}$$

$$A = (6.9 \pm 1.4)\times 10^3, \qquad \alpha = 0.30 \pm 0.07\,. \tag{5.38}$$

We notice that eq. (5.38) can be read as $V_{halo} = 230^{+100}_{-70}\,(r/Mpc)^{0.15\pm0.03}\ km\,s^{-1}$. This expression is consistent, to within less than $1\,\sigma$, with the galaxy-pair result [52]. We can then conclude that the relation between peculiar velocity and scale, originally found to hold on the Mpc scale, does in fact extend down to the kpc scale. Inserting eq. (5.38) in eq. (5.37) we finally get

$$\frac{\delta M_{\rm R}}{M_{\rm R}} \;=\; B\left(\frac{R}{Mpc}\right)^{-\gamma}$$

$$B = (43.8 \pm 8.9)\,\Omega_o^{-1}, \qquad \gamma = 1.70 \pm 0.07\,, \tag{5.39}$$

with a slope γ that is perfectly consistent with that found in §5.2. So we find that, as a consequence of eq. (5.39), excess in mass does scale with distance like excess in number, eq. (5.3), all the way down to the scale of faint spiral disks ($\gtrsim 3\,h_{50}^{-1}\,kpc$), thus vindicating Peebles's [155] arguments about the continuity in the clustering pattern down to galaxy scales. The key realization is that the *galaxy-pairs* technique applies to scales where the mass fluctuations are anyway largely driven by dark matter, while our *spiral-galaxy* technique applies to scales where dark matter and luminous matter concur to the total mass fluctuations (and associated steady circular motions) in comparable fashions. Therefore, if any underlying continuity in the clustering properties of matter on different scales has to be uncovered, dark and luminous matter should get decoupled on the kpc scale.

Moreover, by comparing eq. (5.39) with eq. (5.17), we get for the galaxy–background correlation length

$$r_{o,gb}\;\Omega_o^{1/\gamma} \;=\; (5.7 \pm 1.2)\;Mpc\,, \tag{5.40}$$

that is still consistent with the analogous result found in §5.2 at the optical radius. Thus, assuming $r_{o,gg} \simeq 10\ Mpc$ for the galaxy–galaxy correlation length, we find

$$\Omega_o\, b^{-1} \;=\; 0.37 \pm 0.13\,. \tag{5.41}$$

Such relation gives the relevant cosmological parameters in two particular scenarios. If we postulate that light is a fair tracer of mass (namely, $b = 1$) on the scale of spiral disks, then we estimate the contribution to the mean mass density coming from matter distributed like galaxies to be $\Omega_o = 0.37 \pm 0.13$. On the other hand, if we allow for a *biased* distribution of galaxies in an $\Omega_o = 1$ cosmology, we obtain a biasing parameter $b = 2.7^{+1.4}_{-0.7}$.

In order to discriminate in favor of one particular model Universe, a further step has to be made. To this purpose, we implement a different formulation of the condition for dynamical stability which involves a three-point function, $\zeta \sim Q\,\xi^2$, and the background-background correlation length, $r_{o,bb}$. This approach, known as Cosmic Virial Theorem [149,150], requires that motion stability be consistent with hydrostatic equilibrium, and provides a link between mass distribution and *r.m.s.* velocity dispersion for a self-gravitating system of collisionless particles. In the case of co-planar velocities, as for spiral galaxies, it implies

$$< V^2_{halo} >_{\rm R} \;=\; \frac{3\,M_\gamma\,\Omega_o\,Q\,H_o^2\,r^\gamma_{o,bb}}{4(\gamma-1)(2-\gamma)(4-\gamma)}\,R^{2-\gamma}\,. \tag{5.42}$$

[This formula can be interpreted as follows: the relative motion of two particles in the system (*i.e.*, the halo) depends on a two-body pressure term, which involves ξ, and on a three-body gravitational term with *any* other third background particle, which involves ζ_{gbb}. The quantity M_γ is a suitable numerical coefficient: $M_{1.70} = 4.12$, $M_{1.80} = 3.70$.] On the other hand, dynamical equilibrium [see eqs. (5.37) and (5.17)] also implies that

$$< V^2_{halo} >_{\rm R} \;=\; \frac{3\,\Omega_o\,H_o^2\;r^\gamma_{o,gb}}{2\,(3-\gamma)}\;R^{2-\gamma} \tag{5.43}$$

(in the $\xi_{gb} \gg 1$ regime). Equating eqs. (5.42) and (5.43) yields

$$r_{o,bb} \;=\; \left[\frac{2\,(\gamma-1)\,(2-\gamma)\,(4-\gamma)}{M_\gamma\,Q\,(3-\gamma)}\right]^{1/\gamma}\;r_{o,gb}\,. \tag{5.44}$$

By inserting in eq. (5.44) the value of the 3-point coefficients, $Q = 0.43 \pm 0.02$, that we found in §5.4, and taking into account eq. (5.40), it results $r_{o,bb} = (3.3 \pm 0.7)\Omega_o^{-1/\gamma}$. On the other hand, the definition of the biasing parameter (*i.e.*, $\xi_{gg} = b\,\xi_{gb} = b^2\,\xi_{bb}$) implies $r_{o,gg} = r_{o,bb}\,b^{2/\gamma}$. Combining the previous two expressions allows us to add to eq. (5.41) the equation we were looking for in order to close the system,

$$b^2\,\Omega_o^{-1} \;=\; 7.1^{+2.0}_{-3.7}\,. \tag{5.45}$$

By solving eqs. (5.41) and (5.45) simultaneously, we get

$$\Omega_o = 1.0 \pm 0.2\,, \qquad\qquad b = 2.7^{+0.6}_{-0.4}\,. \tag{5.46}$$

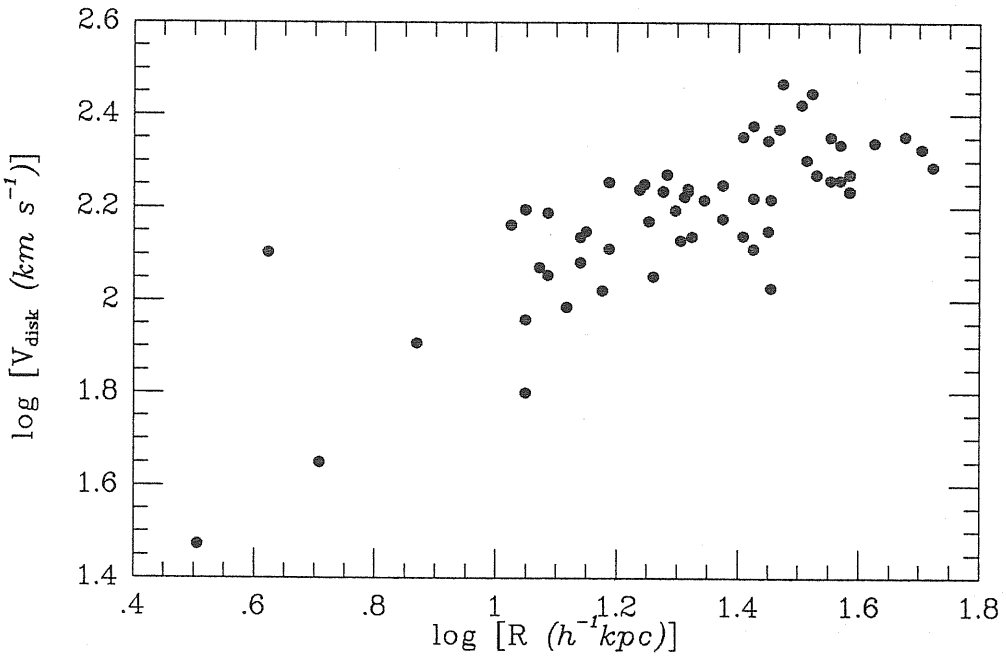

Figure 5.4: *The r.m.s disk components of the observed velocity as a function of the optical radius for our sample of spiral galaxies.*

Therefore, the internal structure and dynamics of spiral galaxies seem to require a flat Universe where the distribution of galaxies is biased over that of matter.

So far we have implicitly assumed that dark halos are the only contributors to the internal structure of spiral galaxies having a physical relevance to the spatial distribution of galaxies. Our motivations for doing so were both continuity with the procedure for probing the distribution of matter within galaxy pairs and homogeneity of the information on matter statistics at small and large scales. However, it is reasonable to ask what happens when we consider disks rather than halos. If the mass contribution of luminous disks were the same for all galaxies irrespective of luminosity, we should expect eq. (5.38) to hold (for the disk component of the rotation velocity) with a different normalization but with the same slope. Actually, the progression with luminosity of the shape of rotation curves on scales $r \lesssim R$ [175] indicates that the halo mass contribution rises systematically with decreasing luminosity, $M_{halo}/M_{disk} \sim L_B^{-0.7}$ [158,160,161], so for the correlation function of *disk* matter we expect a value of γ substantially lower than ~ 1.7. Indeed, for our sample it turns out $\gamma = 1.23 \pm 0.09$ (see Figure 5.4). This striking difference between the autocorrelations of dark and luminous matter highlights the fact that different properties of dissipation necessarily involve different properties of clustering.

5.7 A brief summary of the results

In this chapter we presented the first direct study on the correlation of (dark) matter with galaxy sites. The procedure we adopted is based on the properties of dark galaxy halos deduced from the observed kinematics of rotating disk galaxies. Our method allowed us to investigate galaxy–background correlations with an accuracy higher, even for a rather limited sample of galaxies, than for galaxy correlations analysed through the usual number counts technique applied to large samples. In fact, computing the density of one halo is effectively analogous to counting all the objects within a given distance of a galaxy center; in addition, there is no intersection among the information coming from individual galaxies.

The two-point *galaxy–background* correlation function we obtained is a power law with same slope as the two-point *galaxy* function. A marginal discrepancy between the respective clustering lengths might be indicative of bias. If such is the case, a biasing parameter $b \sim (2\text{–}3)\,\Omega_o$ connects galaxy and background distributions. The range of scales we sampled widely overlaps with the range sampled through galaxy counts, our data extending to yet smaller scales. We find that at such small scales $\xi(r)$ lies on the extrapolation from its known behaviour at larger scales. This seems to indicate that the fluctuation spectrum has the same slope on scales ranging from $\sim 10\,h_{50}^{-1}\ Mpc$ down to $\sim 3\,h_{50}^{-1}\ kpc$, despite the expectation that non–linear evolution and virialization of primeval structure may have modified the (original) fluctuation spectrum on galaxy scales.

As for higher–order correlations, a significant point is that the hierarchical pattern is allowed by observational data up to the sixth order. Suitable combinations of the hierarchical coefficients $Q_{n,a}$ are also obtained.

Moreover, by requiring hydrostatical equilibrium for the halos of our sample of spiral galaxies with known rotation curves, we find that a flat Universe ($\Omega_o = 1$) with a corresponding biasing parameter $b \sim$ 2-3 seems to be favored by the internal kinematics of galaxies. In addition, by requiring dynamical stability also for the luminous disks, we find a strikingly different correlation function for the luminous matter, with slope $\gamma \simeq 1.2$.

We would like to emphasize that obtaining information on the dynamics of dark matter on galaxy scales depends quite crucially on our capability of decomposing rotation curves into their (luminous) disk and (dark) halo components. If, for example, we assumed that the relative disk and halo mass contributions were identical for galaxies of all luminosities (*i.e.*, if the halo velocity component were a constant fraction of the observed rotation velocity), then we would obtain $\gamma \sim 1.4$. This, however, would disagree with the expectation, based on continuity arguments with the galaxy-pairs technique, that $\xi_{gg} \propto \xi_{bb}$. Therefore, we regard our success in showing that indeed on the scale of galaxies it is $\xi_{gg} \propto \xi_{bb}$, as a strong case in favor of a systematic variation of the (percentual) dark matter content in galaxies with luminosity, $M_{halo}/M_{disk} \propto L_{\rm B}^{-0.7}$, in agreement with rotation curve results. More generally,

we can state that, for a stable clustering, the classic measurement of the galaxy two-point correlation function [151] does imply that the dark-matter contribution to the internal dynamics of galaxies increases with decreasing galaxy luminosity. Internal structure and spatial distribution of galaxies seem to be inherently and profoundly connected.

The content of §5.2 to §5.5 is included in two papers, the first already published in *The Astrophysical Journal* [25], the second recently accepted by *The Astrophysical Journal* [32]. Moreover, such results are also published in the *Proceedings of Moriond Astrophysics Meeting 1990* [33]. The content of §5.6 constitutes part of a further paper [178] that will be soon submitted for publication.

Conclusions

In this Thesis we presented a description of various statistical methods for investigating the large–scale structure of the Universe with particular attention to the study of the correlation properties of cosmic structures. After reviewing, in Chapter 1, the observational material concerning the clustering of galaxies and galaxy clusters, we described, in Chapter 2, the technical framework for the study of the correlation properties of these distributions. Particular attention has been devoted in introducing the concept of the n-point correlation function and to describe the *path–integral* formalism, relevant to the study of correlation functions.

We introduced, in Chapter 3, the concept of *biased* theory for the formation of cosmic structures and thereafter we presented our original results. Biased models are particularly interesting because they are able to account in the different correlation properties that are observed for different classes of objects. In its original formulation a *biased* distribution of galaxies or clusters arises if these objects are identified with those peaks of the primordial fluctuation field that exceed a fixed amplitude. This amounts in selecting fluctuations by means of a sharp threshold (θ–threshold case). This threshold gives zero probability to fluctuations below a critical amplitude to turn into observable structures and unity probability for a fluctuation above the threshold level to give rise to an object. We argued that such a picture represents an oversimplification; the strongly non–linear phenomena occurring during the structure formation process are such that a sharp cut, operated on the density fluctuation field, is probably inadequate to relate the distribution of the background matter to that of galaxies and galaxy systems. In this context if we are able to take into account the dynamics of galaxy formation, by means of suitable shapes for the threshold function, the introduction of non–θ thresholds represents the natural solution. Chapter 3 was devoted to the description of our general model used to express the correlation properties of the object distribution (in presence of an arbitrary shape for the threshold function) in terms of those of a generic non–Gaussian background distribution. A remarkable result that we found is that the n-point correlation function can be written as a suitable combination of the 2-point functions which looks like a generalization of the Kirkwood superposition (2.22). Moreover, in the *high–threshold* approximation, when objects form from exceptionally high peaks, the effect of the threshold shape vanish and the *θ-bias* case in completely recovered.

In Chapter 4 we tested our general *biased* models versus observational data.

In particular we considered two specific thresholds, the *erfc* and the Gaussian ones, whose shapes are related to non–sphericity in the gravitational collapse process and to merging between different scale fluctuations. A comparison with observational data on the multiplicity function of galaxy systems and on the 2-point correlation function of rich Abell clusters showed the existence of a sensitive dependence on the shape of the threshold. This represents a clear indication that neglecting the effects of non–spherical collapse and merging in the formation of cosmic structures can be very misleading. We found that a good fit to the observed multiplicity function is obtained if non–sphericity in the gravitational collapse is taken into account. Moreover, introducing the effects of fluctuation merging improve the fit of our models 2-point correlation function to the Abell clusters. As an additional output, we showed that, for any choice of the threshold function, the CDM model fails to reproduce the observed very large scale clustering. Indeed, the CDM spectrum predicts a 2-point function that goes to zero on scales $r \sim 30\,h^{-1}Mpc$ while data shows no evidence of anticorrelation up to $r \sim 60\,h^{-1}Mpc$. Better results have been obtained with a *scale–free* spectrum with spectral index $n = -1.2$.

In order to make possible a test on the reliability of *biased* model, we presented in Chapter 5 a new approach to directly investigate the correlation properties of the background matter surrounding galaxies. Such an approach is essentially based on the observation that spiral galaxy rotation curves can be used as tracers of the matter distribution on galaxy scales, in the same way as galaxy peculiar motions are used to trace the matter density on larger scales. However, since structures involving typical scales of galaxy clustering are dynamically dominated by dark matter, a meaningful comparison between correlation properties of galaxies and background matter should be done by considering only the contribution of dark (halo) matter to the observed rotation velocities. Indeed, we applied the Persic & Salucci mass decomposition method [158,161] to a fair sample of spiral rotation curves and found that the 2-point correlation function, for the dark matter, has the same slope as the galaxy function. Any difference in the clustering amplitude is to be ascribed to the presence of a *bias* between galaxy and matter distributions. On the contrary, significant discrepancies in the slope of the 2-point function are found if we consider the luminous disk component. The application of the Cosmic Virial Theorem to the clustering pattern of dark matter on galaxy scales suggests a flat Universe ($\Omega_o = 1$) with a biasing parameter $b \sim 2$–3. The extension of this analysis to higher correlation orders is also possible and shows that the *hierarchical* expression (2.23) for the n-point function is satisfied. A quantitative comparison of our deduced values for the hierarchical coefficients and the predictions of the BBGKY equations shows a remarkable good agreement.

In our opinion, the results presented in this Thesis open also the possibility for further investigations. For example, it would be interesting to compare the predictions of *biased* models with the correlation properties of different samples of galaxy groups, each characterized by different criteria, such as richness, to identify a physical group. In fact, different values of the galaxy density contrast used to identify a

group or cluster is equivalent to different fluctuation threshold levels that give rise to structures. A quantitative comparison between the increase of the correlation strength with increasing group richness and the corresponding outputs of the biased model for higher and higher threshold levels could be a crucial test for the theory. Also interesting to check is the possibility of reaching the high–threshold regime, in which the effects of a non–sharp biasing disappear, in correspondence of the richest cluster distribution.

Important tests for the *biased* galaxy formation model can also arise from numerical N-body simulations. Indeed, such an is approach particularly useful to investigate the structure formation on scales relevant to galaxy clustering, where highly non–linear evolution of fluctuations renders any analytical approach. In a very recent paper, that has been not presented here (Valdarnini & Borgani 1990; ref. [198]), we used a P^3M code to follow the non–linear evolution of clustering pattern for different initial spectra and biasing level. The analysis of the 3- and 4- point correlation functions shows that they approach the *hierarchical* pattern (2.23) as we consider smaller and smaller scales and more evolved configurations (in accordance with the models of gravitational instability). Another interesting result is that the effect of introducing a biasing in the background distribution strongly depends on the shape of the primordial spectrum. In particular, amplification in the correlation strength occurs only for spectra having sufficient power on large scales, while such differences are not found for a scale–free spectrum with $n = 1$ (which has small amplitude on large scales).

As a concluding remark, we would like also to stress the importance of our method, presented in Chapter 5, for investigating the small scale clustering of dark matter. In fact, such a method could probably open a new window in our understanding of the connection between background and galaxy distributions, once new rotation velocity data become available. Especially interesting could be observations of spirals in different environments and of low-luminosity (*i.e.*, optically small) galaxies. In fact the investigation of the distribution of matter around galaxies in different systems (clusters or groups) would test whether differences in the galaxy clustering pattern, within different environments, reflect similar differences in the clustering properties of the background matter. We point out that faint galaxies highlight the smallest observable clumps of matter on galaxy scales and are dynamically dominated by dark matter. For these reasons low-luminosity galaxies seem to be ideal tools for probing the distribution of (dark) matter down to scales $r \sim 1\, h_{50}^{-1}\, kpc$. In general it would be interesting to apply our analysis to spirals having different morphology. In fact, from the analysis of homogeneous samples, substantial differences have been found between the 2-point correlation function of Sa, Sb and Sc galaxies (see also §1.2). Finding such differences also in the clustering of dark matter would represent a clear indication of a deep connection existing between small–scale matter clustering and large–scale galaxy distribution.

Appendix A

Correlation properties of the biased field

In this appendix we describe in detail the calculations to deduce the statistical properties of the *biased* field, that have been described in Chapter 3. In particular, we will obtain the expressions (3.9) for the N-point joint probability (see §3.3), (3.53) for the joint probability between the galaxy and cluster distributions (see §3.6), and (3.72) for the N-point probability of the *exponential* threshold (see §3.8).

A.1 The N-point probability

For a given threshold function $f(\alpha)$, the expression

$$\Pi^{(N)}_{\nu,\mathrm{R}}(x_1,...,x_\mathrm{N}) \;=\; \int D[\epsilon(x)]\,P[\epsilon(x)] \prod_{r=1}^{N} \int_{\nu\sigma_\mathrm{R}}^{+\infty} d\alpha_r\, f'(\alpha_r) \tag{A.1}$$

for the joint probability will be clearly equivalent to eq. (3.8). This allows us to make use of eq. (3.11) and to obtain

$$\begin{aligned}\Pi^{(N)}_{\nu,\mathrm{R}}(x_1,...,x_\mathrm{N}) \;&=\; (2\pi)^{-N/2} \int_{\nu\sigma_\mathrm{R}}^{+\infty} d\alpha_1 ... \int_{\nu\sigma_\mathrm{R}}^{+\infty} d\alpha_\mathrm{N} \int_{-\infty}^{+\infty} d\phi_1 ... \int_{-\infty}^{+\infty} d\phi_\mathrm{N} \;\times \\ \times\; &\left[\prod_{r=1}^{N} (i\phi_r)^l\, \tilde{g}(\phi_r)\, e^{-i\alpha_r\phi_r}\right] \int D[\epsilon(x)]\,P[\epsilon(x)] \;\times \\ \times\; &exp\left\{ i \sum_{r=1}^{N} \phi_r \int dx\, Q_\mathrm{R}(|x-x_r|)\epsilon(x) \right\}, \end{aligned} \tag{A.2}$$

which, according to the definition (2.58) of partition functional, reads

$$\begin{aligned}\Pi^{(N)}_{\nu,\mathrm{R}}(x_1,...,x_\mathrm{N}) \;&=\; (2\pi)^{-N/2} \int_{\nu\sigma_\mathrm{R}}^{+\infty} d\alpha_1 ... \int_{\nu\sigma_R}^{+\infty} d\alpha_\mathrm{N} \int_{-\infty}^{+\infty} d\phi_1 ... \int_{-\infty}^{+\infty} d\phi_\mathrm{N} \;\times \\ \times\; &\left\{\prod_{r=1}^{N} (i\phi_r)^l\, \tilde{g}(\phi_r)\, e^{-i\alpha_r\phi_r}\right\} \times Z[J^*]\,. \end{aligned} \tag{A.3}$$

In the above expression, the quantity

$$J^*(x) \;=\; \sum_{r=1}^{N} \phi_r Q_{\rm R}(|x - x_r|) \tag{A.4}$$

play the role af an external source. Let us expand $ln\, Z[J_x^*]$ in functional McLaurin series, making use also of the definition (2.96) of *smoothed* correlation functions. This enable us to obtain the expression

$$\Pi^{(N)}_{\nu,{\rm R}}(x_1,...,x_{\rm N}) \;=\; (2\pi)^{-N/2} \int_{\nu}^{+\infty} d\alpha_1 ... \int_{\nu}^{+\infty} d\alpha_{\rm N} \int_{-\infty}^{+\infty} d\phi_1 ... \int_{-\infty}^{+\infty} d\phi_{\rm N} \times$$

$$\times \left\{ \prod_{r=1}^{N} \left(i \frac{\phi_r}{\sigma_{\rm R}} \right)^l \tilde{g}\left(\frac{\phi_r}{\sigma_{\rm R}} \right) \right\} \times exp\left\{ \sum_{n=2}^{\infty} \frac{i^n}{n!} \sum_{[r_n]=1}^{N} \frac{\xi^{(n)}_{con,{\rm R}}(x_{r_1},...,x_{r_n})}{\sigma_{\rm R}^n} \prod_{j=1}^{n} \phi_{r_j} \right\} \times e^{-i\alpha_r \phi_r} \tag{A.5}$$

(here $\sum_{[r_n]} \equiv \sum_{r_1=1}^{N} ... \sum_{r_n=1}^{N}$). If we also expand

$$exp\left\{ \sum_{r=1}^{N} h(\phi_r) \right\} \;=\; e^{Nh(0)} exp\left\{ \sum_{n=1}^{\infty} \frac{1}{n!} \sum_{[r_n]=1}^{N} h^{(n)}(0) \prod_{k=1}^{n-1} \delta_{r_k, r_{k+1}} \prod_{j=1}^{n} \phi_{r_j} \right\} \tag{A.6}$$

and take into account the formal relation

$$t(\phi)\, e^{-i\alpha\phi + \beta\phi^2} \;=\; t\left[i\left(\frac{d}{d\alpha} \right) \right] e^{-i\alpha\phi + \beta\phi^2} \tag{A.7}$$

holding for any constant β and function t, eq. $(A.5)$ also reads

$$\Pi^{(N)}_{\nu,{\rm R}}(x_1,...,x_{\rm N}) \;=\; (2\pi)^{-N/2} e^{Nh(0)} \times$$

$$\times \int_{\nu}^{+\infty} d\alpha_1 ... \int_{\nu}^{+\infty} d\alpha_{\rm N} \int_{-\infty}^{+\infty} d\phi_1 ... \int_{-\infty}^{+\infty} d\phi_{\rm N} \left\{ \prod_{r=1}^{N} \left(-\frac{1}{\sigma_{\rm R}} \frac{\partial}{\partial \alpha_r} \right)^l \right\} \times$$

$$\times \; exp\left\{ \sum_{n=1}^{\infty} \frac{(-1)^n}{n!} \sum_{[r_n]=1}^{N} \left[\frac{h^{(n)}(0)}{(i\sigma_{\rm R})^n} \prod_{k=1}^{n-1} \delta_{r_k, r_{k+1}} + w^{(n)}_{{\rm R},[r_n]} \right] \prod_{j=1}^{n} \frac{\partial}{\partial \alpha_{r_j}} \right\} \times$$

$$\times \; exp\left(-\frac{1}{2} \sum_{r=1}^{N} \phi_r^2 - i \sum_{r=1}^{N} \alpha_r \phi_r \right). \tag{A.8}$$

Let us recall that the functions $w^{(n)}_{{\rm R},[r_n]}$ are defined according to eq. (3.12). By using the expression for the Fourier transform of a Gaussian function and performing the integration over the variables ϕ_r, eq. $(A.8)$ simplifies into

$$\Pi^{(N)}_{\nu,{\rm R}}(x_1,...,x_{\rm N}) \;=\; \sigma_{\rm R}^{-lN} e^{Nh(0)} \int_{\nu}^{+\infty} d\alpha_1 ... \int_{\nu}^{+\infty} d\alpha_{\rm N} \left\{ \prod_{r=1}^{N} \left(-\frac{\partial}{\partial \alpha_r} \right)^l \right\} \times$$

$$\times \; exp\left\{ \sum_{n=1}^{\infty} \frac{(-1)^n}{n!} \sum_{[r_n]=1}^{N} \left[\frac{h^{(n)}(0)}{(i\sigma_{\rm R})^n} \prod_{k=1}^{n-1} \delta_{r_k, r_{k+1}} + w^{(n)}_{{\rm R},[r_n]} \right] \prod_{j=1}^{n} \frac{\partial}{\partial \alpha_{r_j}} \right\} \times$$

$$\times \; exp\left(-\frac{1}{2} \sum_{r=1}^{N} \alpha_r^2 \right). \tag{A.9}$$

Integration over α_r will then be possible only after expanding the exponential factor in eq. $(A.9)$ in order to separate different order derivatives. This requires making recourse to the clustering expansion technique [138], that has been originally introduced in real gas statistical thermodynamics. In this context, the multinomial expansion theorem shall be used, simply stating

$$(y_1 + y_2 + ... + y_k)^n = \sum_{[n_i]=1}^{n} \frac{n!}{n_1!...n_k!} y_1^{n_1}...y_k^{n_k} . \tag{A.10}$$

In such expression, the integers $[n_i] = n_1, ..., n_k$ fulfill the condition

$$\sum_{i=1}^{k} n_k = n . \tag{A.11}$$

This leads to the expression

$$\Pi^{(N)}_{\nu,\mathrm{R}}(x_1, ..., x_\mathrm{N}) = \sigma_\mathrm{R}^{-lN} e^{Nh(0)} \sum_{L=0}^{\infty} \sum_{[m_L]} \left[\prod_{n=1}^{L} \prod_{[r_n]=1}^{N} \left(\frac{W^{(n)}_{\mathrm{R},[r_n]}}{n!} \right)^{m_{n,[r_n]}} \frac{1}{m_{n,[r_n]}!} \right] \times$$
$$\times \int_{\nu}^{+\infty} d\alpha_1 ... \int_{\nu}^{+\infty} d\alpha_\mathrm{N} \left\{ \prod_{r=1}^{N} \left(-\frac{\partial}{\partial \alpha_r} \right)^{l+m(r)} \right\} e^{-\frac{1}{2}\alpha_r^2} \tag{A.12}$$

from which eq. (3.9) can be easily obtained, once the definitions of the coefficients $a^{(l)}_{m(r)}(z)$ are taken into account [see also eqs. (3.13) and (3.14)].

A.2 Joint statistics of galaxy and cluster distributions

Following the same calculation scheme as in the previous subsection, the galaxy–cluster joint probability expression (3.51) can be written as

$$\Pi^{(2)}_{cg}(x_1, x_2) = \frac{1}{2\pi} \int_{\nu_c \sigma_{\mathrm{R}_c}}^{+\infty} d\alpha_1 \int_{\nu_g \sigma_{R_g}}^{+\infty} d\alpha_2 \int_{-\infty}^{+\infty} d\phi_1 \int_{-\infty}^{+\infty} d\phi_2 \times$$
$$\times (i\phi_1)^{l_c} (i\phi_2)^{l_g} e^{h(\phi_1)+h(\phi_2)} e^{-i(\alpha_1\phi_1+\alpha_2\phi_2)} \times Z[J^*] . \tag{A.13}$$

Here the external source takes the expression

$$J^*(x) = \phi_1 Q_{\mathrm{R}_c}(|x_1 - x|) + \phi_2 Q_{\mathrm{R}_g}(|x_2 - x|) . \tag{A.14}$$

The McLaurin functional expansion of $ln\, Z[J^*]$ gives

$$\Pi^{(2)}_{cg}(x_1, x_2) =$$
$$= \frac{1}{2\pi} \int_{\nu_c}^{+\infty} d\alpha_1 \int_{\nu_g}^{+\infty} d\alpha_2 \int_{-\infty}^{+\infty} d\phi_1 \int_{-\infty}^{+\infty} d\phi_2 \left(i\frac{\phi_1}{\sigma_{\mathrm{R}_c}} \right)^{l_c} \left(i\frac{\phi_2}{\sigma_{\mathrm{R}_g}} \right)^{l_g} e^{h_c(\frac{\phi_1}{\sigma_{\mathrm{R}_c}})+h_g(\frac{\phi_2}{\sigma_{\mathrm{R}_g}})} \times$$
$$\times exp\left\{ \sum_{n=2}^{\infty} i^n \sum_{j=0}^{n} \frac{\xi^{(n)}_{con,[\mathrm{R}_c,j;\mathrm{R}_g,n-j]}}{j!(n-j)!} \phi_1^j \phi_2^{n-j} \right\} e^{-i(\alpha_1\phi_1+\alpha_2\phi_2)} , \tag{A.15}$$

where the correlation functions between fields that are smoothed on different scales read

$$\xi^{(n)}_{con,[\mathrm{R}_c,j;\mathrm{R}_g,n-j]} = \int \Big[\prod_{k=1}^{j} dy_k\, Q_{\mathrm{R}_c}(|x_1 - y_k|)\Big]\Big[\prod_{l=1}^{n-j} dy_l\, Q_{\mathrm{R}_g}(|x_2 - y_l|)\Big]\xi^{(n)}_{con}(y_1,...,y_n)\,. \tag{A.16}$$

By expanding the functions $h(\phi)$ in McLaurin series and after rearranging the terms of such expansion, we get

$$h_c(\phi_1)+h_g(\phi_2) = h_c(0)+h_g(0)+\sum_{n=1}^{\infty}\sum_{j=0}^{n}[h_c^{(j)}(0)\delta_{nj}+h_g^{(n-j)}(0)\delta_{0j}]\frac{\phi_1^j\phi_2^{n-j}}{j!\,(n-j)!}\,. \tag{A.17}$$

Thus, the substitution of eq. $(A.17)$ in eq. $(A.15)$ permits us to reproduce the same calculations as in the previous subsection ant to work out the expression (3.53) for the joint probability between galaxy and cluster distributions.

A.3 Statistics of the exponential threshold

According to the definition (3.8) of N-point joint probability and (3.71) of exponential biased field, we get

$$\begin{aligned}\Pi^{(N)}_{\nu,\mu,\mathrm{R}}(x_1,...x_{\mathrm{N}}) &= \int D[\epsilon(x)]\,P[\epsilon(x)]\prod_{r=1}^{N}\rho_{\nu,\mu,\mathrm{R}}(x_r) = \\ &= (2\pi)^{-N/2}\int_{\mu\sigma_R}^{+\infty}d\alpha_1...\int_{\mu\sigma_{\mathrm{R}}}^{+\infty}d\alpha_{\mathrm{N}}\int_{-\infty}^{+\infty}d\phi_1...\int_{-\infty}^{+\infty}d\phi_{\mathrm{N}}\times \\ &\times \Big\{\prod_{r=1}^{N}(i\phi_r)^l\,\tilde{g}(\phi_r)\,e^{-i\phi_r\alpha_r]}\Big\}\times Z[J^*]\,.\end{aligned} \tag{A.18}$$

In the above equation, the expression for the external source J^*_x is quite different from the previous one and reads

$$J^*(x) = \sum_{r=1}^{N}\Big(\phi_r - i\frac{\nu}{\sigma_{\mathrm{R}}}\Big)\,Q_{\mathrm{R}}(|x-x_r|)\,. \tag{A.19}$$

However, if we make the replacement

$$\phi_r \to \phi_r - i\frac{\nu}{\sigma_{\mathrm{R}}}\,, \tag{A.20}$$

a large part of the calculations given in the previous subsection can be easily reproduced. This leads to the expression

$$\begin{aligned}&\Pi^{(N)}_{\nu,\mu,\mathrm{R}}(x_1,...x_{\mathrm{N}}) = \\ &= (2\pi)^{-N/2}\int_{\mu\sigma_{\mathrm{R}}}^{+\infty}d\alpha_1...\int_{\mu\sigma_{\mathrm{R}}}^{+\infty}d\alpha_{\mathrm{N}}\int_{-\infty}^{+\infty}d\phi_1...\int_{-\infty}^{+\infty}d\phi_{\mathrm{N}}\Big\{\prod_{r=1}^{N}\Big(i\frac{\phi_r}{\sigma_{\mathrm{R}}}\Big)^l e^{h(\phi_r)}\Big\}\times \\ &\times\; exp\Big\{\sum_{n=2}^{\infty}\frac{i^n}{n!}\sum_{[r_n]=1}^{N}\frac{\xi^{(n)}_{con,\mathrm{R}}(x_{r_1},...,x_{r_n})}{\sigma^n_{\mathrm{R}}}\prod_{r=1}^{n}(\phi_r - i\nu)\Big\}\,exp\Big(-i\sum_{r=1}^{N}\alpha_r\phi_r\Big)\,.\end{aligned} \tag{A.21}$$

The expansion of $h(\phi)$ must be performed from the point $i\nu/\sigma_{\rm R}$. Accordingly,

$$\begin{aligned}
&\Pi^{(N)}_{\nu,\mu,{\rm R}}(x_1,...x_{\rm N}) \;= \\
&= (2\pi)^{-N/2}\int_{\mu}^{+\infty} d\alpha_1 ... \int_{\mu}^{+\infty} d\alpha_{\rm N} \int_{-\infty}^{+\infty} d\phi_1 ... \int_{-\infty}^{+\infty} d\phi_{\rm N} \left\{ \prod_{r=1}^{N} \left(-\frac{1}{\sigma_{\rm R}} \frac{\partial}{\partial \alpha_r} \right)^{l} e^{h(i\frac{\nu}{\sigma_{\rm R}})} \right\} \times \\
&\times \; exp\left\{ \sum_{n=1}^{\infty} \frac{(-1)^n}{n!} \sum_{[r_n]=1}^{N} W^{(n)}_{{\rm R},[r_n]} \prod_{r=1}^{n} \left(\frac{\partial}{\partial \alpha_{r_j}} - \nu \right) \right\} \times \\
&\times \; exp\left\{ \sum_{r=1}^{N} \left[-\frac{\nu^2}{2} - \frac{\phi_r^2}{2} - i\phi_r(\alpha_r - \nu) \right] \right\}
\end{aligned} \tag{A.22}$$

where the quantities $W^{(n)}_{{\rm R},[r_n]}$ are defined according to eq. (3.73). Here the substitution

$$\alpha_r \;\rightarrow\; \alpha_r + \nu \tag{A.23}$$

ought to be performed. Using the multinomial expansion theorem in the form

$$\left(-\frac{\partial}{\partial \alpha_r} - \nu \right)^{{\rm m}(r)} \;=\; \sum_{k=0}^{{\rm m}(r)} \frac{{\rm m}(r)!}{k!\,({\rm m}(r)-k)!} \left(-\frac{\partial}{\partial \alpha_r} \right)^{k} (-\nu)^{{\rm m}(r)-k} \tag{A.24}$$

and the cluster expansion, we finally obtain the expression (3.72) for the N-point joint probability of the exponential biased field.

Appendix B

Mass decomposition method in spiral galaxies

This appendix is a brief review of the Persic & Salucci's method [158,159] of mass decomposition to split the observed rotation velocities in spiral galaxies into the contributions of luminous (disk) and dark (halo) matter. We model a spiral galaxy as a stellar disk embedded in a spherical dark halo. We assume that *a)* the stellar surface density, $I_{\rm R}$, follows the exponential thin disk law $I_{\rm R} = I_o e^{-R/R_D}$ ($R_{\rm D}$ is the disk length–scale), and *b)* in the region of interest, between 2.2 and 3.2 disk length–scales, the bulge and the HI disk give negligible contributions to the circular velocity $V(R)$. In this appendix we also assume the relation $R_{opt} = 3.2\ R_{\rm D}$ to hold exactly. No density profile is assumed for the halo.

Taking the first moment of the condition for centrifugal equilibrium,

$$V^2(R) = V_d^2(R) + V_h^2(R) \tag{B.1}$$

[$V_d(R)$ and $V_h(R)$ are the disk and halo contributions to the circular velocity], we obtain

$$V(R)\frac{dV(R)}{dR} = V_d(R)\frac{dV_d(R)}{dR} + V_h(R)\frac{dV_h(R)}{dR}. \tag{B.2}$$

The halo and disk masses within a radius R read

$$M_h(R) = G^{-1}V_h^2(R)\ R \tag{B.3}$$

$$M_d(R) = G^{-1}f_{\rm R}^{-1}V_d^2(R)\ R, \tag{B.4}$$

where $f_{\rm R}$ accounts for the disk's departure from spherical symmetry and is expressed in terms of the modified Bessel functions $I_n(x)$ and $K_n(x)$ as

$$f_{\rm R} = \left[4x^3[I_o(x)\ K_o(x) - I_1(x)\ K_1(x)]\right]\Big|_{x=R/2R_D}. \tag{B.5}$$

For an exponential thin disk [77] it is

$$\frac{d\,logV_d(R)}{d\,logR} = \frac{I_o(x)\ K_o(x) + x\ [I_1(x)\ K_o(x) - I_o(x)\ K_1(x)]}{I_o(x)\ K_o(x) - I_1(x)\ K_1(x)}\Big|_{x=R/2R_D}. \tag{B.6}$$

By combination of the previous expressions, the disk–to–total mass ratio [with $M_t(R) = M_d(R) + M_h(R)$] is

$$\frac{M_d(R)}{M_t(R)} = \left[\frac{dlogV_h(R)}{dlogR} - \frac{dlogV(R)}{dlogR}\right] \times \left[4x^3[I_o(x)\,K_o(x) - I_1(x)\,K_1(x)] \times \right.$$
$$\times \left(\frac{dlogV(R)}{dlogR} - \frac{I_o(x)\,K_o(x) + x[I_1(x)\,K_o(x) - I_o(x)\,K_1(x)]}{I_o(x)\,K_o(x) - I_1(x)\,K_1(x)}\right) +$$
$$\left. + \frac{dlogV_h(R)}{dlogR} - \frac{dlogV(R)}{dlogR}\right]^{-1}\Bigg|_{x=R/2R_D}. \qquad \text{(B.7)}$$

We now compute the mass ratio at R_{opt}. In order to simplify the notation, we also define $M_{halo} \equiv M_h(R_{opt})$, $M_{disk} \equiv M_d(R_{opt})$, $M_{tot} \equiv M_t(R_{opt})$, $\nabla \equiv \left.\frac{dlogV(R)}{dlogR}\right|_{R_{opt}}$ and $\nabla_h \equiv \left.\frac{dlogV_h(R)}{dlogR}\right|_{R_{opt}}$. Then

$$\frac{M_{disk}}{M_{tot}} = \frac{\nabla_h - \nabla}{\nabla_h + 0.1\,\nabla + 0.3} \qquad \text{(B.8)}$$

is a function of the (observed) slope ∇ of the rotation curve, and of the (unknown) slope of the halo velocity field, ∇_h. Even though ∇_h is not directly observable in individual objects, in the case of a *sample* of galaxies we can estimate its sample–averaged value, $\bar{\nabla}_h$, arguing that for such a value the correlation between luminosity and disk mass has the smallest scatter. Let us now assume the relationship

$$log\ L_B = a + b\ log\ M_{disk}, \qquad \text{(B.9)}$$

where M_{disk} is given by

$$M_{disk}(\nabla_h) = G^{-1}V^2(R_{opt})\,\frac{\nabla_h - \nabla}{1.1\,\nabla_h + 0.3}\,R_{opt} \qquad \text{(B.10)}$$

and L_B, ∇, R_{opt} and $V(R_{opt})$ are direct observational quantities. The parameters a, b and ∇_h, instead, are obtained by searching a sample of galaxies for a relationship of the form $(B.9)$ and minimizing the corresponding quantity $\Delta^2 = \sum_i (log\ L_B^i - a - b\ log\ M_{disk}^i(\nabla_h))^2$ with respect to a, b, and ∇_h. We find $\bar{\nabla}_h = 0.8 \pm 0.1$ [158,161], that inserted in eq. $(B.8)$ yields

$$\frac{M_{disk}}{M_{tot}} = \frac{0.8 - \nabla}{0.1\,\nabla + 1.1} \qquad \text{(B.11)}$$

which coincides with eq. (5.6) in the text. (A suitable halo density distribution is, *e.g.*, $\rho(R) = \rho_0/[1 + (R/a)^2]$ with $a \simeq \frac{4}{3}R_{opt} \simeq 4\ R_D$.) Then equation $(B.11)$ allows the decomposition, from the profile of a rotation curve, of the total mass $M_{tot} \simeq G^{-1}V^2(R_{opt})R_{opt}$ into its dark $[M_{dark} \simeq G^{-1}\ V^2(R_{opt})\ R_{opt}\ (0.28 + 0.95\ \nabla)]$ and luminous $[M_{lum} \simeq G^{-1}\ V^2(R_{opt})\ R_{opt}\ (0.72 - 0.95\ \nabla)]$ components. The estimated uncertainty is few percents for $M_{disk}/M_{tot} \simeq 0.7$, and $< 30\%$ for $M_{disk}/M_{tot} \simeq 0.2$ [159].

Appendix C

The moment method

Starting from the analysis of the PS90 sample of rotation curves of spiral galaxies (see Chapter 5), in this appendix we work out the values (5.28) of (suitable combinations of) the hierarchical coefficients for correlation functions between galaxies and background matter, by means of the moment method [see eqs. (5.24), (5.25) and (5.26)].

C.1 Analysis of the three-point function.

At the third–order in the correlation analysis, the hierarchical expression (2.23) contains summations over only one *tree* and 3 total terms. Thus

$$\xi^{(3)}_{012} = Q\,[\xi_{01}\xi_{02} + \xi_{10}\xi_{12} + \xi_{20}\xi_{21}] \tag{C.1}$$

with obvious meaning of the two-point functions' indices. Inserting eq. $(C.1)$ into eq. (5.24) and also taking into account the disconnected terms, it easy to show that

$$\begin{aligned} < M^2 >_{\rm R} &= \rho^2 \int_0^R \delta V_1 \int_0^R \delta V_2 \times \\ &\times \; [1 + \xi_{r_1} + \xi_{r_2} + \xi_{r_{12}} + Q\,(\xi_{r_1}\xi_{r_2} + \xi_{r_1}\xi_{r_{12}} + \xi_{r_2}\xi_{r_{12}})]\,, \end{aligned} \tag{C.2}$$

where $r_{12} = |\mathbf{r}_1 - \mathbf{r}_2|$. On the other hand,

$$< M >^2_{\rm R} = \rho^2 \int_0^R \delta V_1 \int_0^R \delta V_2 [1 + \xi_{r_1} + \xi_{r_2} + \xi_{r_1}\xi_{r_2}]\,. \tag{C.3}$$

By averaging eqs. $(C.2)$ and $(C.3)$ over the k-th bin and taking eq. (5.24) with $n = 2$, and including only ξ^2 terms (in the $\xi \gg 1$ regime), we get

$$\frac{< M^2 >_k}{< M >^2_k} = Q + 2\,Q\,\frac{K_2}{K_1^2}\,. \tag{C.4}$$

The quantity K_2 is

$$K_2 = \left(\frac{3}{4\pi}\right)^2 \int_0^1 d^3x_1 \int_0^1 d^3x_2 (x_1 x_{12})^{-\gamma} . \qquad (C.5)$$

The multiple integral in eq. $(C.5)$ can be evaluated numerically and the value it takes for $\gamma = 1.71$ is reported in Table C.1. The fit to eq. $(C.4)$ with the observational $s_k^{(2)}$ values gives

$$Q = 0.43 \pm 0.02. \qquad (C.6)$$

The error in eq. $(C.6)$ corresponds to one formal standard deviation.

C.2 Analysis of the four-point function.

In this case, the hierarchical pattern (2.23) provides summations over two different *trees*, corresponding to two different amplitudes $R_a \equiv Q_{3,1}$ and $R_b \equiv Q_{3,2}$, and 16 total terms. Then:

$$\xi^{(4)}_{0123} = R_a\Big[\xi_{01}\xi_{12}\xi_{23} + \ldots \Big(12 \quad \sqsupset \quad terms\Big)\Big] + \\ + R_b\Big[\xi_{01}\xi_{02}\xi_{03} + \ldots \Big(4 \quad \angle \quad terms\Big)\Big]. \qquad (C.7)$$

By averaging eq. (5.24) over the k-th bin, for $n = 3$ we deduce

$$\left\langle \left(\frac{M}{\bar{M}_k}\right)^3 \right\rangle_k = \left[6\, R_a\left(\frac{K_{3a}}{K_1^3} + \frac{K_2}{K_1^2}\right) + R_b\left(1 + 3\,\frac{K_{3b}}{K_1^3}\right)\right] \left(\frac{< M >_k}{\bar{M}_k}\right)^3 . \qquad (C.8)$$

The constants K_{3a} and K_{3b} come from the triple three–dimensional integration in eq. (5.24). Their full expressions are:

$$K_{3a} = \left(\frac{3}{4\pi}\right)^3 \int_0^R d^3x_1 \int_0^R d^3x_2 \int_0^R d^3x_3 (x_1 x_{12} x_{23})^{-\gamma}$$
$$K_{3b} = \left(\frac{3}{4\pi}\right)^3 \int_0^R d^3x_1 \int_0^R d^3x_2 \int_0^R d^3x_3 (x_1 x_{12} x_{13})^{-\gamma} , \qquad (C.9)$$

and their numerical values are reported in Table C.1.

Comparison between the left hand sides of eqs. (5.24), as can be deduced from the data, and $(C.9)$ allows us to obtain the value of a suitable combination of R_a and R_b. We find

$$R_a + 0.356\, R_b = 0.175 \pm 0.015 . \qquad (C.10)$$

Table C.1
Integrals for higher–order moments[1]

$n = 2:$	$K_1 = (\frac{3}{4\pi}) \int_0^1 d^3x_1\, x_1^{-\gamma}$	$= 1.326$
$n = 3:$	$K_2 = (\frac{3}{4\pi})^2 \int_0^1 d^3x_1 \int_0^1 d^3x_2 (x_1 x_{12})^{-\gamma}$	$= 4.531$
$n = 4:$	$K_{3a} = (\frac{3}{4\pi})^3 \int_0^1 d^3x_1 \int_0^1 d^3x_2 \int_0^1 d^3x_3 (x_1 x_{12} x_{23})^{-\gamma}$	$= 8.992$
	$K_{3b} = (\frac{3}{4\pi})^3 \int_0^1 d^3x_1 \int_0^1 d^3x_2 \int_0^1 d^3x_3 (x_1 x_{12} x_{13})^{-\gamma}$	$= 9.696$
$n = 5:$	$K_{4a} = (\frac{3}{4\pi})^4 \int_0^1 d^3x_1 ... \int_0^1 d^3x_4 (x_1 x_{12} x_{13} x_{14})^{-\gamma}$	$= 18.410$
	$K_{4b} = (\frac{3}{4\pi})^4 \int_0^1 d^3x_1 ... \int_0^1 d^3x_4 (x_1 x_{12} x_{23} x_{24})^{-\gamma}$	$= 15.836$
	$K_{4c} = (\frac{3}{4\pi})^4 \int_0^1 d^3x_1 ... \int_0^1 d^3x_4 (x_1 x_{12} x_{13} x_{34})^{-\gamma}$	$= 16.762$
	$K_{4d} = (\frac{3}{4\pi})^4 \int_0^1 d^3x_1 ... \int_0^1 d^3x_4 (x_1 x_{12} x_{23} x_{34})^{-\gamma}$	$= 11.358$
$n = 6:$	$K_{5a} = (\frac{3}{4\pi})^5 \int_0^1 d^3x_1 ... \int_0^1 d^3x_5 (x_1 x_{12} x_{13} x_{14} x_{15})^{-\gamma}$	$= 38.245$
	$K_{5b} = (\frac{3}{4\pi})^5 \int_0^1 d^3x_1 ... \int_0^1 d^3x_5 (x_1 x_{12} x_{23} x_{24} x_{25})^{-\gamma}$	$= 30.441$
	$K_{5c} = (\frac{3}{4\pi})^5 \int_0^1 d^3x_1 ... \int_0^1 d^3x_5 (x_1 x_{12} x_{13} x_{14} x_{45})^{-\gamma}$	$= 34.691$
	$K_{5d} = (\frac{3}{4\pi})^5 \int_0^1 d^3x_1 ... \int_0^1 d^3x_5 (x_1 x_{12} x_{13} x_{34} x_{35})^{-\gamma}$	$= 31.684$
	$K_{5e} = (\frac{3}{4\pi})^5 \int_0^1 d^3x_1 ... \int_0^1 d^3x_5 (x_1 x_{12} x_{23} x_{24} x_{25})^{-\gamma}$	$= 28.883$
	$K_{5f} = (\frac{3}{4\pi})^5 \int_0^1 d^3x_1 ... \int_0^1 d^3x_5 (x_1 x_{12} x_{23} x_{14} x_{45})^{-\gamma}$	$= 30.723$
	$K_{5g} = (\frac{3}{4\pi})^5 \int_0^1 d^3x_1 ... \int_0^1 d^3x_5 (x_1 x_{12} x_{23} x_{34} x_{35})^{-\gamma}$	$= 27.800$
	$K_{5h} = (\frac{3}{4\pi})^5 \int_0^1 d^3x_1 ... \int_0^1 d^3x_5 (x_1 x_{12} x_{13} x_{34} x_{45})^{-\gamma}$	$= 30.358$
	$K_{5i} = (\frac{3}{4\pi})^5 \int_0^1 d^3x_1 ... \int_0^1 d^3x_5 (x_1 x_{12} x_{23} x_{34} x_{45})^{-\gamma}$	$= 27.204$

[1] Such values of the integrals correspond to $\gamma = 1.71$.

C.3 Analysis of the five-point function.

For $n = 5$, the hierarchical expression (2.23) gets rather cumbersome. By using the helpful graph technique (see Figure 2.1), the contributions from the three different *trees* and 125 total terms can be written as

$$\begin{aligned}
\xi^{(5)}_{0\ldots4} &= Q_{5,1}\Big[\xi_{01}\xi_{02}\xi_{03}\xi_{04} + \ldots \Big(5 \quad \times \quad terms\Big)\Big] + \\
&+ Q_{5,2}\Big[\xi_{01}\xi_{12}\xi_{23}\xi_{24} + \ldots \Big(60 \quad \text{⊢} \quad terms\Big)\Big] + \\
&+ Q_{5,3}\Big[\xi_{01}\xi_{12}\xi_{23}\xi_{34} + \ldots \Big(60 \quad \text{Z} \quad terms\Big)\Big]. \qquad \text{(C.11)}
\end{aligned}$$

In the right hand side of eq. (C.11) the first contribution comes from *star graphs*, while the last one comes from *snake graphs*. The middle term takes into account the presence of one differently *rooted* tree. In this case too, we substitute eq. (C.11) in (5.24) and obtain the fourth *moment* of the mass distribution:

$$\begin{aligned}
\left\langle\left(\frac{M}{\bar{M}_k}\right)^4\right\rangle_k &= \left[Q_{5,1}\left(1 + 4\frac{K_{4a}}{K_1^4}\right) + 12Q_{5,2}\left(\frac{K_2}{K_1^2} + \frac{K_{3b}}{K_1^3} + \frac{K_{4b}}{K_1^4} + 2\frac{K_{4c}}{K_1^4}\right) + \right. \\
&+ \left. 12Q_{5,3}\left(\frac{K_2^2}{K_1^4} + 2\frac{K_{3a}}{K_1^3} + 2\frac{K_{4d}}{K_1^4}\right)\right]\left(\frac{< M >_k}{\bar{M}_k}\right)^4. \qquad \text{(C.12)}
\end{aligned}$$

The four K_4 quantities come from the quadruple volume integration occurring in the computation of $< M^4 >_k$. Their full expressions and numerical values are reported in Table C.1. Following the same pattern as in the previous sub–sections, we compare eq. (C.12) with observational data. In this case, the combination of the Q_5's reads

$$Q_{5,1} + 11.43Q_{5,2} + 9.90Q_{5,3} = 0.675 \pm 0.107. \qquad \text{(C.13)}$$

Eq. (C.13) is relevant because it represent one of the very first pieces if information on fifth-order correlation. Indeed, there is strong evidence for the hierarchical pattern to hold up to the fifth order, with a $\sim 6\,\sigma$ signal.

C.4 Analysis of the six-point function.

The growth of the number of terms to be added in eq. (2.23) leads us to consider, for n=6, contributions from six different *trees* and 1296 total terms. Then, the expression of the six-point correlation function is

$$\begin{aligned}
\xi^{(5)}_{0\ldots5} &= Q_{6,1}\Big[\xi_{01}\xi_{02}\xi_{03}\xi_{04}\xi_{05} + \ldots \Big(6 \quad \text{✳} \quad terms\Big)\Big] + \\
&+ Q_{6,2}\Big[\xi_{01}\xi_{12}\xi_{23}\xi_{24}\xi_{25} + \ldots \Big(120 \quad \text{Y} \quad terms\Big)\Big] + \\
&+ Q_{6,3}\Big[\xi_{01}\xi_{12}\xi_{13}\xi_{34}\xi_{35} + \ldots \Big(90 \quad \text{⊥} \quad terms\Big)\Big] +
\end{aligned}$$

$$+\ Q_{6,4}\Big[\xi_{01}\xi_{12}\xi_{23}\xi_{24}\xi_{45}\ +\ \ldots\ \Big(360\ \ \textit{terms}\Big)\Big]\ +$$
$$+\ Q_{6,5}\Big[\xi_{01}\xi_{12}\xi_{23}\xi_{34}\xi_{35}\ +\ \ldots\ \Big(360\ \ \textit{terms}\Big)\Big]\ +$$
$$+\ Q_{6,6}\Big[\xi_{01}\xi_{12}\xi_{23}\xi_{34}\xi_{45}\ +\ \ldots\ \Big(360\ \ \textit{terms}\Big)\Big]\,. \qquad \text{(C.14)}$$

Due to the complexity of such expression, the form of the fifth moment of the mass distribution does not look friendly. In fact

$$\begin{aligned}\left\langle\left(\frac{M}{\bar{M}_k}\right)^5\right\rangle_k \ =\ & \Big[Q_{6,1}\Big(1+5\frac{K_{5a}}{K_1^4}\Big)+20Q_{6,2}\Big(\frac{K_2}{K_1^2}+\frac{K_{4a}}{K_1^4}+\frac{K_{5b}}{K_1^5}+3\frac{K_{5c}}{K_1^5}\Big)\ + \\ +\ & 30Q_{6,3}\Big(\frac{K_{3b}}{K_1^3}+2\frac{K_{5d}}{K_1^5}\Big)+60Q_{6,4}\Big(\frac{K_2^2}{K_1^4}+2\frac{K_{4c}}{K_1^4}+2\frac{K_{5e}}{K_1^5}+\frac{K_{5f}}{K_1^5}\Big)\Big]\ + \\ +\ & 60Q_{6,5}\Big(\frac{K_{3a}}{K_1^3}+\frac{K_2K_{3b}}{K_1^5}+\frac{K_{4d}}{K_1^4}+\frac{K_{5g}}{K_1^5}+2\frac{K_{5h}}{K_1^5}\Big)\ + \\ +\ & 120Q_{6,6}\Big(\frac{K_2K_{3a}}{K_1^5}+\frac{K_{4d}}{K_1^4}+\frac{K_{5i}}{K_1^5}\Big)\Big]\left(\frac{<M>_k}{\bar{M}_k}\right)^5. \qquad \text{(C.15)}\end{aligned}$$

Expressions and numerical values of the K_5 coefficients are given in Table C.1.

By fitting the data on central moments to eq. (C.15), we get

$$Q_{6,1}+18.06Q_{6,2}+13.79Q_{6,3}+49.50Q_{6,4}+47.96Q_{6,5}+43.59Q_{6,6}\ =$$
$$=\ 0.44\pm0.12\,. \qquad \text{(C.16)}$$

Similarly to eq. (C.13), eq. (C.16) is important in view of the paucity of data on sixth-order correlation. In this case again the hierarchical pattern shows up with a $4\,\sigma$ signal.

Bibliography

[1] Abell, G.O., 1958, *Ap. J. Suppl.*, **3**, 211.

[2] Abell, G.O., 1961, *A. J.*, **66**, 607.

[3] Abell, G.O., Corwin, H.G., and Olowin, R.P., 1989, *Ap. J. Suppl.*, **70**, 1.

[4] Albrecht, A., and Turok, N., 1989, *Phys. Rev.* **D40**, 973.

[5] Allen, T.J., Grinstein, B., and Wise, M.B., 1987, *Phys. Lett. B* **197**, 66.

[6] Bahcall, N.A., 1979, *Ap. J*, **232**, 689.

[7] Bahcall, N.A., 1988, *Ann. Rev. Astr. Ap.*, **26**, 631.

[8] Bahcall, N.A., and Burgett, W.S., 1986, *Ap. J. (Letters)*, **300**, L35.

[9] Bahcall, N.A., and Soneira, R.M., 1983, *Ap. J.*, **270**, 20.

[10] Bahcall, N.A., and Soneira, R.M., 1984, *Ap. J.*, **277**, 27.

[11] Bardeen, J.M., Bond, J.R., Kaiser, N., and Szalay, A.S., 1986, *Ap. J.* **304**, 15.

[12] Bardeen, J.M., Steinhardt, P.J., and Turner, M.S., 1983, *Phys. Rev.* **D28**, 679.

[13] Batuski, D.J., Bahcall, N.A., Olowin, R.P., and Burns, J.O., 1989, *Ap. J.*, **341**, 599.

[14] Bean, A.J., *et al.*, 1983, *M.N.R.A.S.*, **205**, 605.

[15] Begeman, K., 1988, *Ph.D.* thesis, Groningen.

[16] Bennet, D.P., and Bouchet, F.E., 1989, *Phys. Rev. (Letters)* **60**, 257.

[17] Bertschinger, E., and Dekel, A., 1989, *Ap. J. (Letters)*, **336**, L5.

[18] Bertschinger, E., Dekel, A., Faber, S.M., and Dressler, A., 1990, *preprint.*

[19] Blumenthal, G.R., 1987, *Theoretical Advanced Studies Insitute*, ed. R. Slansky (World Scientific Publishing Company).

[20] Blumenthal, G.R., Faber, S.M., Primack, J.R., and Rees, M.J. 1984, *Nature*, **311**, 517.

[21] Bogart, R.S., and Wagoner, R.V., 1973, *Ap. J. (Letters)*, **181**, 609.

[22] Bond, J.R., and Efstathiou, G., 1984, *Ap. J. (Letters)* **285**, L45.

[23] Bond, J.R., and Szalay, A.S., 1983, *Ap. J.* **274**, 443.

[24] Bonometto, S.A., Borgani, S., 1989, *Durham Symposium on the Epoch of Galaxy Formation.*

[25] Bonometto, S.A., Borgani, S., Persic, M., and Salucci, P., 1990, *Ap. J.*, **356**, 350.

[26] Bonometto, S.A., Lucchin, F., and Matarrese, S., 1987, *Ap. J.*, **323**, 19.

[27] Bonometto, S.A., and Masiero, A., 1985, *Rivista del Nuovo Cimento* **9**, 5.

[28] Bonometto, S.A., and Scaramella, R., 1988, unpublished.

[29] Borgani, S., 1990, *Astr. Ap.*, in press.

[30] Borgani, S., and Bonometto, S.A., 1989, *Astr. Ap.*, **215**, 17.

[31] Borgani, S., and Bonometto, S.A., 1990. *Ap. J.*, **338**, 398.

[32] Borgani, S., Bonometto, S.A., Persic, M., and Salucci, P., 1990, *Ap. J.*, in press.

[33] Borgani, S., Bonometto, S.A., Persic, M., and Salucci, P., 1990, *Proceedings of the Moriond Astrophysics Meeting*, in press.

[34] Börner, G., *The Early Universe*, (Berlin: Springer Verlag).

[35] Börner, G., Mo, H.J.,and Zhou, Y., 1989, *Astr. Ap.*, **221**, 191.

[36] Börner, G., and Mo, H.J., 1990, *Astr. Ap.*, **227**, 324.

[37] Bosma, A., 1981, *A. J.*, **86**, 1825.

[38] Broadhurst, T.J., Ellis, R.S., Koo, D.C., and Szalay, A.S., 1990, *Nature*, **343**, 726.

[39] Burstein, D., 1990, *Rep. Progr. Phys.*, **53**, 421.

[40] Carignan, C., and Freemen, K.C., 1988, *Ap. J. (Letters)*, **332**, L33.

[41] Carignan, C., Sancisi, R., and van Albada, 1988, *A. J.*, **95**, 37.

[42] Carr, B.J., Bond, J.R., and Arnett, W.D., 1984, *Ap. J.*, **277**, 445.

[43] Cavaliere, A., Santangelo, P., Tarquini, G., and Vittorio, N., 1986, *Ap. J.*, **305**, 651.

[44] Centrella, J., and Melott, A., 1983, *Nature*, **305**, 196.

[45] Colafrancesco, S., Lucchin, F., and Matarrese, S., 1989, *Ap. J.*, **345**, 3.

[46] Cole, S., and Kaiser, N., 1989, *M.N.R.A.S.*, **237**, 1127.

[47] Coles, P., 1988, *M.N.R.A.S.*, **238**, 319.

[48] da Costa, L.N., *et al.*, 1989, *A. J.*, **97**, 315.

[49] Davis, M., Efstathiou, G., Frenk, C.S., and White, S.D.M., 1985, *Ap. J.*, **292**, 371.

[50] Davis, M., and Geller, M.J., 1976, *Ap. J.* **208**, 13.

[51] Davis, M., and Huchra, J., 1982, *Ap. J.* **254**, 437.

[52] Davis, M., and Peebles, P.J.E., 1983, *Ap. J.* **267**, 465.

[53] Davis, M., and Peebles, P.J.E., 1977, *Ap. J. Suppl.* **35**, 425.

[54] Dekel, A., 1987, *Observational Cosmology*, ed. A.Hewitt, G.Burbidge, and L.Z.Fang (Dordrecht:Reidel), p.145.

[55] Dekel, A., and Aarseth, S.J., 1984, *Ap. J.*, **238**, 1.

[56] Dekel, A., Blumenthal, G.R., Primack, J.R., and Olivier, S., 1989, *Ap. J. (Letters)*, **338**, L5.

[57] Dekel, A., and Rees, M.J., 1987, *Nature*, **326**, 455.

[58] Dekel, A., and Silk, J., 1986, *Ap. J.*, **303**, 39.

[59] de Lapparent, V., Geller, M.J., and Huchra, J.P., 1986, *Ap. J. (Letters)*, **302**, L1.

[60] de Lapparent, V., Geller, M.J., and Huchra, J.P., 1988, *Ap. J.*, **332**, 44.

[61] de Lapparent, V., Geller, M.J., and Huchra, J.P., 1989, *Ap. J.*, **343**, 1.

[62] de Vaucoleurs, G., de Vaucoleurs, G., 1964, *Reference Catalogue of Bright Galaxies*, (Austin: University of Texas Press).

[63] Doroshkevich, A.G., Khlopov, M.Y., Sunyaev, R.A., Szalay, A.S., and Zel'dovich, Y.B., 1981, *Proceedings of the Tenth Texas Symposium on Relativistic Astrophysics*, ed. R. Ramaty and F.C. Jones, Annals of the New York Academy of Sciences Vol. 375 (New York Academy of Sciences: New York), p. 32.

[64] Doroshkevich, A.G., and Shandarin, S.F., 1974, *Astr. Zh.* **51**, 41.

[65] Dressler, A., 1980, *Ap. J.*, **236**, 351.

[66] Efstathiou, G., Davis, M., Frenk, C.S., and White, S.D.M., 1985, *Ap. J. Suppl.*, **57**, 241.

[67] Einasto, J., Klypin, A.A., Saar, E., and Shandarin, S.F., 1984, *M.N.R.A.S.*, **206**, 529.

[68] Einasto, J., Klypin, A.A., and Saar, E., 1986, *M.N.R.A.S.*, **219**, 457.

[69] Ellis, J., Hagelin, J.S., Nanopulos,D.V., Olive, K., and Srednicki, M, 1984, *Nucl. Phys. B* **238**, 453.

[70] Faber, S.M., and Gallagher, J.S., 1979, *Ann. Rev. Astr. Ap.*, **17**, 135.

[71] Faber, S.M., and Jackson, R.E., 1976, *Ap. J.*, **204**, 668.

[72] Fall, S.M., 1975, *M.N.R.A.S.*, **172**, 23P.

[73] Fall, S.M., and Tremaine, S., 1977, *Ap. J.* **216**, 682.

[74] Felten, J.E., 1985, *Comm. Ap. Sp. Sci.*, **11**, 53.

[75] Field, G.B., and Saslaw, W.C., 1971, *Ap. J.*, **176**, 199.

[76] Forman, W., and Jones, C., 1982, *Ann. Rev. Ap.*, **20**, 547.

[77] Freeman, K.C., 1970, *Ap. J.*, **160**, 811.

[78] Frenk, C.S., White, S.D.M., and Davis, M., 1983, *Ap. J.*, **271**, 417.

[79] Fry, J.N., 1982, Ap. J. **262**, 425.

[80] Fry, J.N., 1984, *Ap. J. (Letters)* **277**, L5.

[81] Fry, J.N., 1984, *Ap. J.* **279**, 499.

[82] Fry, J.N., and Peebles, P.J.E., 1978, *Ap. J.* **221**, 19.

[83] Geller, M.J., 1987, *Large Scale Structure in the Universe*, Proceedings of the SAAS–FEE School, ed. L. Martinet and M. Mayor, Geneva: Geneva Observatory, p.71.

[84] Geller, M.J., de Lapparent, V., and Huchra, J., 1987, *I.A.U. Symposium 124, Observational Cosmology*, ed. Hewitt *et al.* (Dordrecht:Reidel), p.301.

[85] Geller, M.J., and Huchra, J.P., 1988, *Large-Scale Motions in the Universe*, ed. V.C. Rubin & G.V. Coyne (Princeton: Princeton University Press), p.3.

[86] Geller, M.J., and Huchra, J.P., 1989, *Science*, **246**, 897.

[87] Geller, M.J., and Peebles, P.J.E., 1973, *Ap. J.*, **184**, 329.

[88] Giovannelli, R., 1983, *IAU Symposium 104, Early Evolution of the Universe and its Present Structure*, ed. G.O. Abell and G.L. Chincarini (Dordrecht: Reidel), p.273.

[89] Giovannelli, R., Haynes, M.P., and Chincarini, G.L., 1986, *Ap. J.*, **300**, 77.

[90] Gott III, J.R., Gunn, J.E., Schramm, D.N., and Tinsley, B.M., 1974 , *Ap. J.*, **194**, 543.

[91] Gott III, J.R., and Rees, M.J., 1975, *Astr. Ap.*, **45**, 365.

[92] Gott III, J.R., and Turner, E.L., 1976 , *Ap. J.*, **209**, 1.

[93] Gott III, J.R., and Turner, E.L., 1977 , *Ap. J.*, **216**, 357.

[94] Gott III, J.R., and Turner, E.L., 1979 , *Ap. J. (Letters)*, **232**, L79.

[95] Grinstein, B., and Wise, M.B., 1986, *Ap. J.*, **310**, 19.

[96] Grishcuk, L.P. and Zel'dovich, Y.B., 1981, *Astron. Zh.* **58**, 472.

[97] Groth, E.J., and Peebles, P.J.E., 1977 , *Ap. J.*, **217**, 385.

[98] Gunn, J.E., and Gott III, J.R., 1972 , *Ap. J.*, **176**, 1.

[99] Guth, A., 1981, *Phys. Rev. D*, **23**, 347.

[100] Hamilton, A.J.S., 1988, *Ap. J.* **332**, 67.

[101] Harrison, E.R., 1970, *Phys. Rev. D* **1**, 2726.

[102] Hauser, M.G., and Peebles, P.J.E., 1973 , *Ap. J.*, **185**, 757.

[103] Haynes, M.P., and Giovannelli, R., *Ap. J. (Letters)*, **306**, L55.

[104] Hawking, S.W., and Ellis, G.F.R., 1980, in *The Large Scale Structure of Space-Time*, (Cambridge: Cambridge University Press).

[105] Hoessel, J.G, Gunn, J.E., and Thuan, T.X., 1980 , *Ap. J.*, **241**, 486.

[106] Huchra, J.P., Davis, M., Latham, D., and Tonry, J., 1983 *Ap. J. Suppl.*, **52**, 89.

[107] Huchra, J.P., and Geller, M.J., 1982, *Ap. J.*, **257**, 423.

[108] Huchra, J.P., Geller, M.J., de Lapparent, V., and Corwin, H.G.Jr., 1990 *Ap. J. Suppl.*, **72**, 433.

[109] Ikeuchi, S., 1981, *Pub. Astr. Soc. Japan*, **33**, 211.

[110] Jensen, L.G., and Szalay, A.S., 1986, *Ap.J. (Letters)*, **305**, L5.

[111] Jing, Y.P., and Valdarnini, R., 1990, *preprint.*

[112] Kaiser, N., 1984, *Ap. J. (Letters)*, **284**, L9.

[113] Kaiser, N., and Davis, M., 1985, *Ap. J.*, **297**, 365.

[114] Kirkwood, J.C., 1935, *J. Chem. Phys.* **3**, 300.

[115] Kirshner, R.P., Oemler, A., Jr., Schechter, P.L., and Shechtman, S.A., 1981, *Ap. J. (Letters)*, **248**, L57.

[116] Kirshner, R.P., Oemler, A., Jr., Schechter, P.L., and Shechtman, S.A., 1983, *A. J.*, **88**, 1285.

[117] Kofman, L.A., and Linde, A.D., 1935, *Nucl. Phys.* **B282**, 555.

[118] Klypin, A.A., and Kopilov, A.I., 1983, *Soviet. Astron. Letters.*, **9**, 41.

[119] Lake, G., and Tremaine, S., 1980, *Ap. J. (Letters)*, **238**, L13.

[120] Lauberts, A., 1982, *The ESO/Uppsala Survey of the ESO(B) Atlas* (München:European Southern Observatory).

[121] Lilje, P.B., and Efstathiou, G., 1988, *M.N.R.A.S.*, **231**, 635.

[122] Limber, D.N., 1953, *Ap. J.* **117**, 134.

[123] Linde, A., 1982, *Phys. Lett. B* **108**, 389.

[124] Linde, A., 1984, *Rep. Prog. Phys.* **47**, 925.

[125] Lucchin, F., 1989, *Proceeding of the XI-th Crakow Summer School of Cosmology.*

[126] Lucchin, F., Matarrese, S., 1985, *Phys. Rev. D* **32**, 1316.

[127] Lucchin, F., and Matarrese, S., 1988, *Ap. J.*, **330**, 535.

[128] Lugger, P.M., 1989, *Ap. J.*, **343**, 572.

[129] Maddox, S.J., Efstathiou, G., Sutherland, W.J., and Loveday, J., 1990, *M.N.R.A.S.*, **242**, 43.

[130] Maia, M.A.G., and Nicolaci da Costa, L., 1990, *preprint.*

[131] Martinez, V.J., and Jones, B.J.T., 1990, *M.N.R.A.S.*, **242**, 517.

[132] Martinez–Gonzalez, E., and Sanz, J.L., 1988, *Ap. J.*, **324**, 653.

[133] Martinez–Gonzalez, E., and Sanz, J.L., 1988, *Ap. J.*, **332**, 89.

[134] Matarrese, S., Lucchin, F., and Bonometto, S.A., 1986, *Ap. J. (Letters)* **310**, L21.

[135] Melott, A.L., and Fry, J.N., 1986, *Ap. J.*, **305**, 1.

[136] Messina, A., Moscardini, L., Lucchin, F., and Matarrese, S., 1990, *M.N.R.A.S.*, **345**, 344.

[137] Meszaros, P., 1974, *Astr. Ap.* **37**, 225.

[138] Münster, A., 1969, *Statistical Thermodynamics*, (Springer Verlag: Berlin).

[139] Nicolaci da Costa *et al.*, 1988, *Ap. J.*, **327**, 544.

[140] Nilson, P., 1973, *Uppsala General Catalogue of Galaxies, Nova Acta, Reg. Soc. Sci. Upsaliensis*, Ser. V: A, Vol.**1**.

[141] Oemler, A., 1974, *Ap. J.*, **194**, 1.

[142] Occhionero, F., and Scaramella, R., 1988, *Astr. Ap.*, **204**, 3.

[143] Olivier, S., Bumenthal, G.R., Dekel, A., Primack, J.R., and Stanhill, D., 1990, *Ap. J.*, **356**, 1.

[144] Ortolan, A., Lucchin, F., and Matarrese, S., 1989, *Phys. Rev. D* **40**, 290.

[145] Ostriker, J.P., and Cowie, L., 1981, *Ap. J. (Letters)* **243**, L127.

[146] Peackock, J., 1990, *Contribution Paper at the 10^{t}h Moriond Astrophysics Meeting*, in press.

[147] Peackock, J., and Heavens, A., 1985, *M.N.R.A.S.*, **217**, 805.

[148] Peebles, P.J.E., 1975, *Ap. J.*, **196**, 647.

[149] Peebles, P.J.E., 1976, *Ap. J. (Letters)*, **205**, L109.

[150] Peebles, P.J.E., 1976, *Ap. and Space Sci.*, **45**, 3.

[151] Peebles, P.J.E., 1980, *The Large Scale Structure of the Universe*, (Princeton: Princeton University Press).

[152] Peebles, P.J.E., 1982, *Ap. J.* **258**, 415.

[153] Peebles, P.J.E., 1982, *Ap. J. (Letters)* **263**, L1.

[154] Peebles, P.J.E., 1984, *Ap. J.* **277**, 470.

[155] Peebles, P.J.E., 1986, *Nature*, **321**, 27.

[156] Peebles, P.J.E., and Groth, E.J., 1975, *Ap. J.*, **196**, 1.

[157] Peebles, P.J.E., and Hauser, M.G., 1974, *Ap. J. Suppl.*, **28**, 19.

[158] Persic, M., and Salucci, P., 1988, *M.N.R.A.S.*, **234**, 131.

[159] Persic, M., and Salucci, P., 1990, *Ap. J.*, in press.

[160] Persic, M., and Salucci, P., 1990, *Ap. J.*, in press.

[161] Persic, M., and Salucci, P., 1990, *M.N.R.A.S.*, in press.

[162] Pietronero, L., *Physica*, 1987, **144A**, 257.

[163] Pokorski, S., *Gauge Field Theories*, (Cambridge: Cambridge University Press).

[164] Politzer, D., and Wise, M., 1984, *Ap. J. Letters)* **285**, L1.

[165] Postman, M., Geller, M.J., and Huchra, J.P., 1986, *A. J.*, **91**, 1267.

[166] Preskill, J., Wise, M., and Wilczek, F., 1983, *Phys. Lett.* **120B**, 127.

[167] Press, W.H., and Schechter, P., 1974, *Ap. J.*, **187**, 425.

[168] Primack, J.R., and Blumenthal, G.R., 1983, in *Fourth Workshop on Grand Unification*, ed H.A. Weldon, P. Langacker, P.J. Steinhardt (Boston: Birkhauser) p. 256.

[169] Ramella, M., Geller, M.J., and Huchra, J.P., 1989, *Ap. J.*, **344**, 57.

[170] Ramella, M., Geller, M.J., and Huchra, J.P., 1990, *Ap. J.*, **353**, 51.

[171] Rees, M.J., and Ostricker, J.P., 1977, *M.N.R.A.S.*, **179**, 541.

[172] Riordan, J., 1958, *An Introduction to Combinatorial Analysis*, (New York:Wiley).

[173] Rood, H.J., 1976, *Ap. J.*, **207**, 16.

[174] Rubin, V.C., Ford, W.K., Thonnard, N., and Burstein, D., 1982, *Ap. J.*, **261**, 439.

[175] Rubin, V.C., Burstein, D., Ford, W.K., and Thonnard, N., 1985, *Ap. J.*, **289**, 81.

[176] Rudnicky, K., Dworak, T.Z., Flin, P., Baranovski, B., and Sendrakowski, A., 1973, Acta Cosmologica **1**, 7.

[177] Saarinen, S., Dekel, A., and Carr, B., 1987, *Nature*, **325**, 598.

[178] Salucci, P., Bonometto, S.A., Borgani, S., and Persic, M., 1990, in preparation.

[179] Schaeffer, R., and Silk, J., 1985, *Ap. J.*, **292**, 319.

[180] Schechter, P., 1976, *Ap. J.*, **203**, 297.

[181] Schectman, S., *Ap. J. Suppl.*, **57**, 77.

[182] Seldner, M., and Peebles, P.J.E., 1977, *Ap. J.*, **215**, 703.

[183] Shane, C.D., Wirtanen, C.A., 1967, Publ. Lick Obs., vol.22.

[184] Sharp, N., Bonometto, S.A., and Lucchin, F., 1984, *Astr. Ap.* **130**, 79.

[185] Silk, J., Szalay, A.S., and Zel'dovich, Y.B., 1983, *Sci. Am.* **249**, N. 4, 72.

[186] Struble, M.F., and Rood, H.J., 1987, *Ap. J. Suppl.* **63**, 543.

[187] Sutherland, W., 1988, *M.N.R.A.S.*, **234**, 159.

[188] Sutherland, W., and Efsthatiou, G., 1990, preprint.

[189] Szalay, S.A., 1988, *Ap. J.*, **333**, 21.

[190] Szalay, A.S., and Schramm, D.M., 1985, *Nature*, **314**, 718.

[191] Szapudi, I., Szalay, A.S., and Boschan, P., 1990, *P.A.S.P.*, in press.

[192] Toth, G., Hollosi, J., and Szalay, A.S., 1989, *Ap. J.*, **344**, 75.

[193] Totsuji, H., and Kihara, T., 1969, *Publ. Astron. Soc. Japan*, **25**, 287.

[194] Turner, E.L., and Gott III, J.R., 1976, *Ap. J. Suppl.*, **32**, 409.

[195] Tully, R.B., 1982, *Ap. J.*, **257**, 389.

[196] Tully, R.B., and Fisher, 1977, *Astr. Ap.*, **54**, 661.

[197] Turok, N., 1986, *Cosmology, Astronomy and Fundamental Physics*, ed. G. Setti and L. Van Hove (ESO, Garching bei München), p. 175 .

[198] Valdarnini, R., and Borgani, S., 1990, *M.N.R.A.S.*, submitted.

[199] van Albada, T.S., Bahcall, J.N., Begeman, K., and Sancisi, R., 1985, *Ap. J.*, **295**, 305.

[200] van der Kruit, P.C., 1987, *Astr. Ap.*, **173**, 59.

[201] Vilenkin, A., 1985, *Phys. Rep.* **121**, 265.

[202] Weinberg, S., 1972, *Gravitation and Cosmology*, (New York: Wiley).

[203] Weinberg, D.H., Ostriker, J.P., and Dekel, A., 1989, *Ap. J.* **336**, 9.

[204] Yang, J., Turner, M.S., Steigman, G., Schramm, D.N., and Olive, K.A., 1984, *Ap. J.*, **281**, 493.

[205] Yoshioka, S., and Ikeuchi, S., 1989, *Ap. J.* **341**, 16.

[206] Zaidi, M.H., 1983, *Fortschr. Phys.*, **7**, 403.

[207] Zel'dovich, Y.B., 1972, *M.N.R.A.S.* **160**, 1.

[208] Zwicky, F., Herzog, E., Karpowicz, M., and Koval, C.T., 1961–1968, *Catalogue of Galaxies and Clusters of Galaxies* (Pasadena, Calif.: California Institute of Technology).